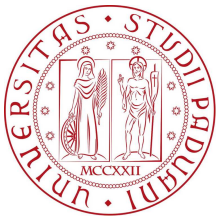

UNIVERSITÀ DEGLI STUDI DI PADOVA

Dipartimento di Fisica e Astronomia "Galileo Galilei"

Master Degree in Astrophysics and Cosmology

Final Dissertation

Accretion and ejection at work in the Narrow-Line Seyfert 1 Galaxy 1H 0323+342

Thesis supervisor:
Prof. Stefano Ciroi

Candidate:
Valentina Rosa

Thesis co-supervisor:
Dr. Luigi Foschini

Academic Year 2022/23

«Curious heart, wants to observe
something it cannot see»

1. List of Abbreviations

AD: Accretion Disk
AGN: Active Galactic Nucleus/Nuclei
BH: Black Hole
BL Lac: BL Lacertae
BLR: Broad Line Region
EC: External Compton
Fermi LAT: Fermi Gamma-ray Large Area Telescope
FOV: Field of View
FSRQ: Flat Spectrum Radio Quasars
FWHM: Full Width Half Maximum
IC: Inverse Compton
IR: Infrared
ISCO: Innermost Stable Circular Orbit
JD: Julian Date
MJD: Modified Julian Date
MCMC: Monte Carlo Markov Chain
NLR: Narrow Line Region
NLS1: Narrow Line Seyfert 1 Galaxy
pc: Parsec
RL: Radio Loud
RM: Reverberation Mapping
RQ: Radio Quiet
SED: Spectral Energy Distribution
SMBH: Super Massive Black Hole
SSC: Synchrotron Self Compton
Swift: Neil Gehrels Swift Observatory
XRB: X-Ray Binaries **XRT**: X-Ray Telescope
UVOT: Ultra-Violet Optical Telescope

1.1 List of Symbols

c: Speed of light in a vacuum

G: Gravitational constant

h: Planck constant

k: Boltzmann constant

M_{BH}= Black Hole Mass

$M_{\odot}$: Solar mass

σ_T= Thompson Cross Section

r= radius, distance from central source

v= velocity of gas

R_g: Gravitational radius

Abstract

Context: The Jetted Narrow Line Seyfert 1 galaxy, 1H 0323+342, is an interesting source within the domain of Active Galactic Nuclei (AGN), thanks to its low redshift, z=0.063. This thesis embarks on an extensive exploration of the properties of 1H 0323+342 through the analysis of a dataset spanning from 2006 to 2023, comprehensive of 170 Swift observations in the optical, ultraviolet and x-ray bands, combined with 78 Fermi LAT observations.

Purpose: The primary aim of this research is to understand the interplay between the relativistic jet, the hot corona and the accretion disk around a supermassive black hole, by interpreting x-ray spectral parameters such as the variation of flux and photon index. By searching for correlations with observed features in optical, ultraviolet and gamma-ray bands, I aspire to understand the interacting regions that dominate in the innermost regions of this AGN.

Methods: I performed a spectral analysis of 170 Swift X-Ray Telescope (XRT) observations. Spectral fitting provided the main parameters such as the Photon Index, Γ, and the flux values in the 0.3-10.0 keV energy range. For each XRT observation I collected the optical and ultraviolet counterparts and from the magnitudes I obtained fluxes values and then the spectral indices. Additionally, my research extends to the Fermi Large Area Telescope (LAT) lightcurves, affording a supportive assessment of multi-wavelength variability in 1H 0323+342.

Results: On the photon index-flux graph I identified three *zones* which represent three different stages of the jet-corona-disk interaction. I emphasize that the third *zone*, having lower flux and a steeper profile, is dominated by recent data, suggesting that jet emission has decreased during the latest observations. The hypothesis is supported from the available Fermi LAT data, while the parameters obtained from UVOT observations make us reject the scenario of a decrease in the accretion rate.

Conclusion: The thesis suggests two hypothetical explanations to explain the observations: the Blandford-Znajek theory revisited, and a disk instability scenario. The research provides valuable insights into the intricate mechanisms of disk-corona-jet interactions in AGN, particularly jetted Narrow Line Seyfert 1 galaxies. The study emphasizes the need for multiwavelength techniques and approaches in understanding the "short"-scale variations and their origins, providing a foundation for future investigations in the field of AGN research.

Contents

List of Figures

List of Tables

Introduction

The name "black holes" defines non-luminous objects. However, their looming shadow permeates a gigantic portion of our Universe: their enormous gravity keeps stars with their planets trapped in orbit, and then, eventually consumes them.

The extremely massive black holes are believed to disrupt the environment of galactic central regions with such violent interactions that are hard to imagine. Sometimes their behaviour is even dominating the energy emission of an entire galaxy. It is the case of Active Galactic Nuclei.

All the information provided below is obtained from summarizing and revising relevant books and articles such as: Peterson (1997), Rybicki and Lightman (1979), Foschini et al. (2019), Antonucci (1993).

Active Galactic Nuclei (AGN) stand as some of the most enigmatic and dynamic objects in the universe. These cosmic powerhouses, residing at the centers of galaxies, exhibit a diverse assembling of behaviors and emissions that challenge our understanding of astrophysical processes.

At their heart lies a supermassive black hole (SMBH) surrounded by a complex structure encompassing an accretion disk, a hot electron corona, a broad-line region (BLR), a dusty torus, and more externally a narrow-line region (NLR). Some AGN were also found to eject collimated plasma at relativistic speeds.

The intense radiation emitted by AGN spans the entire electromagnetic spectrum, from radio waves to gamma-rays, making them a subject of profound

interest and extensive study.

Initially, their distinctiveness was marked by extremely broad emission lines, indicative of a high-speed rotating gas, then found to be related to accretion onto these massive black holes. These anomalous characteristics were useful to provide a first distinction among these sources:

- **Type 1 AGN**: Exhibiting both broad and narrow emission lines, as a proxy of a direct view of the inner regions.
- **Type 2 AGN**: Exhibiting only narrow emission lines as a consequence of the supposed obscuration of the inner regions.

After improvements in radio observations, an AGN classification based on their emission in the radio band could be provided:

- **Radio-Quiet AGN**: Exhibiting no significant radio emission compared to the B band. Seyfert galaxies traditionally belong to this cathegory.
- **Radio-Loud AGN**: Exhibiting high radio emission compared to the B band. Quasars and BL Lac objects belong to this cathegory.

However, during the latest decades, the improvement of instruments sensitivities and surveys made it possible to detect radio and high-energy gamma-ray emission also from Seyfert galaxies, with particular reference to Narrow-Line Seyfert 1 galaxies.

It represented an exceptionally meaningful discovery as NLS1 galaxies traditionally belonged to the radio-quiet category, even though they still exhibited unique characteristics.

Since the detection of powerful relativistic jets similar to those found in blazars, we can say that these jetted NLS1 show a dual nature combining the features of Seyfert galaxies and radio-loud AGN and this makes them an interesting and

fascinating target to study.

The source I present, 1H 0323+342, is the closest γ-Narrow Line Seyfert 1 Galaxy at a redshift of z=0.063. The aim of the present work is to obtain deeper insights about its central engine, its surroundings and especially its jet emission mechanism and how it is related to the other internal components.

This thesis focuses on X-ray spectral data obtained from Neil Gehrels Swift Observatory, taken by X-ray Telescope XRT, including 170 observations spanning from 2006 to 2023.

In a Seyfert galaxy, the X-ray emission is thought to be the result of the Compton upscattering of the UV photons of the accretion disk from the hot electrons of the surrounding corona. However, after the detection of strong radio and gamma-ray emission, the existence of a powerful relativistic jet was evident. Therefore, I would like to investigate the interplay between the accretion disk and the jet by analysing optical-to-gamma ray data from Swift and Fermi surveys.

The study reveals a classification of observations into three *zones* that show different fluxes and photon index values from one another. We do not find significant correlations between decreased X-ray and UV flux values, as UVOT fluxes tend to remain constant overtime. We only observe a spectral softening in all bands over the last observations.

70 additional Light Curves collected from Fermi LAT from 2008 to 2023 were ultimately analysed, obtaining photon index and flux data. Results show correspondence between high flux values in both X-ray and gamma-ray bands during specific time intervals. However the latest data were not sufficient to compare them precisely with the X-ray observations that showed a decreasing flux.

This dissertation is structured mainly in five chapters: the first two will provide an overview of Active Galactic Nuclei and our current understanding on their structure, their spectral classification, and AGN subclasses. I will focus on the case of 1H 0323+342, summarizing the acquired knowledge from previous literature. The third chapter will be dedicated to the instruments used, such as the Swift Satellite and Fermi Satellite, and I will provide insights into the X-ray telescope XRT and Optical/Ultraviolet telescope UVOT. From chapter four all the data analysis is explained: I will describe in detail the data processing and analysis methods applied to 1H 0323+342 observations. Results are presented in the last chapters, discussing the jet emission mechanism through correlations across different observation bands and investigating the apparently ceased jet emission in the last years. The conclusion summarizes the key findings of the study, while in the bibliography I list all the relevant articles that contributed to this research.

2. Active Galactic Nuclei

2.1 AGN: from observations to models

The universe is filled with immensely energetic entities and occurrences, among which Active Galactic Nuclei (AGN) stand out as some of the brightest and most powerful persistent sources of electromagnetic radiation. These remarkable phenomena are located at the cores of what are known as active galaxies, deriving their energy from large-scale accretion of matter onto supermassive black holes (SMBH).

One of the fascinating features characterizing these objects is their emission, spanning the entire electromagnetic spectrum. But how can we distinguish properly these powerful sources from regular galaxies or distant stars?

Some of the characteristics, that may also not necessarily be all present, sufficient for defining a galaxy as an AGN from an optical perspective are the following:

- A compact nuclear region, brighter than the corresponding region in galaxies of the same Hubble type.
- Nuclear emission in the continuum, which can be either thermal or non-thermal, across the electromagnetic spectrum or a portion of it.
- High-excitation, broad (FWHM>1000 km/s) emission lines, generated by a central thermal ionizing source.
- Correlated variability of emission lines and continuum.

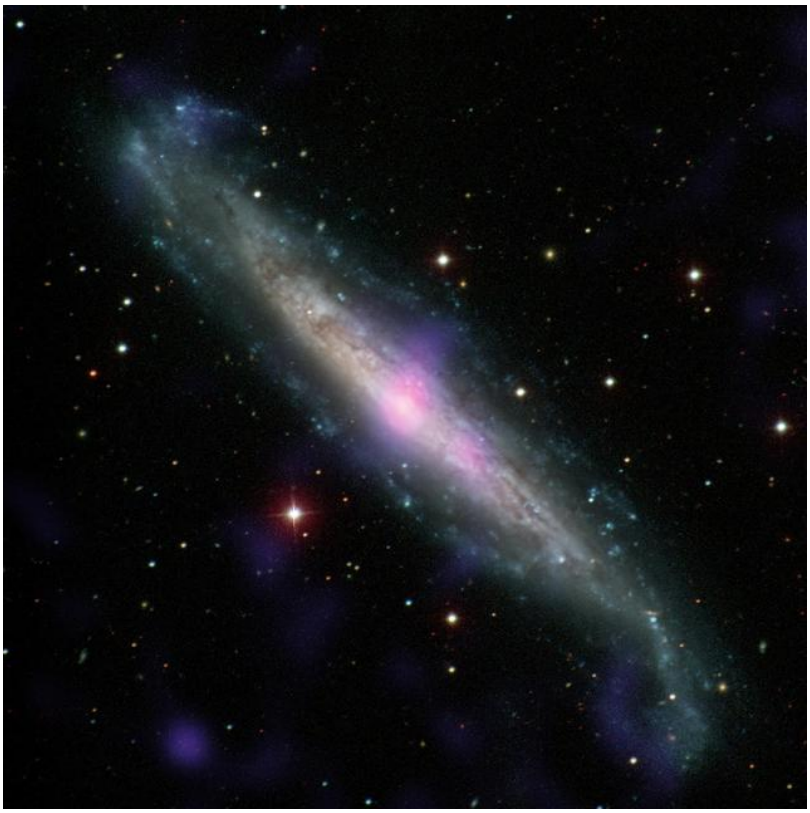

Figure 1: Galaxy NGC 1448 with Active Galactic Nucleus
Credits: Carnegie-Irvine Galaxy Survey/NASA/JPL-Caltech

The journey towards the comprehension of AGN started with the early observations of emission lines within galactic nuclei, pioneered by Carl Seyfert in the 1940s (Seyfert, 1943). He observed high-excitation nuclear emission lines superimposed on a normal star-like spectrum in six galaxies. Some of these galaxies displayed broad emission lines, while others only had narrow ones. At the time, it was unclear what caused this large broadening in emission lines, and some suggested it could have been due to a large number of stars.

In the early 1950s, the discovery of a large amount of radio sources carved the way for renewed focus on AGN. These sources showed in the radio band one or two lobes that could reach a size even bigger than the host galaxy. These lobes were subsequently considered linked to jets: specifically, they were found to generate from the jet interaction with the interstellar medium.

The origin of these jet emissions is still uncertain nowadays. However, they seem to originate from synchrotron radiation of relativistic electrons spiralizing around the magnetic field lines.

The journey towards the carachterization of AGN continues with relevant advancement in the following decades. Around the 1960s we note the identification of quasi-stellar radio sources, or quasars, by astronomers such as Schmidt (1963), Sandage (1969).

Further investigation led to a tremendously important revelation: as the concentration of emission within the central 100 parsecs of these galaxies would require a mass of several million solar masses, there had to be a supermassive object residing in the center of these galaxies, specifically a Super Massive Black Hole.

The fundamental energy source driving AGN was understood to be accretion onto a sorrounding gas disk and the presence of broad emission lines with velocities exceeding 1000 km/s was supposed to be due to the fast rotation of the gas around the supermassive central object.

Atoms emitting radiation have a distribution of velocities, therefore each photon emitted will be red or blue-shifted by the Doppler effect depending on the velocity of the atom relative to the observer. Hot regions are linked to wide velocity distributions and broad lines that are observed in the optical bands.

AGN also exhibited narrow, non-variable forbidden and permitted emission lines which were relative to galactic nebulae located at larger radii from the central engine.

Another typical feature among AGN was the distinctive blue continuum spectrum, differing from typical galaxies. This "big blue bump" in their spectra

represented an additional hint at the presence of an emitting Accretion Disk.

Additionally infrared emission was detected, and it could be explained with the presence of a thermal secondary emission generated from dust located at a distance within a few parsecs from the central BH. Dust particles are heated from AGN nuclear radiation and re-emit in the infrared band.

Thanks to multi-wavelength studies, a broad diversity in the types of AGN was identified.

A first classification system based on broad and narrow emission line characteristics in AGN optical spectra was introduced in 1978 (Khachikian and Weedman, 1974,Osterbrock, 1978).

In this classification system we observe:

- **Type 1 AGN**: Exhibiting both broad and narrow emission lines in their optical spectra.
- **Type 2 AGN**: Exhibiting only narrow emission lines.

A question was raised of whether the diversity of AGN classes could be attributed to an observational viewing angle effect.

A major observational breakthrough came with spectropolarimetric measurements made of the Seyfert galaxy NGC 1068 (Antonucci and Miller, 1985), which revealed a Type 1 optical spectrum in polarized light, despite the AGN being classified as a prototypical Type 2 AGN. Such an observation was interpreted in terms of a BLR and a central continuum source that was obscured from the observer by a dusty torus surrounding the SMBH outside the BLR. The BLR emission was reflected and scattered into the observer's line of sight by material located in the inner areas of the torus, thereby polarizing the photons.

The basic unified model accounts for the narrow emission lines observed in

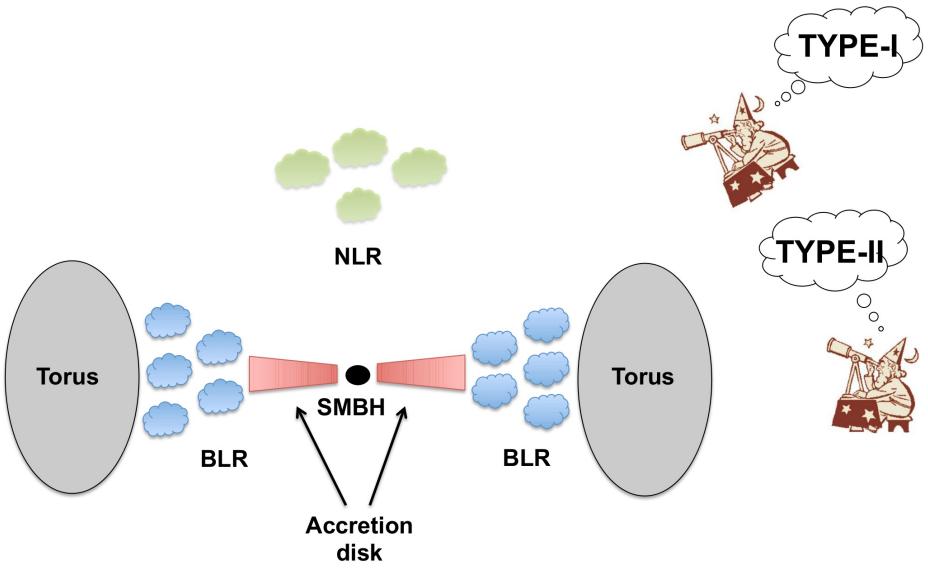

Figure 2: Type 1 and 2 AGN as viewed from different angles
Credits: ESA

both Type 1 and 2 AGN and the absence of broad emission lines in the optical spectra of Type 2 AGN since the BLR is obscured by the torus in Type 2 AGN which are typically viewed at edge-on inclinations. In Type 1 AGN, the torus is viewed at face-on angles with a direct, unobscured view of the BLR.

X-ray observations of AGN were also been applied to address issues of fundamental black hole physics. The shapes of line profiles have been compared to models which in principle allow one to infer the BH intrinsic angular momentum or spin, an important parameter related to the accretion rate (Brenneman and Reynolds, 2009).

The basic idea is that the asymmetry of a line profile, usually the Fe Kα one at 6.4 keV, produced in the inner AGN accretion disk, depends in a predictable manner on the shape of the gravitational potential, which in turn depends on the black hole spin.

Other questions were addressed, since the intense emission in the X-ray band could not be justified only by the presence of an Accretion Disk. Accretion

Disks usually do not exceed a temperature of $10^5 - 10^6$ K, therefore another additional hot component is needed in order to generate X-ray photons. The observed spectrum is characteristic of an inverse compton scattering radiation, where soft photons are up scattered from hot electrons.

Combining the results of several years of multiwavelength studies, the formalism for the basic unified model of AGN was proposed (Antonucci, 1993).

According to this model, the differences between observational classes of AGN are attributed to an orientation effect where the SMBH and torus are viewed at different angles along the observer's line of sight. Within this classical unified model, there are several key components of an AGN, described as follows:

- Super Massive Black Hole (SMBH)
- Accretion Disk (AD)
- Hot Corona
- Broad Line Region (BLR)
- Dusty Torus
- Narrow Line Region (NLR)

Some classes of AGN also exhibited presence of jet emission, detected by radio and gamma observations.

2.1.1 Structure of AGNs

2.1.1.1 SMBH

Located at the centre of the AGN there is a Super Massive Black Hole, whose mass ranges from 10^6 to 10^{10} $M_\odot$, actively accreting matter from gas and plasma surrounding it, thanks to its gravitational field.

SMBH are characterized mainly by their spin and especially their mass, M_{BH} which characterize their gravitational radius R_g, corresponding to the black hole event horizon. It ranges in size from 10^{-7} pc for a 10^6 $M_\odot$ black hole, to 10^{-3} pc for a 10^{10} $M_\odot$ black hole. If the black hole is rotating, as it is usually found from observations, it is defined as:

$$R_g = \frac{GM_{BH}}{c^2} \tag{2.1}$$

This radius is useful to define distances especially in the central regions of AGN.

2.1.1.2 Accretion disk

Accretion Disks are structures formed from material rotating in the vicinity of a compact object. In the case we treat here we will refer only to SMBH.

The material getting closer to the SMBH is forced to spin in the object's plane of rotation. Matter loses angular momentum as it spirals inwards and is accreted onto the SMBH, resulting in gravitational energy being converted to thermal blackbody radiation. It is primarily observed in the optical or UV spectrum with temperatures ranging between 10^4 and 10^5 K.

According to the most common model it is generally treated as a geometrically thin, optically thick structure (Shakura and Sunyaev, 1973).

The energy release in thin accretion disks is determined by the loss of gravitational energy of the inward going material and the work done by the torque that results in outward loss of angular momentum. In terms of the luminosity L, if we combine the two contributions and differentiate with respect to r, the distance from the central source, we obtain an expression for the energy release

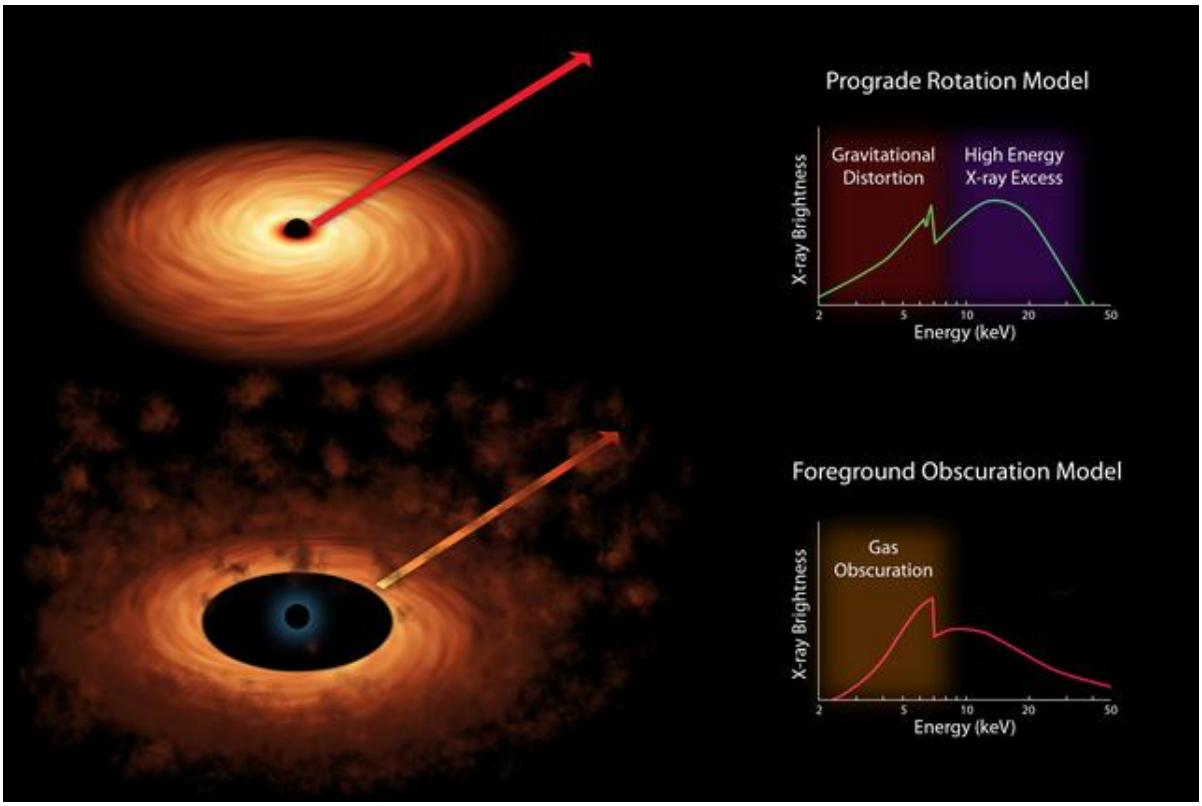

Figure 3: Two Models of Black Hole Spin Artist Concept
Credits: NASA/JPL-Caltech

at various radii:

$$\frac{dL}{dr} = \frac{3G\dot{M}M}{2\,r^2}\left(1 - \frac{r_{in}}{r}\right) \tag{2.2}$$

where the second term on the right takes into account the innermost radius of the disk, r_{in} and $\dot{M}$ indicates the mass accretion rate.

Simple integration over parts of the disk far from its center shows that the luminosity as a function of distance, L_r, grows as the accretion rate grows: $L_r \propto \frac{G\dot{M}M}{r}$.

The total radiated power, obtained by integrating over the entire disk, in the

non-relativistic limit, is

$$L = \frac{1}{2}\frac{G\dot{M}M}{r_{in}} \tag{2.3}$$

This is half the total available power meaning that, neglecting relativistic corrections, the matter at r_{in} still retains a kinetic energy which is half the potential energy it has lost.

The accretion disk thermal radiation can be observed across a broad range of wavelengths with the peak depending on the mass of the black hole and the accretion rate.

The accretion rate of the central engine is usually measured in comparison to its limit value, called Eddington Limit: the maximum luminosity value coming from accretion of matter onto a spherical body in hydrostatic equilibrium. This value is reached when the radiation pressure generated from the dynamics in the inner accretion disk equals the gravitational attraction exerted by the central engine. Beyond this luminosity, radiation pressure will overcome gravity, and material outside the object will be forced away from it rather than falling inwards.

If we express the luminosity in terms of the accretion rate $\dot{M}$ and we call ϵ the fraction of Gravitational Potential Energy that is radiated away:

$$L = \epsilon \dot{M} c^2 \tag{2.4}$$

The radiation pressure P_{rad} generated from accretion mechanisms is given from

the formula:

$$\mathrm{P_{rad}} = \frac{\mathrm{L}}{\mathrm{c}4\pi\mathrm{r}^2} \tag{2.5}$$

And since a pressure is a force per unit surface, we can express the force generated from radiation pressure $\mathrm{F_R}$ as:

$$\mathrm{F_R} = \mathrm{P_{rad}} \frac{\sigma_\mathrm{T}}{\mathrm{m_p}} \dot{\mathrm{M}} \tag{2.6}$$

Here the fraction $\frac{\sigma_\mathrm{T}}{m_p}$ is the cross-sectional area per unit mass for radiation scattering, where specifically σ_T is the Thomson cross-section and $\mathrm{m_p}$ is the proton mass.

The expression for the Eddington Accretion Rate comes out from equating the radiation pressure force with the gravitational force, namely, the condition defining the Eddington limit. After some substitutions we obtain:

$$\frac{\epsilon \mathrm{c} \sigma_\mathrm{T} \dot{\mathrm{M}}_\mathrm{Edd}^2}{4\pi \mathrm{r}^2 \mathrm{m_p}} = \frac{\mathrm{G} \dot{\mathrm{M}}_\mathrm{Edd} \mathrm{M}}{\mathrm{r}^2} \tag{2.7}$$

$$\dot{\mathrm{M}}_\mathrm{Edd} = \frac{4\pi \mathrm{M} \mathrm{m_p}}{\epsilon \mathrm{c} \sigma_\mathrm{T}} \tag{2.8}$$

with M mass of the central Black Hole and $\dot{\mathrm{M}}$ the mass accretion rate.

Different types of AGN have shown to accrete at different rates compared to the

Eddington Limit and this feature was linked to differences in the sorrounding environment and evolutions in the disk structure.

As the orbiting material approaches the inner regions, however, other mechanisms will be taken into account: electron scattering and comptonization.

The spectral emission from the inner regions will therefore have three source models that contribute to the total energy, arising from the occurring processes: a modified blackbody (electron scattering) and a powerlaw model (comptonization) in addition to the thermal blackbody, with the powerlaw dominating at high temperatures (Wandel and Petrosian, 1988).

Powerlaw emission follows the distribution:

$$\mathrm{F}_\nu \propto \nu^{-\alpha} \tag{2.9}$$

with F being the flux value, ν the frequency at which we observe the emission and α the so-called spectral index. It can be evaluated as follows:

$$\alpha_{12} = \frac{-\log \frac{S_1}{S_2}}{\log \frac{\nu_1}{\nu_2}} \tag{2.10}$$

In this formula, S stands for flux density and ν_i are the frequencies in band 1 and 2. 1 and 2 are general indices that indicate the frequency interval within which we calculate the slope.

It is relevant to note that the thin disk model does not explain properly every feature that was observed within AGN accretion disks. Other models were then proposed, for example Advection Dominated Accretion Flows (ADAF) disks,

where a large fraction of the released energy is stored in the gas and advected into the black hole instead of being radiated away. Advective disks are therefore geometrically thick.

An additional model was introduced to explain the X-ray emission observed from AGN accretion flows: the corona-disk model which fulfills the required presence of emitters other than the accretion disc described previously.

It adds a X-ray radiating structure positioned above the black hole, called corona. The name is given in analogy to solar and stellar coronae: optically thin hot structures, hotter than the underlying photosphere.

2.1.1.3 Corona

The hypothesis suggesting the presence of a hot corona responsible of the X-ray emission linked to a relatively cold accretion disk was presented a long time ago (Bisnovatyi-Kogan and Blinnikov, 1977).

The corona is supposed to generate and power the luminous X-ray continuum emission that we observe. The most common models describe it as a hot cloud of plasma located close to the inner part of the accretion disk. Within the corona, electrons Compton-upscatter optical and UV photons from the accretion disk to X-ray energies (Rybicki and Lightman, 1979).

The resulting emission from the corona is therefore well described by the distribution of the electrons in the plasma. A power law model with $\mathrm{N(E)} \propto \mathrm{E}^{-\Gamma}$ is thus appropriate. Here N stands for the electrons number density and E is their energy.

The X-ray photon index Γ, in the energy band 0.2-10 keV, is usually in the range $1.5 - 2.5$ (Nandra and Pounds, 1994, Reeves and Turner, 2000, Piconcelli et al., 2005) and the Γ value for unsaturated Comptonization is 1.9. Some sources will

show lower or higher Γs, which are believed to depend on the coronal electron temperature kT_e and the optical depth τ .

While many of the properties of the corona remain a mystery, it has been established to be a compact structure. The observed rapid variability of the 2–10 keV X-ray emission seen in many AGN, combined with X-ray spectral timing strongly indicate that the corona is physically compact, of the order 3–10 R_g in radius and height above the SMBH (De Marco et al., 2011, Kara et al., 2013, Fabian et al., 2015).

In addition to being physically small, the corona can also be radiatively compact, meaning that interactions involving significant energy exchange between particles and photons are occurring within the source, leading to a large ratio of coronal luminosity to radius (Fabian et al., 2015).

We underline another interesting feature of the coronal emission processes: as the density of high-energy photons is increased, photon-photon collisions can lead to electron-positron pair production. Increasing energy supplied to the corona thus has the effect of producing more particle pairs to share the available energy. In this way, pair production can become a runaway process that exceeds particle annihilation, thereby limiting any further rise in the temperature of the corona.

According to the current most popular theory (Haardt and Maraschi, 1993), the X-rays are produced via Inverse Compton (IC) emission in a hot corona embedding a colder accretion disk. Soft thermal photons emitted by the cold layer provide the main source of cooling for the hot electrons in the corona. At the same time, about half of the high-energy photons produced in the corona are able to heat the underlying dense layers. The energy coupling between the disk and the corona forces the electron temperature to adjust to maintain com-

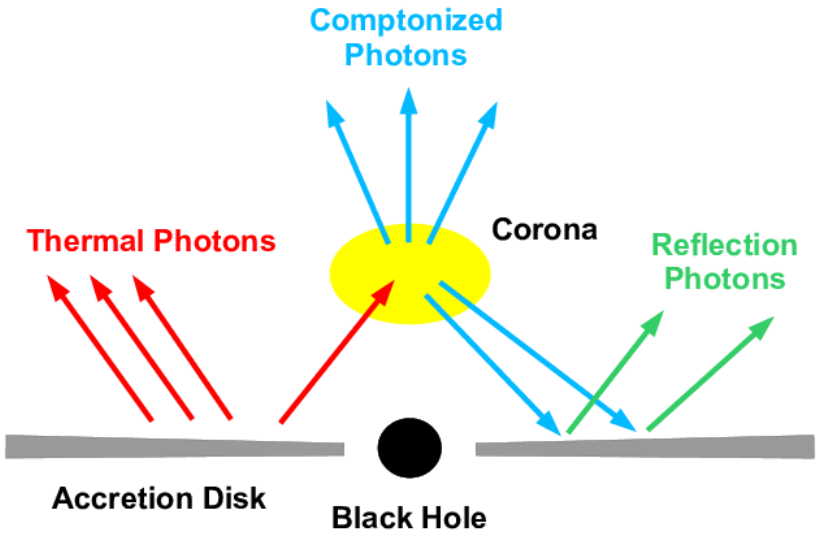

Figure 4: Cartoon of Disk Corona Model
Bambi, 2023

parable luminosities in the soft and hard components of the emitted radiation, independently of the optical depth of the scattering medium. The total emitted spectra consist of the intrinsic IC emission from the hot layer, plus the thermal flux and a reflected component from the cold disk.

However, there is a longstanding problem of how energy is supplied to heat the corona, since sources generally have a cooling timescale that is shorter than the light crossing timescale.

A possible explanation could be that the corona is powered by reconnecting magnetic field loops originating from the strong differential rotation of the accretion disk (Galeev et al., 1979). This implies that the corona is coupled to the disk by the magnetic field and the two are in persistent interaction.

2.1.1.4 Broad Line Region

Moving further from the compact object, a region of high velocity and high temperature gas clouds is located surrounding the innermost regions of the

AGN.

These gas clouds intercept a small percentage of the ionizing radiation, about 10%, and emit it again in the form of lines. Doppler shifts broaden the observed lines and this is why this region is called Broad Line Region.

The widths of the lines are used to infer the velocity of the rotating gas and therefore also the mass of the SMBH, through reverberation mapping. This method assumes that the dynamics of the gas in the BLR is dominated by gravitational forces and therefore enables to evaluate the black hole mass. It is indeed a function of the radial distance of the BLR gas from the continuum emitting source in the center, the velocity dispersion of the gas v, and a scaling factor f that depends on the still mostly unknown dynamics and geometry of the BLR.

The BLR radius that is used to infer the mass value can be directly measured through this reverberation mapping technique that determines the light-travel time-delayed lag t_{LAG} that the flux of the BLR takes to responds to variations in the ionizing continuum flux.

Applying virial theorem, the SMBH mass can be inferred:

$$\frac{\mathrm{GM_{BH}}}{f\, r_{\mathrm{BLR}}} = v^2 \tag{2.11}$$

$$\mathrm{M_{BH}} = \frac{v^2 f r_{\mathrm{BLR}}}{\mathrm{G}} \tag{2.12}$$

Reverberation mapping is an extremely useful technique to measure the black hole mass as it does not require spatial resolution.

2.1.1.5 Dusty Torus

At a distance enclosed within 10^5 R_g, a geometrically and optically thick dust emitting region, called dusty torus, is located around the central engine.
The inner radius of this dust region corresponds to the dust sublimation radius, while the outer radius is bound by the gravitational sphere of influence from the SMBH. It is mostly believed that this dusty region can obscure some direct observations of the optical and UV emissions depending on orientation of the AGN with respect to the observer.

There is a contemporary debate whether the torus can be properly described by smooth and homogeneous distribution models or if it is distributed in clumps. In order to estimate the dust distribution within the AGN, IR and near-IR interferometry are essential tools.

2.1.1.6 Narrow Line Region

After about 10^6 R_g we can find another region with less dense clouds moving less rapidly with respect to the Broad Line Region. This area is called Narrow Line Region (NLR). It has a biconical structure extending beyond the torus. As this gas is still ionized from the radiation coming from the center, emission lines in the optical spectra are detected. These lines are narrower than the ones produced in the BLR, due to slower velocities of the gas that forms this region.

Another important feature is the presence of forbidden narrow emission lines: since the gas there is less dense, the collisional timescales can be longer than forbidden decay timescales, allowing forbidden lines to appear.

Narrow emission lines are observed in both Type 1 and 2 AGN while the broad emission lines are observed exclusively in Type 1 AGN; we therefore assume, according to the basic unified model, that the BLR is obscured by the torus in

Type 2 AGN and only the NLR is observed in these cases.

2.1.1.7 Jets

About 14% of Active Galactic Nuclei exhibit extreme features of plasma expulsion in the form of collimated jets, typically following the direction of the rotational axis of a spinning black hole. These jets, consisting of material moving at relativistic speeds, can extend over vast distances, ranging from kiloparsecs to megaparsecs from the central engine. Radio telescopes have been crucial instruments in detecting the resulting morphological features, such as extended lobes and hotspots, that arise from the interaction between these jets and their surrounding medium (Padovani, 1997).

Understanding the origin of these relativistic jets remains an ongoing challenge in astrophysics. Today, the prevailing theory for jet formation regards the Blandford-Znajek mechanism, which requires a spinning black hole to extract energy from it. This process relies on the dragging of magnetic fields by the black hole spin and the subsequent launch of relativistic material through magnetic field line reconfiguration (Blandford and Znajek, 1977).

The emission produced in the jets is believed to derive from synchrotron radiation spanning the frequency ranges from radio to X-rays. This emission arises when the charged relativistic particles are accelerated: spiralizing around the magnetic field they are subject to an acceleration perpendicular to their velocity and photon emission occurs (Falle, 1986).

With advancements in radio telescope angular resolution, researchers have been able to investigate the shape of jets in active galactic nuclei in great detail, from large scales down to regions near the central black hole. These studies have consistently confirmed the self-similarity of jet shapes, with the innermost

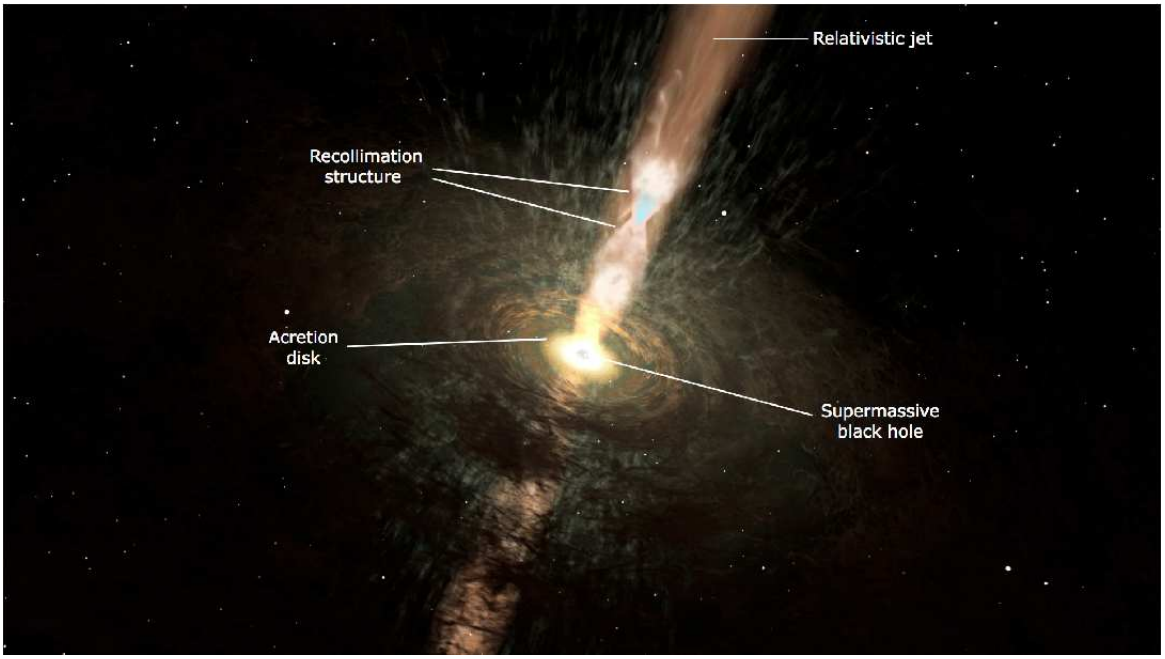

Figure 5: Relativistic Jet from a Black Hole
Credits: W. Steven, UNAM, Cosmovision.

part exhibiting a parabolic shape and a transition to a conical shape after a collimation break (Hada, 2019). This concept of self-similarity is crucial for applying the scaling laws (Heinz and Sunyaev, 2003) according to which the jet power depends on the mass of the central black hole and the nature of the accretion disk, whether it is dominated by advection, gas pressure, or radiation pressure.

These relationships are nonlinear: for instance, in the case of a radiation-pressure dominated disk, the jet power P_J increases as the mass of the central compact object increases, specifically $P_J \propto M_{BH}{}^{\frac{17}{12}}$, while in other cases additional components related to the accretion rate are involved.

The confirmation of relativistic jet emissions from AGNs through gamma ray detections, especially by the the Energetic Gamma-Ray Experiment Telescope (EGRET) and later on by its successor, the Fermi Large Area Telescope (LAT), has shed light on the dominant processes occurring in the gamma band. These

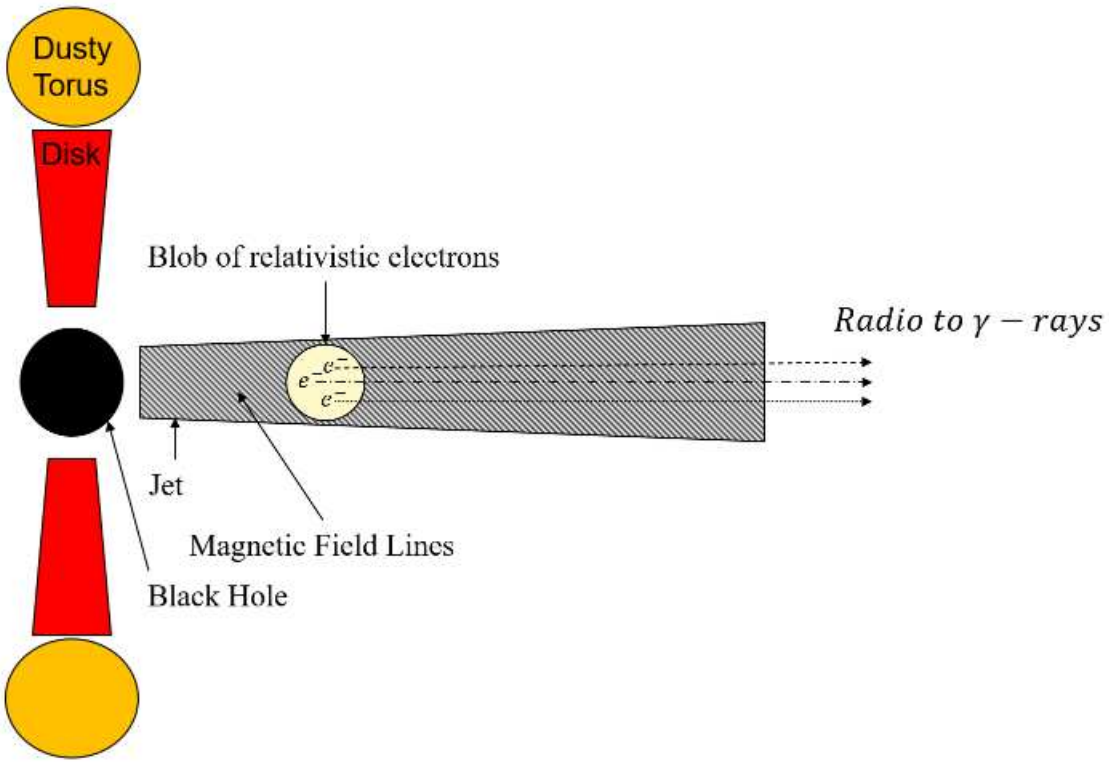

Figure 6: Scheme of jet emission mechanism with prevailing SSC processes.

emissions are primarily driven by synchrotron self-comptonization (SSC) and external comptonization (EC). SSC arises from synchrotron-generated photons being scattered by relativistic electrons in the jet, while EC involves the scattering of external photons from the accretion disk or the Broad Line Region (BLR) by the jet electrons.

The type of synchrotron comptonization that prevails depends on the immediate environment. If a strong emitting disk is present, external comptonization becomes dominant. Therefore in these sources, the origin of jets is closely tied to our understanding of the accretion process that powers AGN, with magnetic fields playing a crucial role.

Yet, fundamental questions remain, such as the reasons behind the presence or absence of jets in different AGNs and the correlation between luminosity, mass, and jet power.

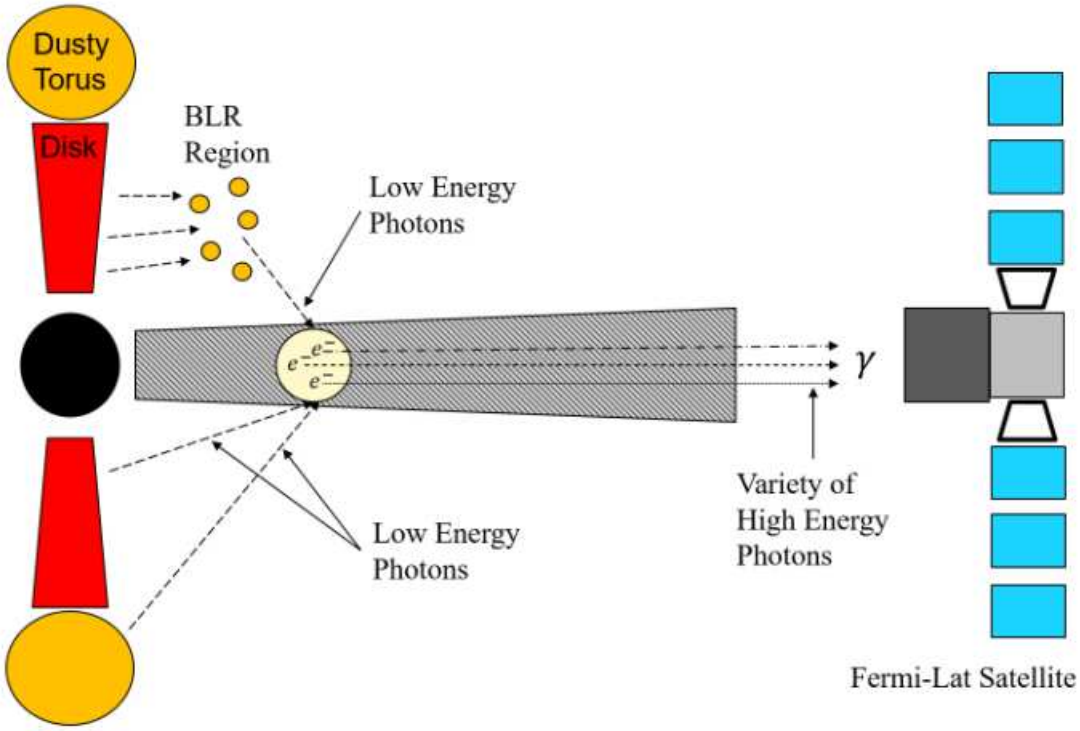

Figure 7: Scheme of jet emission mechanism with prevailing EC processes.

An ongoing issue is to address whether jet acceleration occurs in the immediate vicinity of the central black hole or gradually over larger distances. This is complicated by the potential for a "Compton drag" effect due to inverse Compton scattering with the radiation field in the inner region.

This complex subject necessitates further research to construct a Unified Model that encompasses these intricate features, shedding light on the enigmatic phenomenon of AGN jet formation and evolution.

2.2 Standard Model of AGN

By evaluating the primary emission band and analysing their spectral characteristics, various subclasses can be distinguished within the realm of AGNs. As we anticipated above, a first classification of AGN was based on the shape of the detected emission lines.

- **Type 1**: show very broad optical/UV permitted emission lines, with FWHM $>$ 1000 km/s. Narrow (forbidden) lines typically have FWHMs of order of 500-1000 km/s.
- **Type 2**: show lines with FWHM ranging usually from 500 to 1000 km/s.

In type 1 AGN we are seeing both the Broad and Narrow Line regions features, therefore we expect them to be placed closely face-on with respect to our line of sight. Spectral features of type 2 AGN, on the other hand, are suggesting that in this case we only see rotating gas on the outer regions of the AGN, the Narrow Line Region. Since the BLR is supposed to be covered by the dusty torus, we expect that these AGN are placed almost edge on with respect of our line of sight allowing us to see only the NLR.

In this context of Unified Models, the same processes are at work in all AGN and the main differences in their observed properties are rather ascribed to orientation effects.

However, several other different observed features were found. Their discovery indicated the need of other parameters to differentiate types of AGN. For example: with the introduction of powerful radio telescopes in the 1960s, scientists uncovered strong radio sources that often exhibited a point-like appearance in their optical counterparts.

The simple unification scheme which only considered absorption and beaming was therefore not sufficient to answer the question of why some sources were strong radio emitters, and some were not. In other words, what makes the central engine produce a jet.

Indeed, another fundamental division in the classification scheme needed to be taken into account, regarding the AGN radio emission. Early studies suggested

that the differences in radio properties could have been related to fundamental physical differences unlike the previously cited optical features.

Another classification was introduced, and it was based on the emission intensity in the radio band. This feature is well described by the radio loudness parameter R, defined as the ratio of the 5 GHz flux density to the optical flux density in the B band (Kellermann et al., 1989):

$$R = \frac{F_{5GHz}}{F_B}. \tag{2.13}$$

This classification divided AGN into:

- **Radio-Quiet AGN**: R«10, showing weak or negligible radio emission compared to other bands.
- **Radio-Loud AGN**: R>10, suggesting strong radio emission associated with highly energetic and collimated jets of charged particles.

After astronomers had learned how to measure the mass of SMBH (Peterson and Wandel, 1999), it became possible to study also the dependence of the radio loudness parameter R on the Black Hole mass and the Eddington ratio, which is defined as:

$$\lambda_{Edd} = \frac{L_{bol}}{L_{Edd}} \tag{2.14}$$

where L_{bol} stands for bolometric luminosity.

It was noticed that the radio loudness appeared to increase with decreasing Eddington ratio, more quickly at higher accretion rates, and more slowly at lower accretion rates.

Another possible trend which had been found was the correlation of the mass of the central black hole and the radio-loudness of the AGN. High radio-loudness usually required high masses.

All these studies then led to the assumption that the various types of AGN could be approximately described by three basic parameters:

1. Black Hole Mass, M_{BH};
2. Accretion Rate, $\frac{L_{bol}}{L_{Edd}}$;
3. Inclination Angle, i.

However, in a study including the recently discovered jetted NLS1 galaxies, it was shown that these sources were characterized from high radio-loudness and low masses. Therefore, no straightforward relationship has been found between radio loudness and M_{BH} and the concept of radio loudness does not provide any deep insight on the characterization of jet power. It is worth noting, indeed, that that low-power jet sources can have either high or low radio-loudness parameters.

Also the Radio Loudness failed in the attempt of classifying AGN based on their physical properties as it is still an artificial parameter with an abitrary threshold. Its usage was indeed useful in the earlier days when our knowledge of AGN and their related phenomena was much more limited. Nowadays we consider this view of AGN too simplistic, as the radio loudness distribution of AGN is not bimodal (Järvelä et al., 2015), and therefore other features need to be taken into account.

This paper will further delve into the description of AGN, distinguishing between the two approximate cathegories of radio-quiet and radio-loud AGN.

Initially, we will explore the main characteristics of Seyfert Galaxies, which

fall within the radio-quiet AGN category. Subsequently, we will focus on the description of radio-loud AGNs, as this research highlights the presence of jet emissions.

2.2.1 Seyfert Galaxies

Seyfert Galaxies were named after Carl K. Seyfert, who recognized that a subclass of spiral galaxies showed an exceedingly bright nucleus, peculiar emission spectra characterized mainly by broad emission lines in the optical band, which could not originate only from stars.

A Seyfert galaxy has a strongly emitting nucleus, but the host galaxy is clearly detectable. The original definition of the class was primarily morphological. They are defined as galaxies with high surface brightness cores, since if observed directly by a large telescope, a Seyfert galaxy looks like a normal distant spiral galaxy with a star superimposed on the center.

The definition has evolved thanks to subsequent spectroscopy so that Seyfert galaxies are now identified by the presence of broad, high-ionization emission lines.

Seyfert galaxies are further divided into two main categories based on their spectral features, as generally explained above for AGN: Seyfert 1 and Seyfert 2.

- **Seyfert 1** galaxies exhibit broad permitted emission lines that arise from gas clouds located in the BLR. They also display narrow emission lines, believed to originate from gas in the NLR.
- **Seyfert 2** galaxies show nuclei with weak or null nuclear continuum and emission lines not affected by variability. The observed emission lines come almost totally from the outer NLR.

The Spectral Energy Distribution (SED) of Seyfert galaxies is notably complex, reflecting a diverse ensembling of components that contribute across all the energy ranges. The observed spectrum encompasses the resultant emissions from an accretion disk, Compton emission modified by a population of relativistic electrons, emissions from broad and/or narrow emission line regions, as well as dusty absorbing material that may be heated by the AGN itself. Also contributions from star formation within the host galaxy can further complicate the SED.

2.2.1.1 Narrow Line Seyfert 1 Galaxies

A subset of the Seyfert-1 galaxies, are the so-called narrow emission line Seyfert 1 galaxies (NLS1). These sources are strong X-ray emitters, and they show a Hβ line which is narrower than general Seyferts (with FWHM < 2000 km s^{-1}).

NLS1s show strong X-ray variability but they vary only marginally in the UV. This could indicate that the accretion disk, as seen in the UV, is rather stable, while in the X-rays non-thermal beamed emission can be responsible for the variability. Optical studies seem to indicate that the black holes in NLS1 are still growing and their growth is governed by secular processes rather than by mergers.

Analysing these types of Seyfert galaxies, we are observing lines which are narrower than usual, but due to their shape and energy we know for sure they are coming from the BLR rather than from the NLR like the lines detected in Seyfert 2 galaxies.

The narrowness of the allowed spectral lines serves as an indicator of unique physical conditions that significantly differ from those found in other Seyfert

galaxies. Different explanations were suggested to understand the origin of these features.

It was proposed (Decarli et al., 2008) that the observed spectrum of Narrow-line Seyfert 1 (NLS1) galaxies could be attributed to the presence of a disk-like Broad-Line Region (BLR) that we are observing from a nearly head-on perspective. According to this scenario there is no component of the circular motion within the disk that is directed towards the observer, thereby avoiding the Doppler broadening effect.

An alternative explanation (Marconi et al., 2008) for the narrowness of BLR lines attributes this phenomenon to the radiation pressure exerted by an accretion disk that accretes close to the Eddington limit. This intense radiation pressure pushes the BLR to a greater distance from the central engine, leading the gas to move slower.

Some other studies suggested also that NLS1s hosted lower mass black holes in their inner region. These lower mass values, found mostly through reverberation mapping, lie usually within $10^5 - 10^7$ $M_\odot$.

For a fixed accretion rate value $\dot{M}$, higher M_{BH} values imply higher velocities and therefore broader emission lines, as a consequence of the virial theorem.

NLS1s are described as a "mixed bag" (Peterson, 2011) of sources that include both high Eddington rate accretors and low-inclination AGNs.

The observed complex spectral features display a pronounced soft excess emission below 1 keV and steeper X-ray photon indices values compared to Seyfert 1 galaxies. The strong X-ray variability is usually addressed to a higher accretion rate.

The morphology of the host galaxies of NLS1s is generally spiral, with often a

bar crossing the central region, with an extension of about 1 kpc with respect to the nucleus (Leighly, 1999a). Some studies suggest there is a correlation between the higher accretion rate and the observed bar in the center. This bar is an additional gravitating area which helps bringing the gas towards the central region causing the accreting material to increase towards the central area.

According to evolutionary theories, the presence of this bar suggests that the galaxy is in an initial phase of activity and is capable of further evolution (Salvato, 2002).

2.2.2 Radio-Loud AGN

Radio-loud AGN are a class of astronomical objects characterized by their strong radio emission compared to the other bands.

Radio-loud AGN are typically associated with the presence of highly energetic and collimated jets of charged particles, usually electrons, that emit synchrotron radiation in the radio frequency range and inverse compton scatter internal or external photons to high energies.

These sources also can exhibit variability in their radio and x-ray emissions, often associated with changes in the accretion rate onto the central black hole and the dynamics of the jet.

We further classify these objects in other two subclasses, primarily based on the angle α_{J} between the jet orientation and the line of sight.

- **Blazars**: Jet pointing towards the observer. In this case we see an extremely powerful emission, as the relativistic amplification is strongly effective. The jet emission represents the dominant source of radiation.

- **Radio Galaxies**: Jet forming a non-negligible angle α_{JET} with the line of sight. In this case, the relativistic amplification and superluminal effects become less significant. While jet emission persists across the electromagnetic spectrum, it may no longer be the dominant source of radiation. Instead, other nuclear and non-nuclear components come into play, especially in the infrared (IR), optical, and X-ray frequency ranges.

2.2.2.1 Blazars

Blazars, a contraction of BL Lac Object and Quasar, stand as extraordinary celestial entities known for their exceptional luminosity and energy output. When observed from telescopes on Earth, they are seen as point-like sources of light, a consequence of their elevate distance from our planet. These enigmatic entities radiate energy at a rate that can exceed that of an entire galaxy by thousands of times, and they are typically detected at high redshifts, which refers to their potentially considerable ages.

The Blazar Sequence, as delineated observationally by Fossati et al. (1998) and theorethically by Ghisellini et al. (1998), categorizes these objects into two distinct classes based on their spectral emissions:

- **Flat Spectrum Radio Quasars (FSRQs)**: showing presence of strong lines. It means they are surrounded by a so-called photon rich environment linked to an emitting accretion disk and surrounding gas.
- **BL Lacertae (BL Lac Objects)** : they lack conspicuous strong emission lines, implying a more photon-poor environment. These objects usually show stronger magnetic fields.

A criterion used to distinguish between FSRQ and BL Lacs is the equivalent width of the emission lines (EW) , and a dividing line of EW of 5 Å is applied.

BL Lac objects predominantly display lines with equivalent widths below this threshold, but it is essential to note that the continuum emission in blazars is highly variable, leading to corresponding fluctuations in the equivalent width of spectral lines.

The observed differences in spectral features are well explained by theoretical models that encompass radiative processes within blazar jets, primarily involving synchrotron radiation for the low-energy part and Inverse Compton (IC) scattering for the high-energy part:

- **Synchrotron radiation**: arises from electrons spiralizing around the magnetic field lines, generating low energy photons.
- **Inverse Compton scattering**: here arises when high energy electrons in the collimated jet scatter lower energy photons that were either previously produced from synchrotron radiation, or generated in the external environment.

We repeat that a further distinction is made between two cases of Inverse Compton scattering:

- **Synchrotron–Self–Compton (SSC)**: In this scenario, the seed photons for IC scattering are synchrotron photons produced by the same electrons responsible for the high-energy Compton component.
- **External Compton (EC)**: Here, the primary seed photons originate externally to the jet, such as from the accretion disk (Dermer and Schlickeiser, 1993), broad-line region (BLR) lines (Sikora et al., 1994), or torus (Błażejowski et al., 2000).

The visual representation of the Blazar Sequence demonstrates the relationship between jet power and accretion disk luminosity, a key parameter that varies

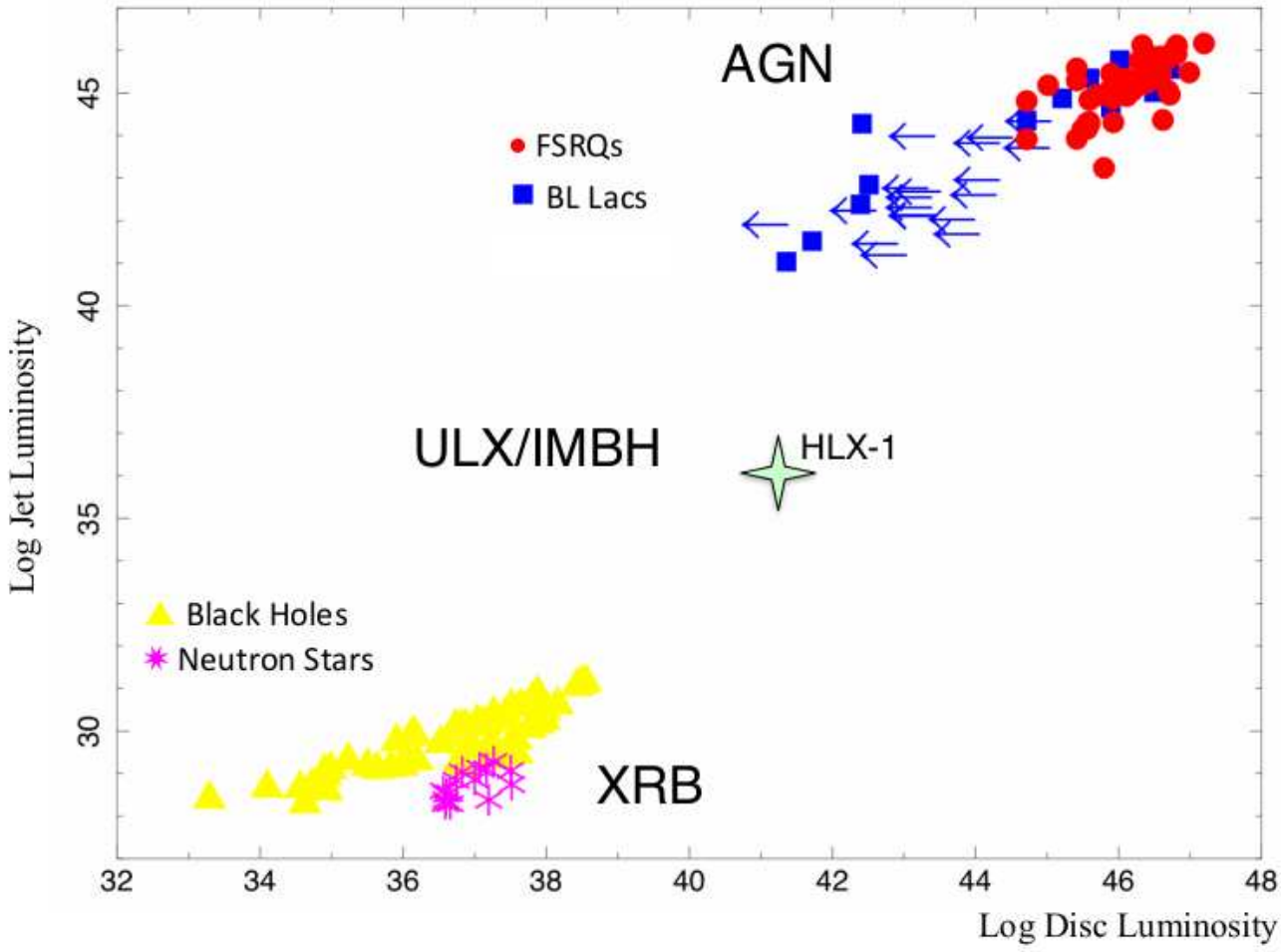

Figure 8: Jet Power as a function of the accretion disk luminosity, the main parameter that varies from BL Lacertae and Radio Quasar
(Foschini, 2017)

between BL Lacertae Objects and Radio Quasars.

In BL Lacs, the absence of evident thermal emission implies that the accretion process is not radiatively efficient. The lack of ionizing radiation further results in the absence of broad emission lines.

These properties can be explained if the accretion luminosity, relative to the Eddington limit, is below a critical threshold $L_{disk} \leq (10^{-2} - 10^{-3}) \cdot L_{Edd}$. In this case the jet emission mechanism is supposed to be dominated by Synchrotron Self Compton processes, not involving a significant amount of external photons as the environment appears to be depleted and poorly emitting.

In contrast, in powerful flat-spectrum radio quasars (FSRQs) we directly observe radiation from the accretion disk, broad emission lines, and the infrared torus component. This suggests that the high-energy emissions in FSRQs are likely a result of the external Compton (EC) process.

In both cases, the measured masses of the central black holes are similar, emphasizing that the power of their jets primarily depends on electron cooling influenced by the surrounding environment.

2.2.3 Jetted Narrow Line Seyfert 1 Galaxies

In 2008, the discovery of high-energy gamma-rays from Narrow-Line Seyfert 1 Galaxies (NLS1s) revealed the presence of active galactic nuclei that are capable of emitting powerful relativistic jets while showing differing features from blazars and radio galaxies.

NLS1s were conventionally not perceived as jet producers as they belong to the Seyfert Galaxies class. While early radio observations had previously hinted at jet emissions, it was the discovery of GeV γ-rays that was decisive, confirming that these AGN can indeed produce powerful relativistic jets, similar to the ones from blazars or radio galaxies (Abdo et al., 2009a, Abdo et al., 2009b).

A salient distinction between jetted NLS1 galaxies and the established blazars lies in the central black hole mass, a parameter found to be correlated with jet power.

The supermassive black holes residing at the heart of these peculiar NLS1 galaxies typically possess masses in the range of $10^6 - 10^8$ $M_\odot$.

Previously, relativistic jets were linked to higher mass SMBHs, placed in the centre of elliptical galaxies. It was commonly believed that a mass threshold existed in order to trigger the jet emission. Indeed, the discovery of powerful

relativistic jets in γ-NLS1s has expanded our characterization of AGN, raising intriguing questions about emission mechanisms and the purpose to compare AGN jets parameters with the ones of X-ray binaries (Foschini, 2014,Foschini, 2012a).

In this parallel, quasars in the blazar sequence occupy the position of stellar mass black holes in the X-Ray Binary (XRB) sequence, while γ-NLS1s occupy the equivalent position of neutron stars XRB. Consequently, concerning relativistic jets, gamma-ray-emitting NLS1s serve as the low-mass counterparts of blazars, just as neutron stars mirror the small-mass counterparts of galactic black holes.

Another peculiar feature, that distinguish γ-NLS1s from other radio loud AGN, refers to the extreme accretion values, up to 80% or even 90% of the Eddington limit. These values are the most extreme ever found in any γ-ray-emitting AGNs, but they are usual for NLS1s.

It is important to remark that usually Blazars are more likely to be found in elliptical galaxies, while γ-NLS1s are more likely to be detected in spiral galaxies. We can deduce that relativistic jets can form and develop independently of their host galaxies (Järvelä et al., 2018, Olguín-Iglesias et al., 2020).

Radio Loud Narrow Line Seyfert 1 Galaxies represent a hybrid class which has characteristics of the usually radio-quiet Seyfert galaxies but evidently showing to be radio-loud.

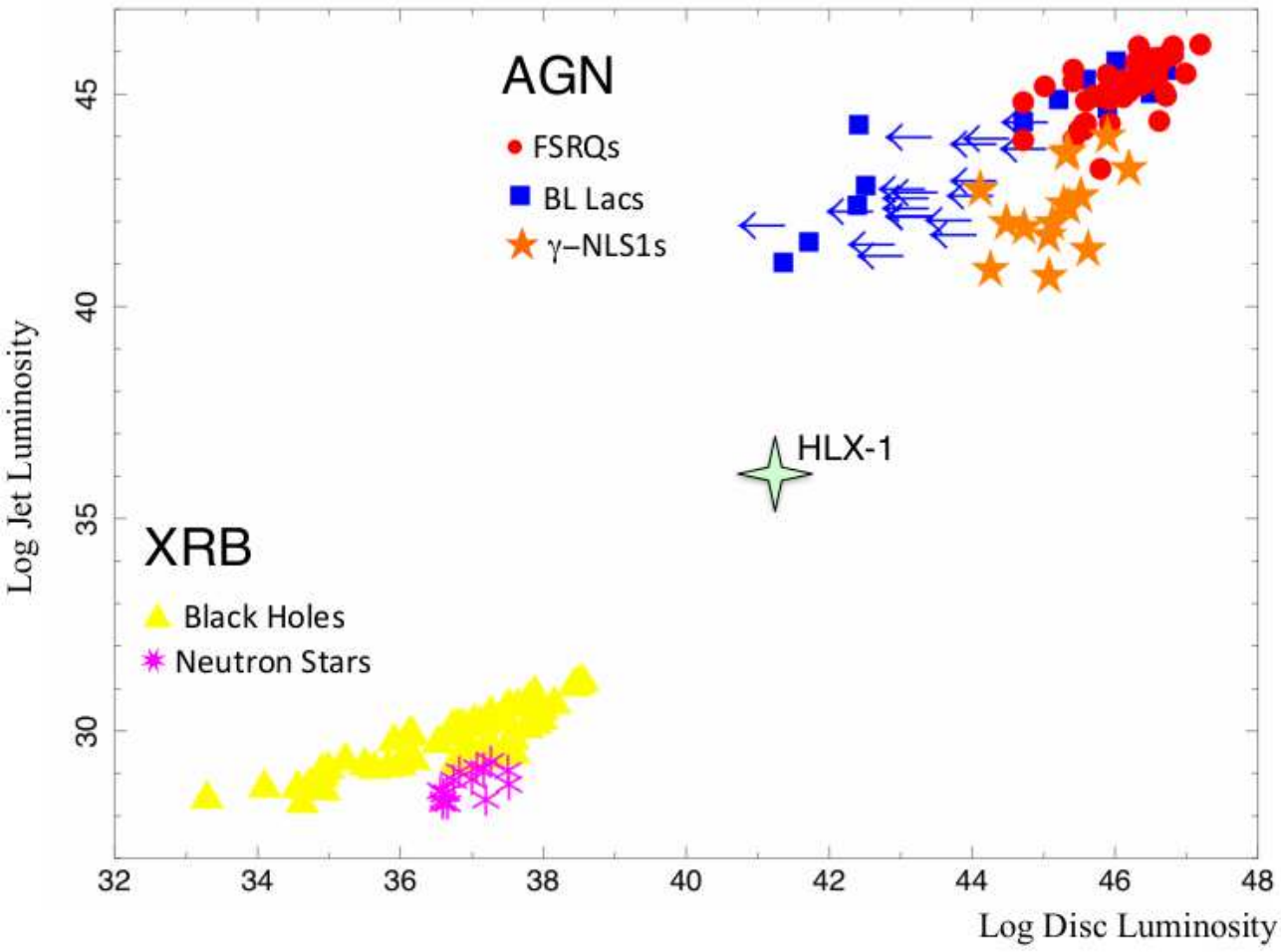

Figure 9: Jet Power as a function of the accretion disk luminosity with the addition of γ-NLS1 galaxies, whose jet emission is less powerlful in relation with their smaller BH mass (Foschini, 2017)

3. The case of 1H 0323+342

1H 0323+342 is a gamma-ray-emitting narrow-line Seyfert 1 galaxy (NLS1) and it is considered to be the closest gamma-ray-emitting NLS1 to Earth, with a redshift (z) of 0.063. Its ICRS coordinates (J2000) are RA=03h 24m 41.2 Dec=+34° 10' 45.8".

1H 0323+342 was discovered in 1993 with an optical follow up of HEAO sources (Remillard et al., 1993). It was classified as NLS1, but the discovery of radio emissions in 2007 suggested that it had relevant analogies with blazars (Zhou et al., 2007). In 2009 gamma emission was detected after the first year of Fermi operations. It is one of the first four NLS1 detected by Fermi.

3.1 Spectral Features

This source is radio loud, since its Radio-Loudness parameter R measures 318, and it also displays a flat radio spectrum.

It exhibits a double-hump Spectral Energy Distribution, characteristic of γ-NLS1s that peaks in the radio band and γ-rays implying synchrotron emission and synchrotron mechanisms that would result from a jet (Mundo et al., 2020).

However, while 1H 0323+342 has been firmly established as a radio-loud AGN, compelling evidence, drawn from the X-ray spectral shape and multiwavelength spectral energy distribution, suggests that its X-ray emissions below 10 keV predominantly originate from the accretion disk and corona, rather than from relativistic jets, contrasting with the behavior of radio-loud AGNs.

3.2 Mass of SMBH

In common with Seyfert 1 galaxies, which are typically radio-quiet AGNs, 1H 0323+342 houses a central SMBH characterized by a relatively lower mass value of order $10^7\,M_\odot$. The central BH mass has been determined through various methods, all yielding consistent results.

These methods encompass the evaluation of Hβ luminosity and Full Width at Half Maximum (FWHM) from a single-epoch spectrum, fitting the accretion disk based on the Shakura–Sunyaev model, analyzing excess variance at X-rays, and employing reverberation mapping techniques (Wang et al., 2016). These methodologies converge to estimate the central black hole mass in the range of 1.0-3.5 x 10^7 solar masses, with the most likely value being approximately: $2.2 \times 10^7 M_\odot$.

3.3 Structure of 1H 323+342

In the following, I summarize the basic features of the structure of 1H 0323+342 as found by Foschini et al. (2019).

The structural characteristics of 1H 0323+342 provide valuable insights into its inner mechanisms. The boundary separating the Broad Line Region from the molecular torus is established at a dust sublimation radius of approximately 0.19 parsecs. The temperature at which dust sublimation occurs is estimated to be around 1500 Kelvin. The outer boundary of the torus is situated at a distance of approximately 5.7 parsecs from the central black hole.

To investigate the extent of the Narrow Line Region, researchers have utilized the luminosity of the [OIII] λ_{5007} emission line. The profile of this emission line has been significantly affected by turbulence, likely due to interactions with

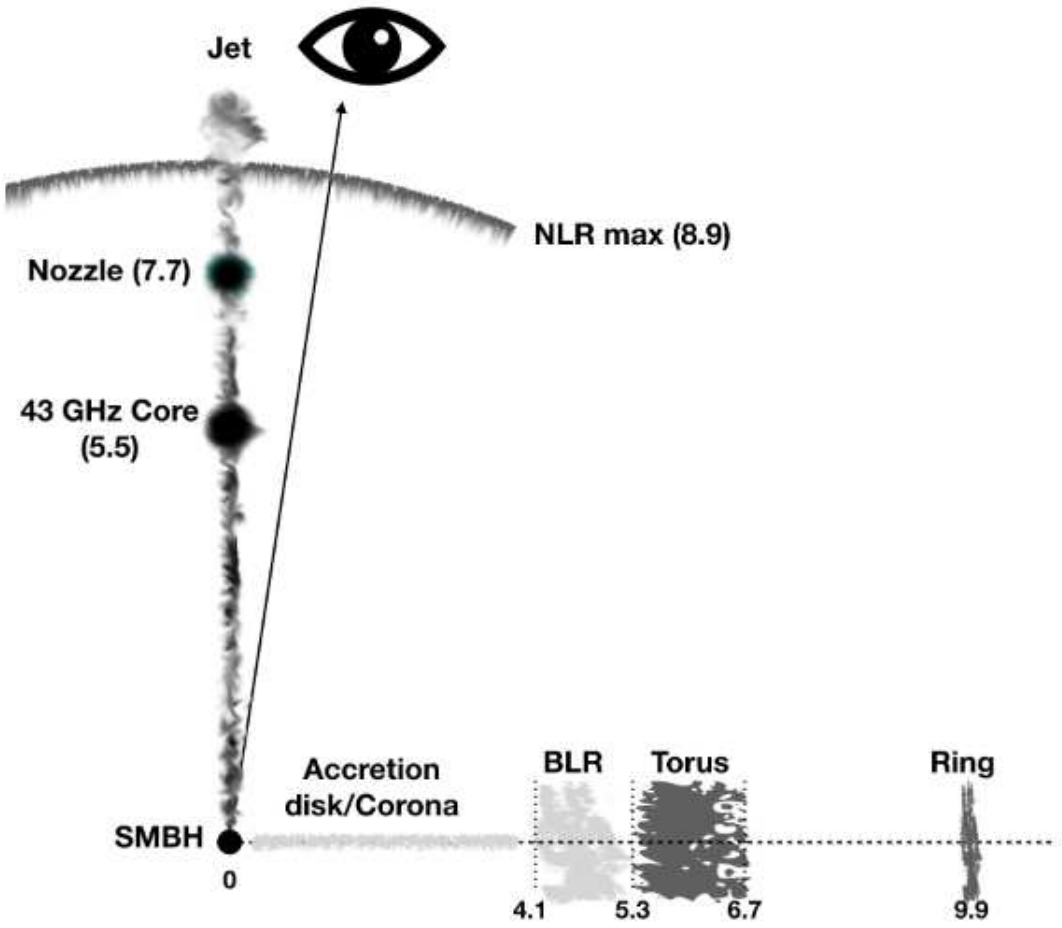

Figure 10: Structure of 1H 323+342
(Foschini et al., 2019)

the relativistic jet. As a result, the maximum extension of the NLR has been determined to be approximately 794 parsecs.

The host galaxy of 1H 0323+342 exhibits a ring (Zhou et al., 2007) that was interpreted as spiral arm structure with a radius of approximately 7.5", or a merger remnant (Antón et al., 2008).

The specific viewing angle of 1H 0323+342 remains unknown, but certain clues about its orientation can be deduced. Since the structural features, such as the ring/spiral arm, developed along the equatorial plane of the central black hole, and since the jet emanates perpendicularly to the black hole equator, the

viewing angle of the ring/spiral arm is likely to be the complementary angle of the jet viewing angle, estimated to be approximately 9 degrees. This viewing angle was determined by measuring the Doppler factor from the variability in the light curves and the kinematics of the components within the jet.

The structure of the relativistic jet in 1H 0323+342, when observed at high-resolution radio frequencies, exhibits an inner region with a parabolic shape and an outer region with a conical shape.

4. Observing instruments

1H 0323+342 has been subject to extensive monitoring through the Swift satellite, with observations conducted in both the X-ray and UV/optical wavelength ranges. This observational campaign spans a duration extending for more than sixteen years, from 2006 to 2023. The foundation of the analysis presented herein draws from a substantial dataset, specifically utilizing a collection of 170 observations curated from the Swift satellite archive.

4.1 Swift

The Swift satellite is a space observatory born with the aim to detect Gamma Ray Bursts, and other transient astronomical events, by observing these short-lived high-energy phenomena across various wavelengths, including soft and hard X-rays, ultraviolet (UV) and optical light.

Launched on November 20, 2004, by NASA in collaboration with international partners, it is orbiting around Earth performing a Low Earth Orbit, with a distance from our surface between 584 and 601 km (Gehrels et al., 2004).

Swift is equipped with three principal instruments, each tailored to capture and scrutinize specific aspects of the transient events it encounters. These instruments include the Burst Alert Telescope (BAT), responsible for detecting GRBs, the X-ray Telescope (XRT) for X-ray observations, and the Ultraviolet/Optical Telescope (UVOT), which handles observations in the ultraviolet and optical spectra. Together, these instruments enable Swift to provide comprehensive insights into the dynamic and rapidly evolving phenomena occurring

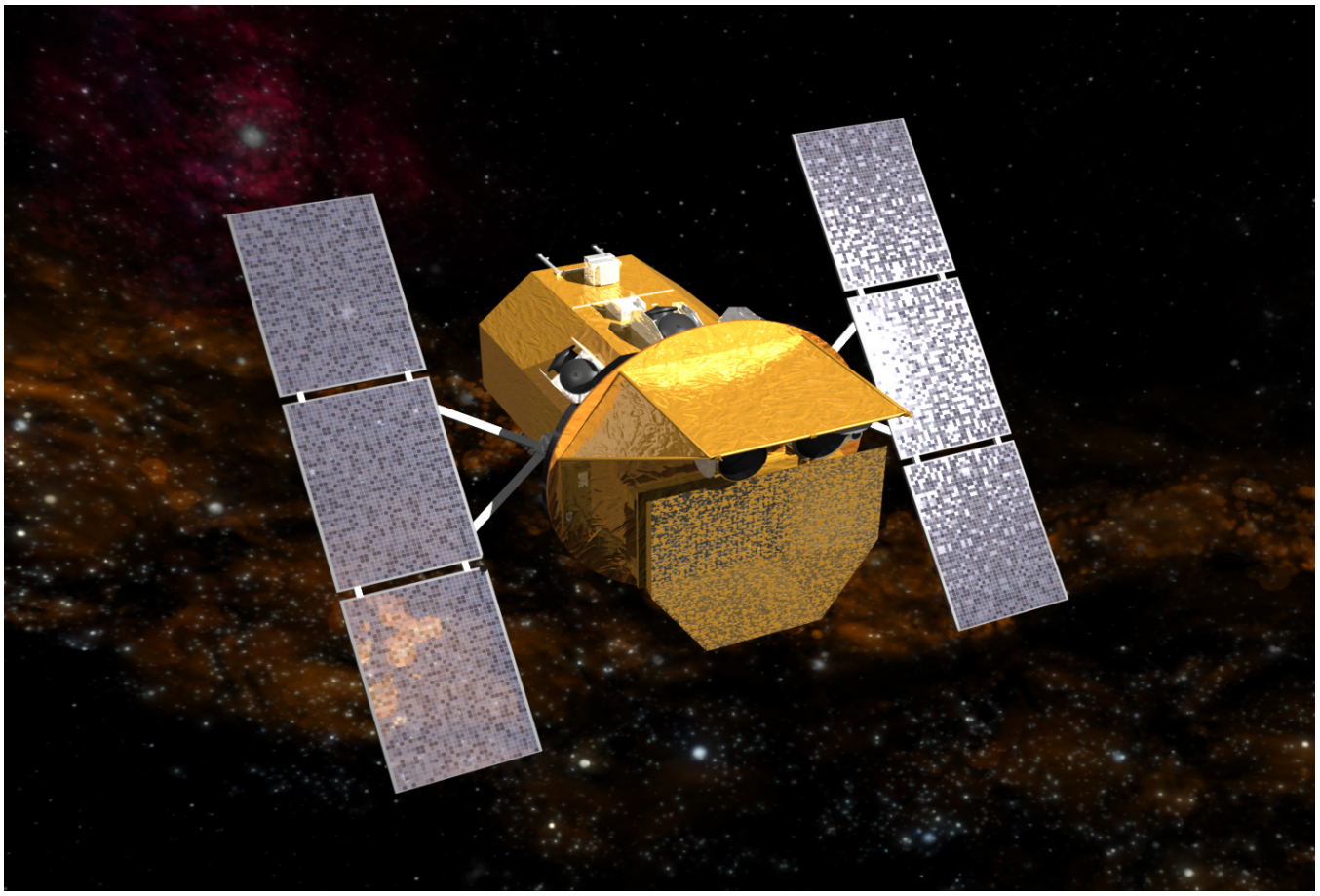

Figure 11: Swift Telescope

Credit: NASA

in our universe.

4.1.1 Burst Alert Telescope (BAT)

The Burst Alert Telescope is Swift's primary instrument for detecting and localizing Gamma Ray Bursts. It operates in the hard X-ray energy range (15 keV to 150 keV) and has a wide field of view, allowing it to rapidly detect and locate GRBs within seconds (Barthelmy et al., 2005). The BAT can trigger the other instruments of the spacecraft to observe the afterglows of GRBs in different wavelengths.

4.1.2 X-ray Telescope (XRT)

The X-ray Telescope is responsible for observing the X-ray afterglows of GRBs and other high-energy sources. It operates in the X-ray energy range of 0.2 keV to 10 keV. The XRT is designed to provide detailed images and spectral information of the X-ray emissions, allowing scientists to study the physical properties of the emitting sources, such as the characteristics of the accretion disks around black holes in AGNs (Burrows et al., 2005).

The XRT employs a grazing incidence Wolter I telescope to focus X-rays onto the spare MOS CCD of XMM. This CCD has dimensions of 600x602 pixels and is equipped with four calibration sources positioned at each corner of the detector, emitting X-rays at 5.9 keV and 6.4 keV, providing the calibration references.

The effective area of the XRT is determined by three main components: the mirror area, the filter transmission, and the CCD Quantum Efficiency (QE). The ancillary response files (ARF) contain information regarding the mirror area and filter transmission, which is akin to the XMM-MOS medium filter, incorporating corrections for vignetting and point spread function losses. The CCD QE is accounted for by the Redistribution Matrix Files (RMFs), which vary depending on the operating mode and the choice of grades selected.

The XRT Telescope can operate in two primary states: Auto and Manual state. The Manual state is predominantly used for calibration purposes, with science modes selected for specific observations. In contrast, the Auto state is the normal operating mode in which the XRT autonomously selects the appropriate science mode based on the source count rate, enhancing efficiency and adaptability.

Within both Auto and Manual states, the XRT can operate in various science modes, including Image Long and Short (IM), Low rate (LR), Piled-up Photodiode (PU), Windowed Timing (WT), and Photon Counting (PC).

Here, we specifically focus on Photon Counting mode, known for its ability to retain full imaging and spectroscopic resolution, all while accumulating data across the full field of view every 2.5 seconds. This mode is indeed particularly advantageous for studying X-ray emissions in detail.

4.1.3 Ultraviolet/Optical Telescope (UVOT)

UVOT is Swift's instrument for observing sources in the ultraviolet and optical parts of the electromagnetic spectrum. UVOT makes Swift a complete multi-wavelength facility. Coaligned with XRT, UVOT provides simultaneous ultraviolet and optical coverage: 170-650 nm, in a $17' \times 17'$ field with a magnitude limit of 24, observing in six filters, namely V,B,U,W1,M2, and W2.

Despite its limited aperture, UVOT is a powerful complement to other instruments because of its UV capabilities and the absence of atmospheric extinction, diffraction, and background (Roming et al., 2000).

Since UVOT has photon counting detectors, which are able to retain individual photon positions and timing information, it operates in a mode more similar to typical X-ray telescopes rather than typical optical telescopes.

As soon as a Gamma-Ray Burst (GRB) is detected and pinpointed by the Burst Alert Telescope (BAT), the spacecraft reorients itself to align both the UVOT and the X-ray Telescope (XRT) with the location of the GRB.

The spacecraft's rapid 20-70 second time-to-target capability means that approximately 100 GRBs per year can be observed by the narrow-field instruments during the afterglow phase.

Upon acquisition of a new GRB by the spacecraft, the UVOT follows a predetermined sequence of exposure times and filter combinations. The initial images are promptly transmitted to Earth for use as reference charts by ground-based observers. These images are also compared to archival observations of the same portion of the sky to detect any changes that might indicate the presence of an optical counterpart to the GRB.

4.2 Fermi Gamma-ray Space Telescope

The Fermi Gamma-ray Space Telescope, also known as FGST or Fermi, is a space-based observatory designed for conducting gamma-ray astronomy observations in low-Earth orbit.

Fermi's precursor was the EGRET telescope on the Compton Gamma-Ray Observatory (CGRO), launched in 1991. It spanned a energy range of 30 keV-30 GeV and was then revolutionary since this range was previously unexplored with such sensitivity. From its development and improvement, Fermi was created, covering a energy range of 8 keV-300 GeV.

Initially named the Gamma-Ray Large Area Space Telescope (GLAST), the mission was later renamed in honor of physicist Enrico Fermi following its successful launch in 2008.

This mission represents a collaborative effort involving NASA, the United States Department of Energy, as well as various agencies and research institutes in France, Germany, Italy, Japan, and Sweden. As of early 2021, Fermi had completed its 70,000th orbit around the Earth.

The Fermi satellite is equipped with two types of detectors; the Large Area Telescope (LAT) and the Gamma-ray Burst Monitor (GBM) where its primary tool for detection is the LAT.

4.2.1 Large Area Telescope (LAT)

The Large Area Telescope (LAT) is the primary instrument on the Fermi Gamma-ray Space Telescope. It is a high-energy γ-ray telescope covering an energy range from below 20 MeV to over 300 GeV. The LAT is a collaborative effort involving multiple countries and institutions.

Figure 12: Fermi Telescope

Credit: NASA

It consists of a precision tracker, calorimeter, anticoincidence detector, and data acquisition system. The tracker has silicon strip detectors and tungsten material for tracking, while the calorimeter uses CsI(Tl) crystals for energy measurement (Atwood et al., 2009).

5. Data Analysis

I have retrieved data from the Swift archive on the High Energy Astrophysics Science Archive Research Center (HEASARC), downloading 170 datasets taken from XRT and UVOT telescopes, starting from 2006.

The primary goal of my analysis was to derive the key physical parameters related accretion and ejection processes that are occurring within this AGN. To achieve this, fitting models were applied to the available spectroscopic data, and and the quality of these fits as well as the robustness of the proposed models were assessed using two main tests:

1. χ^2 **Test**: this test is applicable when a large number of counts are available, typically requiring at least 20 counts per bin in binned data.

   In statistics we define

   $$\chi^2 = \sum \frac{(\mathrm{O} - \mathrm{E})^2}{\mathrm{E}} \tag{5.1}$$

   with O being the observed values and E the expected ones.

   The quality of the fit is determined by the reduced χ^2: the χ^2 value divided by the number of degrees of freedom (d.o.f), which is the number of energy channels minus the number of fitted parameters.

   A reduced χ^2 value close to 1 is indicative of a good fit. On the other hand, significantly greater values may lead to rejection, indicating that the model does not fit the data properly, while values much less than 1 could signify oversampling.

2. **Maximum Likelihood Test**: also known as C-statistics, this test is applied in case there are insufficient counts to generate a meaningful number of bins, due to a decrease in source rate or the source's intrinsic weakness for the instrument's performance. In this case the χ^2 test is no longer applicable.

   This method calculates the joint probability that each individual event fits the selected model without the need for binning. It computes the probability of the model fitting each event and forms the likelihood function as the product of these probabilities. The maximum of this function reveals estimates of the model's parameters (Mattox et al., 1996). However, one limitation of the likelihood method is its inability to provide a measure of the fit's quality, as it only indicates the probability of obtaining the observed results without offering information about the overall goodness of the fit.

   In the case of EGRET and Fermi LAT, the likelihood ratio is preferred as a test that is called (Mattox et al., 1996):

   TS, **Test Statistic**, defined as

$$\mathrm{TS} = 2 \ln \frac{\mathrm{L}_{\mathrm{max},0}}{\mathrm{L}_{\mathrm{max},1}} \tag{5.2}$$

   It is used for example when the optimizers of Fermi LAT find the best fit spectral parameters, but not the location. To overcome this issue, a tool that performs a grid search mapping out the maximum likelihood value over a grid of locations is provided.

   So in this case $\mathrm{L}_{\mathrm{max},0}$ is the maximum likelihood value for a model without

an additional source, the null hypothesis, and $L_{max,1}$ is the maximum likelihood value for a model with the additional source at a specified location.

In the limit of a large number of counts the TS for the null hypothesis is asymptotically distributed as χ^2_x, where x is the number of parameters characterizing the additional source.

In practice, a larger TS indicates that the null hypothesis is incorrect, implying the presence of an additional source. The square root of the TS is approximately equal to the detection significance for a given source, providing a quantifiable measure of the source's presence and importance.

5.1 XRT data analysis

XRT observations were selected in the photon-counting mode and the data are reduced using the task `xrtpipeline`, from the Swift `FTOOLS` in `HEASOFT 6.31.1` and calibration database (`CALDB`) updated on September 11, 2013.

Once the spectra were obtained, it was necessary to add calibration files to the header of the spectrum. Using `grppha` command the associated redistribution matrix file and the associated ancillary response file were included for each observation.

Spectral files are in PHA format. The PHA file contains such information as integration time, detector effective area, and a scaling factor that estimates the expected size of the internal background. It contains also the total observed counts for a number of channels and a factor for the size of any systematic error.

Also, data were grouped in order to have at least 20 counts per bin, with the purpose to obtain a valid χ^2 statistics on our models.

When χ^2 is a valid statistic, we know that its value is drawn from a known distribution and we can use the probability of obtaining the observed value as a goodness-of-fit measure. This is the case of a large number of degrees of freedom. However, when χ^2 is not a valid statistics we cannot obtain a goodness-of-fit measure as we do not know the distribution from which the maximum likelihood value is drawn.

For most of the observations taken between MJDs 58332 and 58451 (2018-08-02, 2018-11-29), due to a significantly decreased exposure time, and therefore less counts in the derived spectra, χ^2 statistics was not valid, so I chose to apply the C-statistics keeping 1 count per bin in the spectra.

Spectra were then analysed through the software `XSPEC`: a command-driven,

interactive, X-ray spectral-fitting program. Through this software I wanted to measure the photon index values aiming to search for correlations with the source's flux in the X-ray band.

`XSPEC` was able to measure these quantities by letting the user choose spectral models, described in terms of few parameters, and then enabling to match or fit them to the data obtained by the spectral observations.

It takes as input files the PHA format, containing also the total observed counts for a number of channels and a factor for the size of any systematic error. Each channel is then converted to a count rate per unit area. For each spectrum, channels are converted to count rates per unit area, and channels with a quality flag of 5 were further excluded with the command `ignore bad`. Additionally, only events in the range 0.3-10 keV were kept for the analysis.

To begin the analysis, a specific absorption model, `tbabs`, was applied. This model calculates the cross-section for X-ray absorption by the interstellar medium (ISM), encompassing gas-phase ISM, grain-phase ISM, and ISM molecules. The only parameter that varies in the `tbabs` model is N_H, representing the equivalent hydrogen column in units of 10^{22} atoms cm^{-2}. For our source, this value was frozen at the galactic value of $0.117 \cdot 10^{22}$.

As the underlying physical process generating X-ray emission involves Comptonization of seed photons by energetic electrons in a hot plasma cloud, it has been demonstrated that power law spectra are exact solutions to the radiative kinetic equation. This analytical solution for spectral slope is applicable without any restrictions on plasma physical parameters.

Hence, two models, `zpowerlaw` and `zbknpower`, were compared to study the spectral slope of photon counts and the influence of emitted jets. The former is a powerlaw model incorporating redshift, aiming to approximate the spectrum

while no jet emission is occurrig, and the latter is a broken powerlaw model, consisting of two separate powerlaws, each dominating a distinct energy range of the spectrum with the higher energy range that is supposedly related to the plasma ejection. The redshift parameter was frozen at 0.063.

Once data have been read in and a model was defined, `XSPEC` used a fitting algorithm to minimize the fit statistic, thus determining the best-fit values for the model parameters. At the conclusion of each fitting, `XSPEC` generated a record of the best-fit parameter values. Additionally, using the `err` tool, it provided estimated confidence intervals, calculated at the 90% confidence level from the second derivatives of the fit statistic with respect to the model parameters at the best-fit point.

In case both models provided meaningful results, showing accurate parameters and reduced χ^2 close to 1, the `ftest` tool was employed as a tool to choose which model between `zpow` and `zbknpower` was the best fit. It takes as input the two χ^2 from both models and their respective degrees of freedom. Than it computes the F-statistics giving out F-test probability. If

$$1 - \mathrm{P}_{\mathrm{Ftest}} > 99.7\% \tag{5.3}$$

it means the additional model is preferred with a probability of at least 3σ, so it is reasonable to add the extra model component and therefore choosing `bknpower` model.

Eleven observations were better described by a broken-powerlaw. These data were taken during: 53925.452, 54479.353, 54786.733, 55045.032, 55499.098, 55525.794, 55527.735, 55528.137, 56356.608, 56492.098, 57257.625 MJDs (that correspond to ISO 8601 dates: 2006-07-09 10:50:52.800, 2008-01-14T 08:28:19.200,

2008-11-16 17:35:31.200, 2009-08-02 00:46:04.800, 2010-10-30 02:21:07.200, 2010-11-25 19:03:21.600, 2010-11-27 17:38:24.000, 2010-11-28 03:17:16.800, 2013-03-05 14:35:31.200, 2013-07-19 02:21:07.200, 2015-08-23 15:00:00.000).

To calculate the flux in the energy band 0.3-10 keV, the model `cflux` was applied. This is a convolution model to calculate the corrected logarithmic flux of other model components in units of ergs/cm^{2}s^{-1}.

The essential parameters that `zbknpower` enabled to measure were:

- **BreakE**: the Energy Break, which is the energy value in keV units at which the second powerlaw starts to dominate the spectrum.
- **PhoInd1**: the photon index of the soft powerlaw emission which dominates the lower energy band of the spectrum, $\Gamma_1 > 1.9$.
- **PhoInd2**: the photon index of the hard powerlaw emission which dominates the higher energy band of the spectrum, supposed to be influenced by the jet, $\Gamma_1 < 1.9$.

Data derived from fittings with `zpowerlaw` were used to obtain an initial approximation of the spectral slope and flux. Also for the datasets that were better modeled by `zbknpower`, the parameters of `zpowerlaw` still offered a rough estimate for the average spectral slope and flux. These values were retained for the purpose of comparing all photon indices and fluxes, thus allowing for a general analysis of the spectral variations over time.

I noticed that data fitted with broken-powerlaw show above average fluxes. However, other observations that were modeled by a simple powerlaw with both hard and softer photon index show fluxes in the same range. Deeper insights were needed to understand better the origin of the jet and the increased flux values.

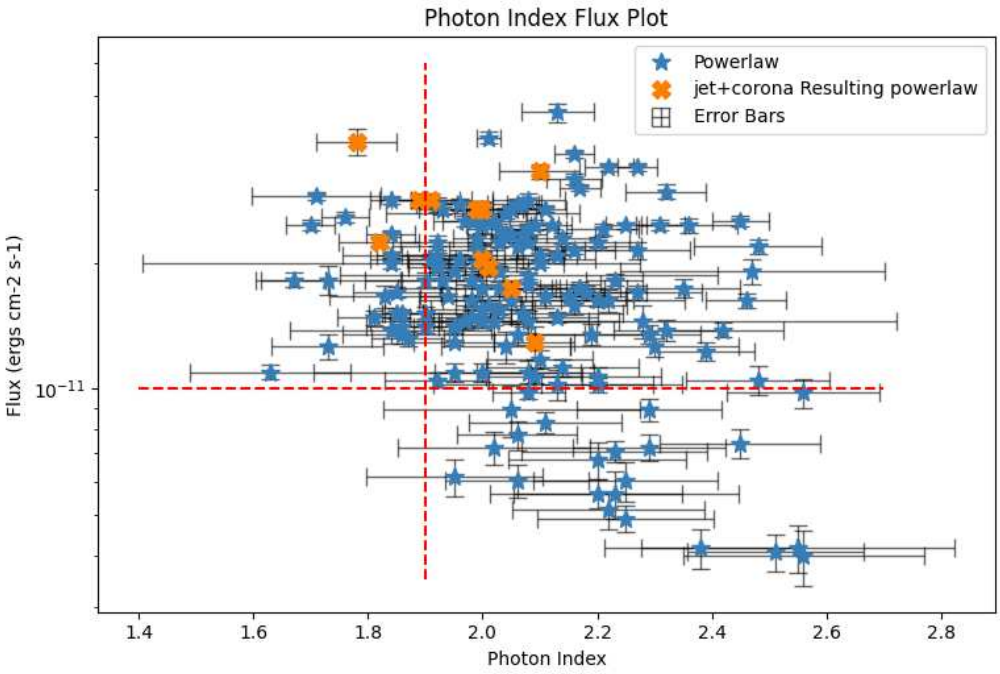

Figure 13: Areas of different Photon Index and Flux power. The area on the bottom left is the "Zone of Avoidance"

I therefore created a light curve over the 16 years observing time, to monitor the flux variations over this period, relating them to the respective photon indices.

I also distinguished three areas in the photon-flux graph:

1. *Zone 1*: $\Gamma < 1.9$ & $F > 10^{-11}$ ergs cm^{-2} s^{-1}.
2. *Zone 2*: $\Gamma > 1.9$ & $F > 10^{-11}$ ergs cm^{-2} s^{-1}.
3. *Zone 3*: $\Gamma > 1.9$ & $F < 10^{-11}$ ergs cm^{-2} s^{-1}

Where F is the flux value and Γ is the powerlaw photon index.

Generally speaking, *zone 1* refers to the "harder when brighter" phase, *zone 2* is the "softer when brighter" phase, while *zone 3* is hypothesized to be associated with a reduction in inner activity of an unknown nature.

I added together spectra from all observations belonging to each *zone* with the `addspec` tool.

For the average *zone* 1 I found that a broken powerlaw was the best fit model, displaying a reduced $\chi^2 = 466.54/350$ closer to 1 than the single powerlaw model with $\chi^2 = 484.68/352$. Modeling *zone* 2, a broken powerlaw did not fit well the data, while s single powerlaw model constituted a better fit yelding $\chi^2 = 643.12/472$. However there was still a soft excess leaving significant residuals below 2keV, so I applied a `zbbody` as an addition to the single powerlaw.

`zbbody` is an additive model of redshifted black-body radiation. It provides a black-body spectrum from a given peak temperature, and gives the spectrum from the Stefan-Boltzmann and Planck laws. The parameters are the maximum temperature kT (in keV units) of the inner disk, the norm and the redshift z.

The addition of `bbody` model improved significantly the fit, as the reduced χ^2 value had lowered to 562.53/64.

For the averaged *zone* 3 spectrum, a single powerlaw model was sufficient as the reduced χ^2 statistic value was 130/124.

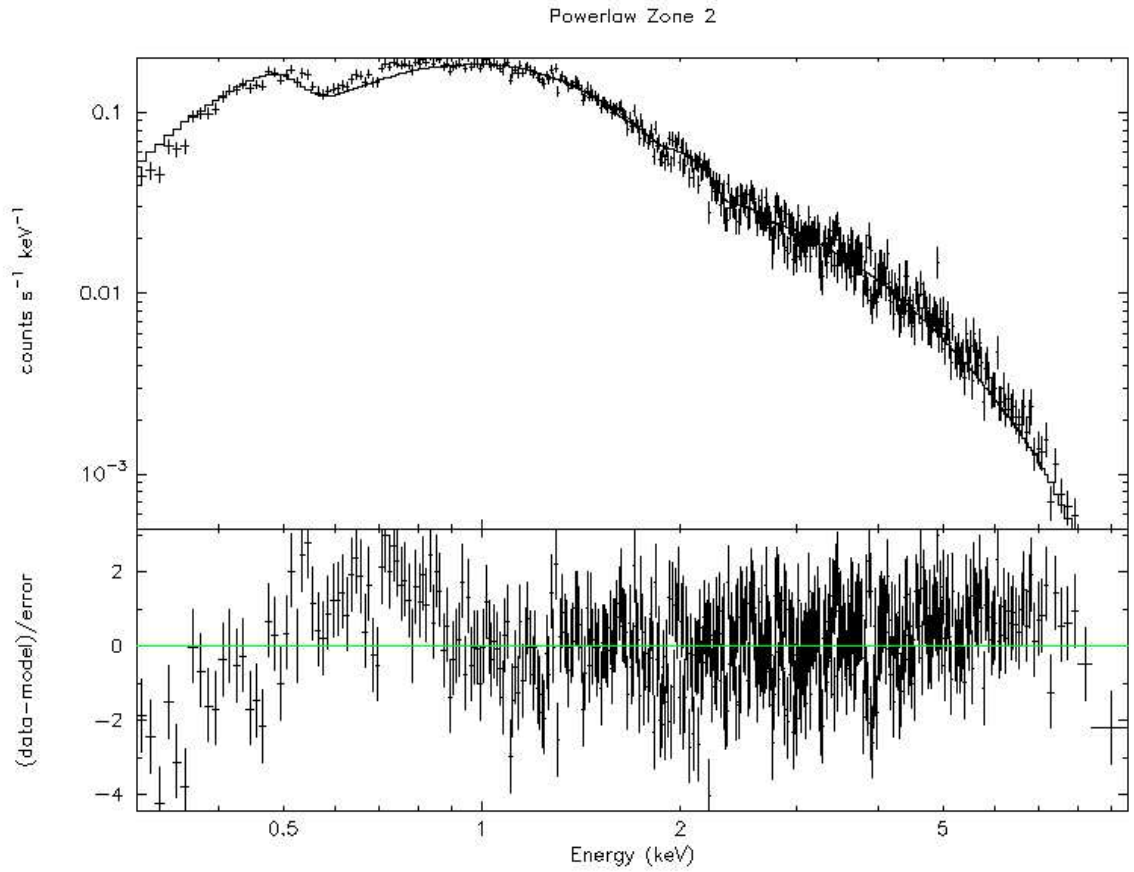

Figure 14: Plot with residuals of powerlaw model for *zone* 2

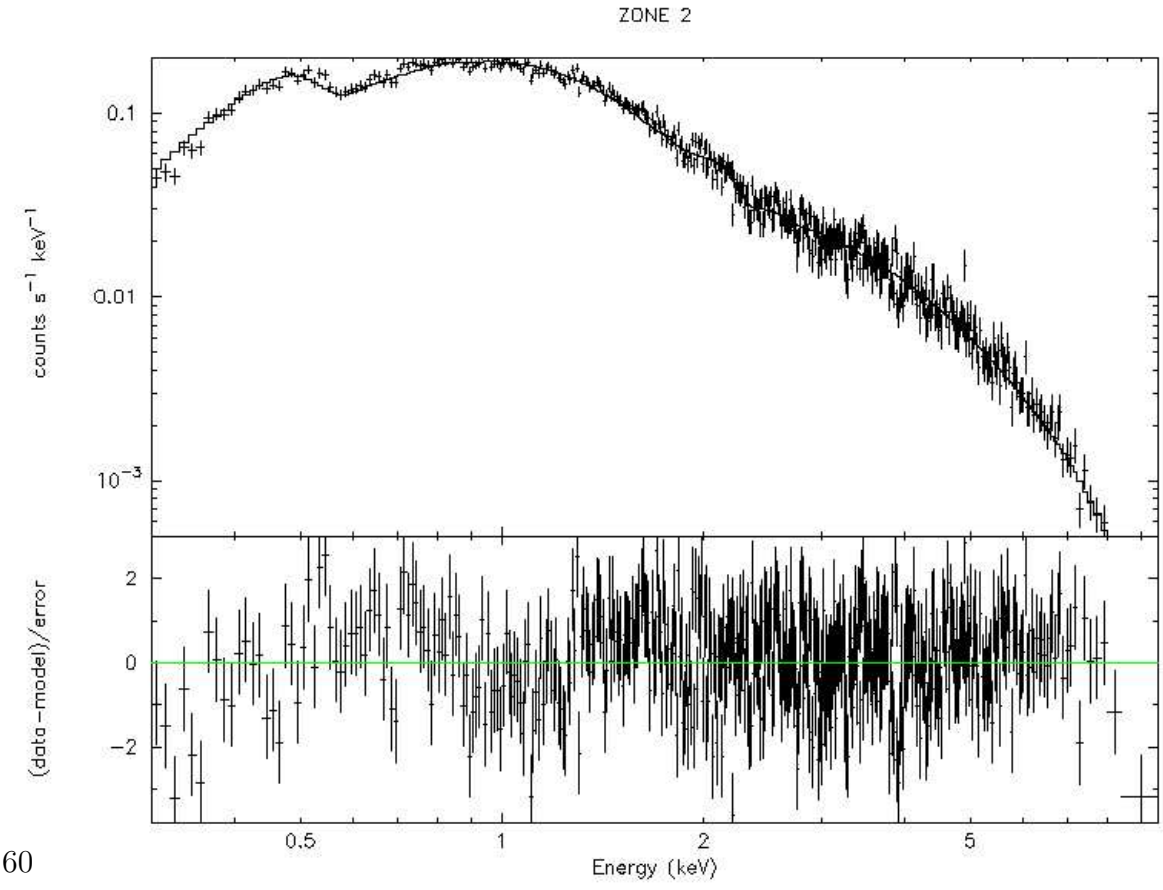

Figure 15: Plot with residuals of zbb+powerlaw model *zone*2

5.2 UVOT data

During most of the Swift observations, the object was also observed with UVOT in all the six passbands in the optical: V, B, U bands and near UV: W1, M2, W2 bands.

Since the sum of UVOT exposures is useful both to detect faint sources and improve the signal-to-noise ratio, data were summed using the tool `uvotimsum`.

The obtained FITS files were analysed with the tool `uvotsource`. This tool performs aperture photometry on a single source in a UVOT SKY exposure. It returns information about the count rate from the source, the source's magnitude in both Vega and AB systems, and flux density information. For this project I chose to use Vega magnitudes.

The source extraction region and background region obtained through `SAOImageDS9` were specified in the FK5 coordinate system.

The observed magnitudes needed to be corrected for extinction. To first evaluate the extinction A_V in the V band the following calculation was performed (Allen and Cox, 2000):

$$A_V = N_H \cdot 5.3 \times 10^{-22} \tag{5.4}$$

Where N_H is the galactic hydrogen column density, measuring: $N_H = 1.17 \times 10^{21}\,cm^{-2}$.

In order to obtain the different extinctions for all the five magnitudes in the remaining bands I used Cardelli laws (Cardelli et al., 1989).

Subsequently, the corrected magnitudes at all six wavelengths were transformed into flux values using the zero-point magnitudes given in the `HEASOFT` package:

$$\mathrm{zp_V} = 17.89,\ \mathrm{zp_B} = 19.11,\ \mathrm{zp_U} = 18.34,\ \mathrm{zp_{W1}} = 17.44,\ \mathrm{zp_{M2}} = 16.85,\ \mathrm{zp_{W2}} = 17.38. \quad (5.5)$$

I evaluated the total optical flux by summing fluxes in the V, B and U bands. In the same way I calculated the UV flux by summing in the W1,M2,W2 bands.

Unfortunately only few were are available in the periods ranging from MJD 55500.569 to 55529.141 (2010-10-31 13:39:21.600, 2010-11-29 03:23:02.400) and 58304.463 to 58465.058 (2018-07-05 11:06:43.200, 2018-12-13 01:23:31.200). Nonetheless, a total of 110 fluxes were obtained throughout the Swift observation time.

Corrected fluxes for each band were used to evaluate the optical and ultraviolet spectral index, α_{opt} and α_{UV} respectively.

$$\alpha_{\mathrm{opt}} = \frac{-\log \frac{\mathrm{S_V}}{\mathrm{S_U}}}{\log \frac{\nu_{\mathrm{V}}}{\nu_{\mathrm{U}}}} \quad (5.6)$$

$$\alpha_{\mathrm{UV}} = \frac{-\log \frac{\mathrm{S_{W1}}}{\mathrm{S_{W2}}}}{\log \frac{\nu_{\mathrm{W1}}}{\nu_{\mathrm{W2}}}} \quad (5.7)$$

Here $\mathrm{S_V}, \mathrm{S_U}, \mathrm{S_{W1}}$ and $\mathrm{S_{W2}}$ are the V, U, W1, W2 bands flux densities respectively and $\nu_{\mathrm{V}} = 5.56 \times 10^{14}\,\mathrm{Hz}$, $\nu_{\mathrm{U}} = 8.57 \times 10^{14}\,\mathrm{Hz}$, $\nu_{\mathrm{W1}} = 1.16 \times 10^{15}\,\mathrm{Hz}$, $\nu_{\mathrm{W2}} = 1.48 \times 10^{15}\,\mathrm{Hz}$ are the respective frequencies.

Errors $\sigma_{\alpha_{\rm opt}}$ and $\sigma_{\alpha_{\rm UV}}$ were evaluated through the formulas:

$$\sigma_{\alpha_{\rm opt}} = \frac{\partial \alpha_{\rm opt}}{\partial {\rm M_V}} \sigma_{\rm M_V} + \frac{\partial \alpha_{\rm opt}}{\partial {\rm M_U}} \sigma_{\rm M_U} \tag{5.8}$$

and

$$\sigma_{\alpha_{\rm UV}} = \frac{\partial \alpha_{\rm UV}}{\partial {\rm M_{W1}}} \sigma_{\rm M_{W1}} + \frac{\partial \alpha_{\rm UV}}{\partial {\rm M_{W2}}} \sigma_{\rm M_{W2}} \tag{5.9}$$

Where $\rm M_V$, $\rm M_U$, $\rm M_{W_1}$, $\rm M_{W_2}$ are the magnitudes in the V,U,W1,W2 band and $\sigma_{\rm M_V}, \sigma_{\rm M_U}, \sigma_{\rm M_{W1}}$ and $\sigma_{\rm M_{W2}}$ are their respective errors previously evaluated through `uvotsource`.

5.3 Fermi LAT data

Fermi LAT light curves were already supplied from the Fermi LAT Light Curve Repository. I downloaded the 3 days cadence ones with free photon index.

Observations were taken from August 2008 and data provided information on Julian Dates, Mid point of time bin in Mission Elapsed Time (MET), The likelihood Test Statistic (TS), Photon Flux between 0.1 and 100 GeV with its error and Photon Index with its error.

A larger TS indicates that the null hypothesis is incorrect i.e. a source really is present which can be quantified.

The square root of the TS is approximately equal to the detection significance for a given source, so I discarded data with TS lower than 4.

Also only data whose flux error was $\sigma_{\rm F} < 3 \times 10^{-1}\,{\rm F}$ were considered.

As for XRT and UVOT observations I collected and plotted flux and photon index values over time, to compare variations with the other bands.

6. Results and Discussion

6.1 XRT Data

X-ray observations show variations among the inferred parameters, specifically: Photon Index of the powerlaw models Γ and the flux values between 0.3-10.0 keV.

6.1.1 3 phases overview

In the plot representing photon index and flux values I noticed that data are distributed in three areas of the graph as I introduced in the previous paragraphs.

1. **Zone 1**: $\Gamma < 1.9$, F $> 10^{-11}$ ergs cm^{-2} s^{-1},
2. **Zone 2**: $\Gamma > 1.9$, F $> 10^{-11}$ ergs cm^{-2} s^{-1},
3. **Zone 3**: $\Gamma > 1.9$, F $< 10^{-11}$ ergs cm^{-2} s^{-1}.

These 3 zones on the graph can represent three different phases occurring in the jet emission mechanism.

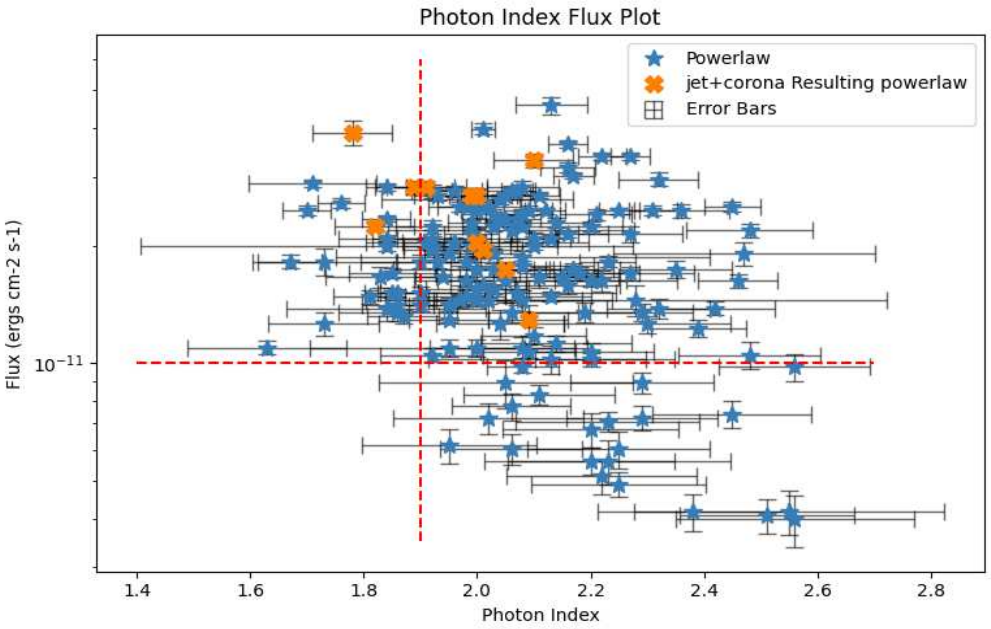

Figure 16: Areas of different Photon Index and Flux power. The area on the bottom left is the 'Zone of Avoidance'

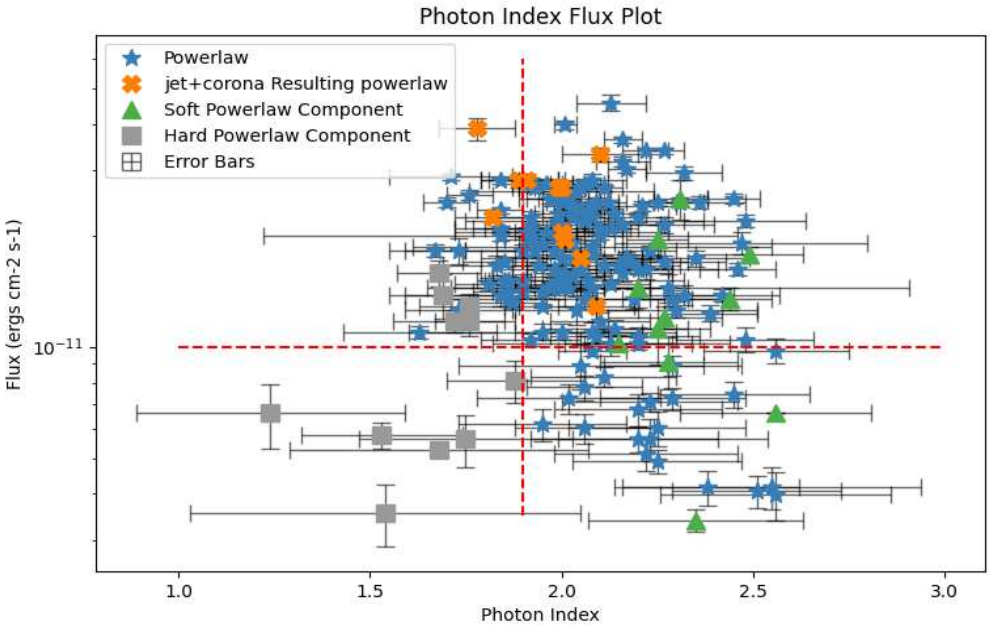

Figure 17: Areas of different Photon Index and Flux power. The two different components of the broken powerlaw are shown.

6.1.1.1 ZONE 1

In all the observations belonging to Zone 1, the Photon Index is found to be harder than the average values (about 2.1) of NLS1 galaxies spectra (Vaughan et al., 1999, Leighly, 1999b). Hence we suppose that this hardening is due to influence from a jet emission. When we posses available data, we will confirm this assumption with Fermi LAT results.

The single spectra of observations belonging to *zone* 1 were either:

- Flat spectrum well modeled by single **powerlaws**. We believe here the jet's emission dominates the whole spectrum from 0.3keV.
- Spectra modeled with **broken powerlaws**. Here through spectral fitting one can explicitly distinguish the two components contributing to the emission: the hard component representing the jet contribution and the soft component modeling the coronal emission. The energy break is usually in the range 1.2-3.0 keV.

This is consistent with results from previous researches in gamma-ray-emitting NLS1s. They are typically well fitted by a broken power-law model, exhibiting a break at approximately 2.0 keV. Below this break, the spectrum is attributed to disc and coronal emissions, a common feature of Seyfert galaxies. Conversely, the emission above the break is governed by jet-related processes, a characteristic feature of blazars.

I also summed all the spectra that were classified as *zone* 1 and I fitted the averaged spectrum with `XSPEC` obtaining as a best-fit model a broken powerlaw with energy break at about 2.49 keV, a soft component which is still describing a flatter spectrum $\Gamma_1 = 1.96 \pm 0.03$ and a harder component with $\Gamma_2 = 1.74 \pm 0.05$.

Later in this chapter I will compare this averaged spectrum with the ones of

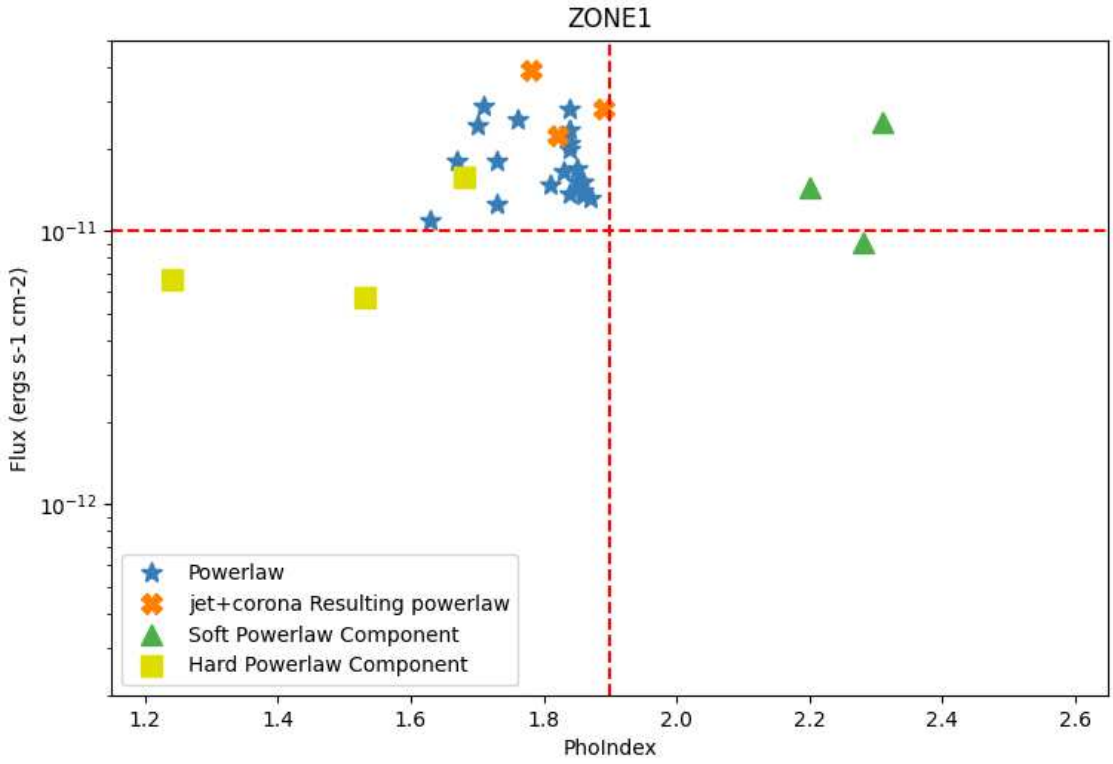

Figure 18: Photon Index flux graph of *zone* 1 observations

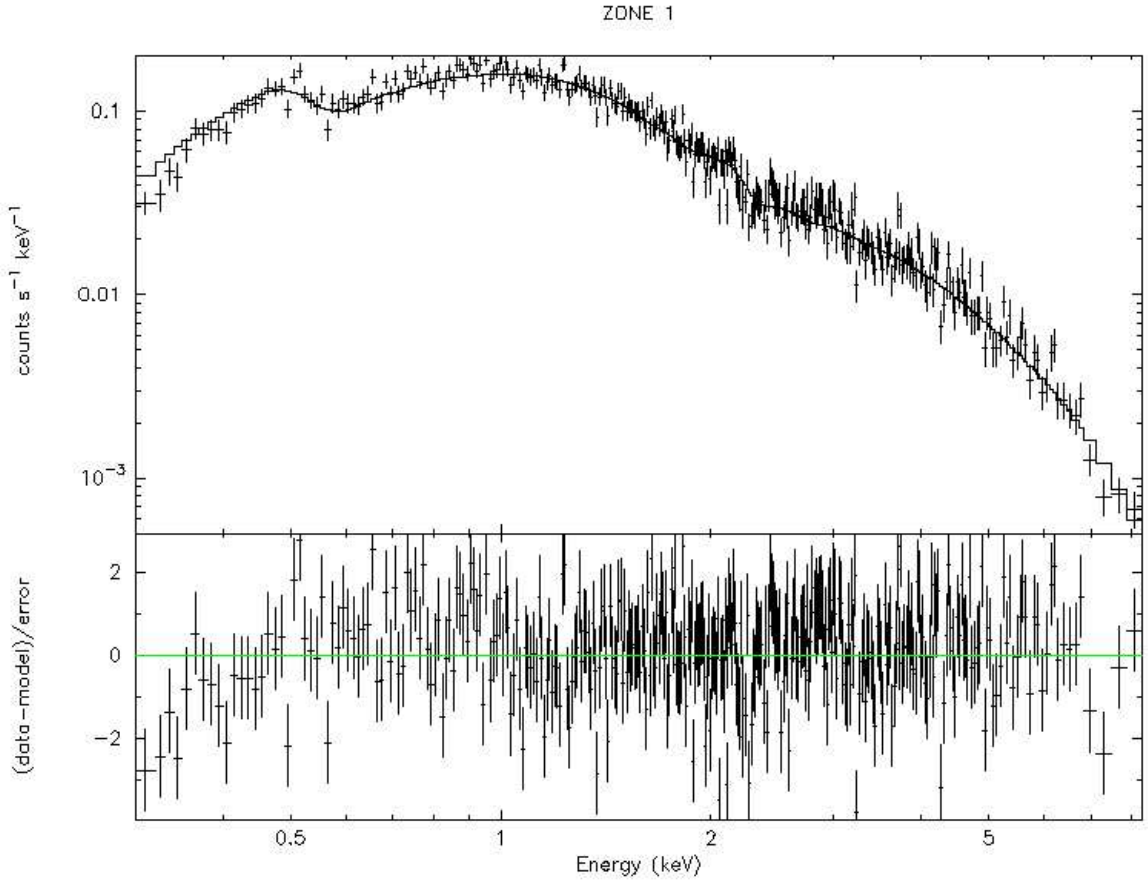

Figure 19: Count rates of *zone* 1 between 0.3-10.0 keV with residuals

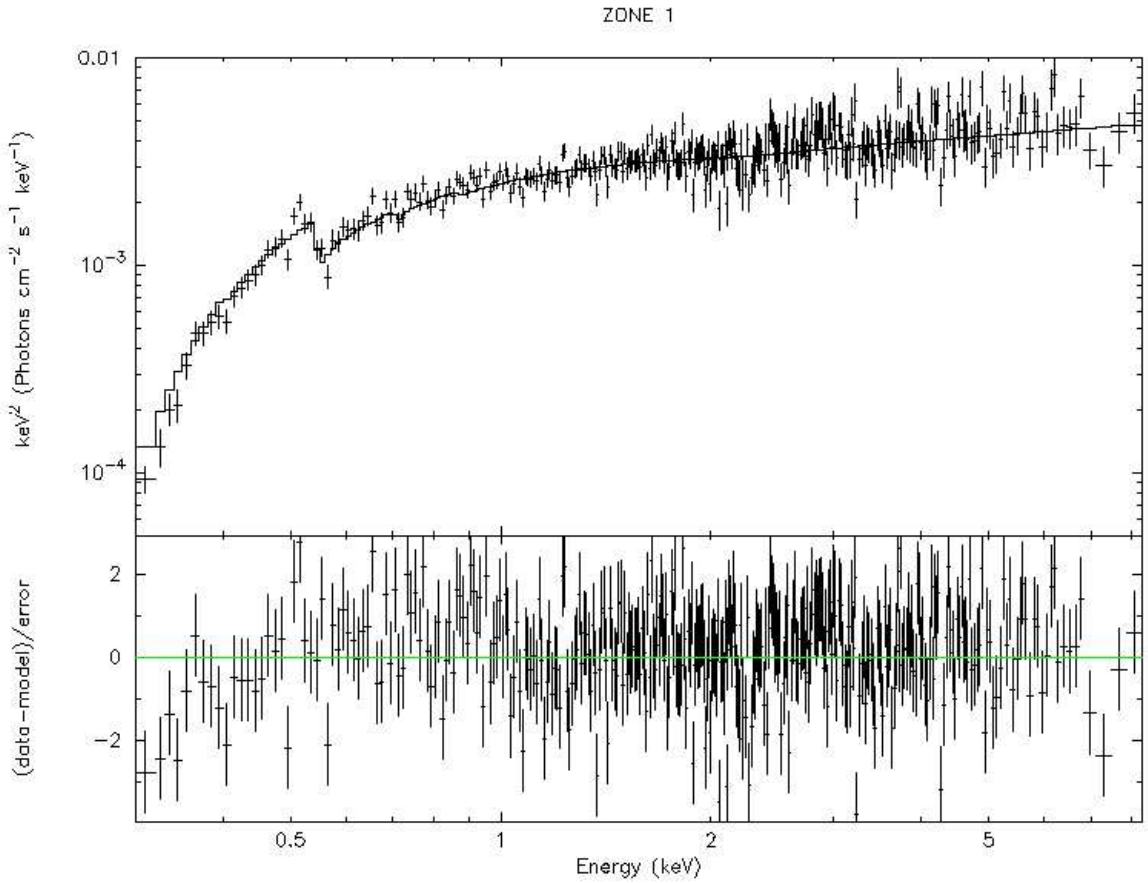

Figure 20: Plot with residuals of fitting model broken powerlaw *zone* 1

the other *zones*.

We now attempt to explain what happens in *zone* 2.

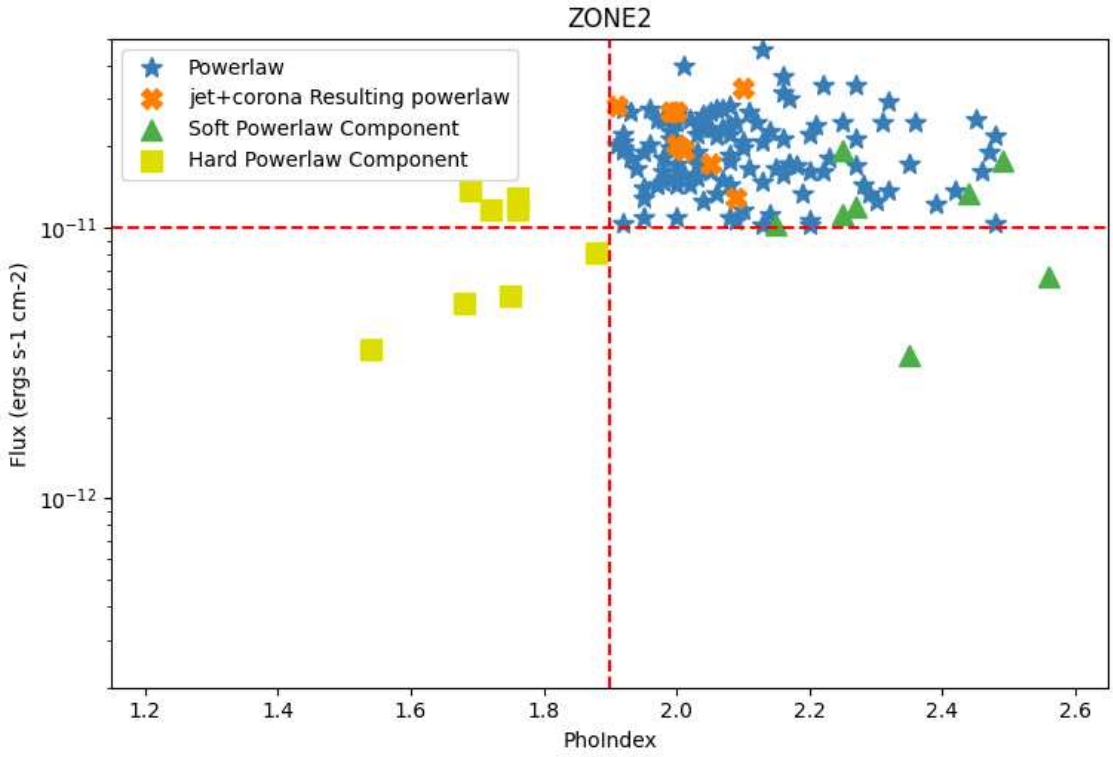

Figure 22: Photon Index flux graph of *zone* 2 observations

6.1.1.2 ZONE 2

Here single spectral data were either described by:

- High fluxes single **powerlaws** with Γ values ranging from 1.9 to 2.4. We justify this high flux emission at relatively low electron energies assuming it arises as a consequence of efficient electron cooling. The softer spectrum does not provide evidence of jet emission.
- **Broken powerlaw** with average $\Gamma > 1.9$. This feature can be explained if the jet's emission has occurred but it was not sufficiently powerful to dominate the spectrum.

In the graph, data points belonging to *zone* 2 are plotted, showing also the broken powerlaw components.

The best fit model for *zone* 2 average spectrum was composed of:

- **Blackbody**: modeling the soft excess below 1keV. The inner temperature was found to be kT=0.17 ± 0.02.
- **Powerlaw**: modeling the coronal emission, with $\Gamma = 1.94 \pm 0.03$.

The addition of `zbbody` enabled to reduce the χ^2 value from 642.94/472 to 562.53/470.

Both features of this average spectrum are interesting: the powerlaw index is still harder than the average photon index of NLS1 galaxies and this leads to the question whether it can be related to favourable conditions for the jet emission. Regarding the soft excess, it is a common feature among AGN, even though in this specific source was not prominent.

6.1.1.3 Soft Excess

This observed feature, predominantly shown in NLS1 galaxies, initially was hypothesized to be a high-energy tail of the optical-UV accretion disk emission.

However, this theory has been rejected by observational data as this excess is not correlated with SMBH mass or accretion rate. The observed temperature exceeds what is expected for a standard accretion disk. Various hypotheses have been proposed to explain the soft excess: a ionized reflection within the inner regions of the accretion disk, leading to relativistic blurring of X-ray lines (Ross and Fabian, 2005), a relativistically smeared absorption at higher energies, where high-velocity absorbing clouds obscure atomic spectral features, resulting in a seemingly soft excess (Bambi, 2023) and finally the existence of two Comptonizing regions within the AGN, one hotter region responsible for high-energy emission and another colder region producing the soft X-rays (Laor et al., 1997).

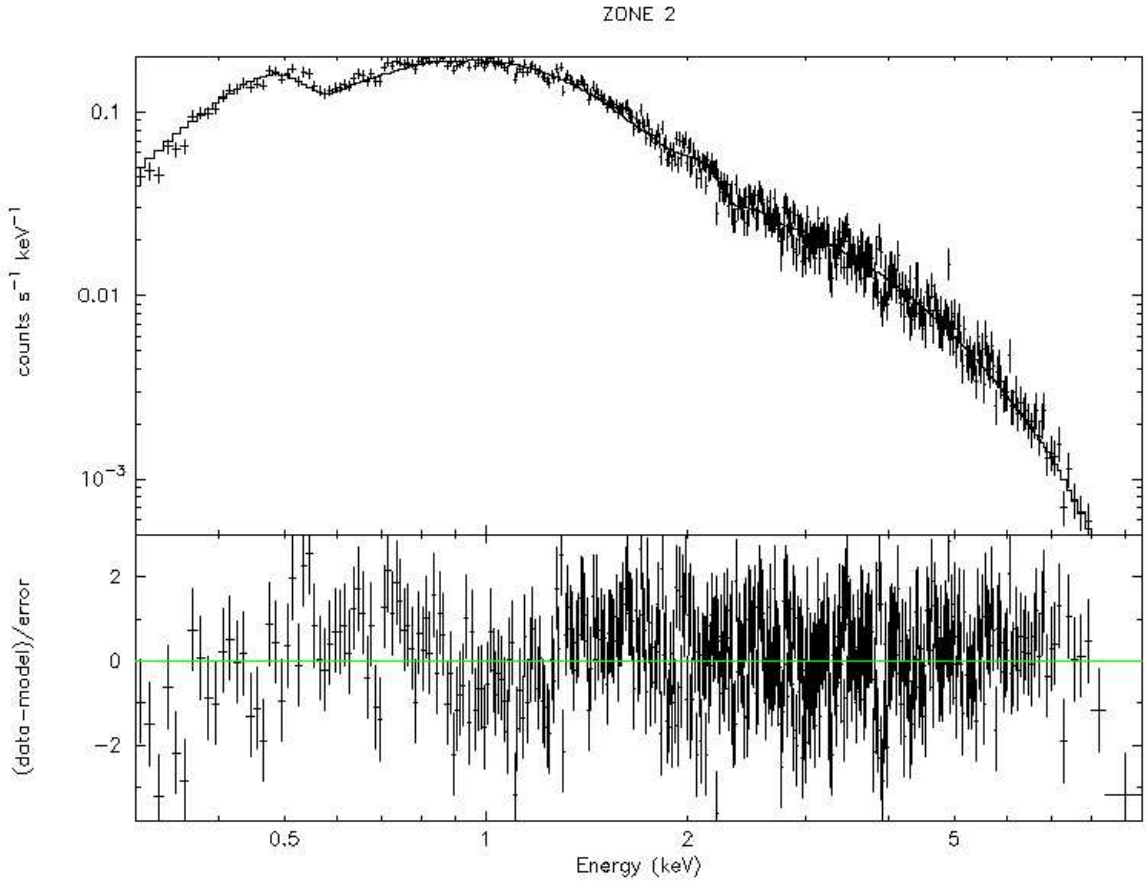

Figure 23: Count Rate of ZONE2 between 0.3-10.0 keV

Although there are apparent differences in the physical mechanisms of these models, they can explain the X-ray spectrum with comparative goodness of fit. This makes the physical origin of soft X-ray excess subject to long-standing controversy. To break the degeneracy of these models, some works have used broadband energy spectrum analysis or temporal analysis to study some particular sources. The results show that in different sources, the origin of the soft excess is different and the excess even has hybrid characteristics, which implies that its origin is diverse from source to source.

I also created a contour plot to see if parameters kT and Γ were correlated:

I noticed also from the previous Γ-Flux graphs that several observations over time appear to switch from *zone*1 to *zone* 2.

The explanation I propose for these observed features, is that the emission from the jet may originate from kinetic processes involving coronal electrons that are accelerated, triggering the emission. Furthermore, the jet could also exert a influence on the coronal environment making it more suitable for a following jet generation.

6.1.1.4 Around the jet emission

I decided to study more in detail the evolution of spectral parameters by selecting the intervals encompassing a supposed jet emission modeled with a `brokenpowerlaw`.

Comparing the parameters inferred with `XSPEC`, one indeed notices that there is either an increased flux and/or a flattening of the spectrum, anticipating and/or following an event well modeled by a broken powerlaw.

Here below I list some selected time intervals with the fitting models and inferred parameters. The full table is attached in the Appendix.

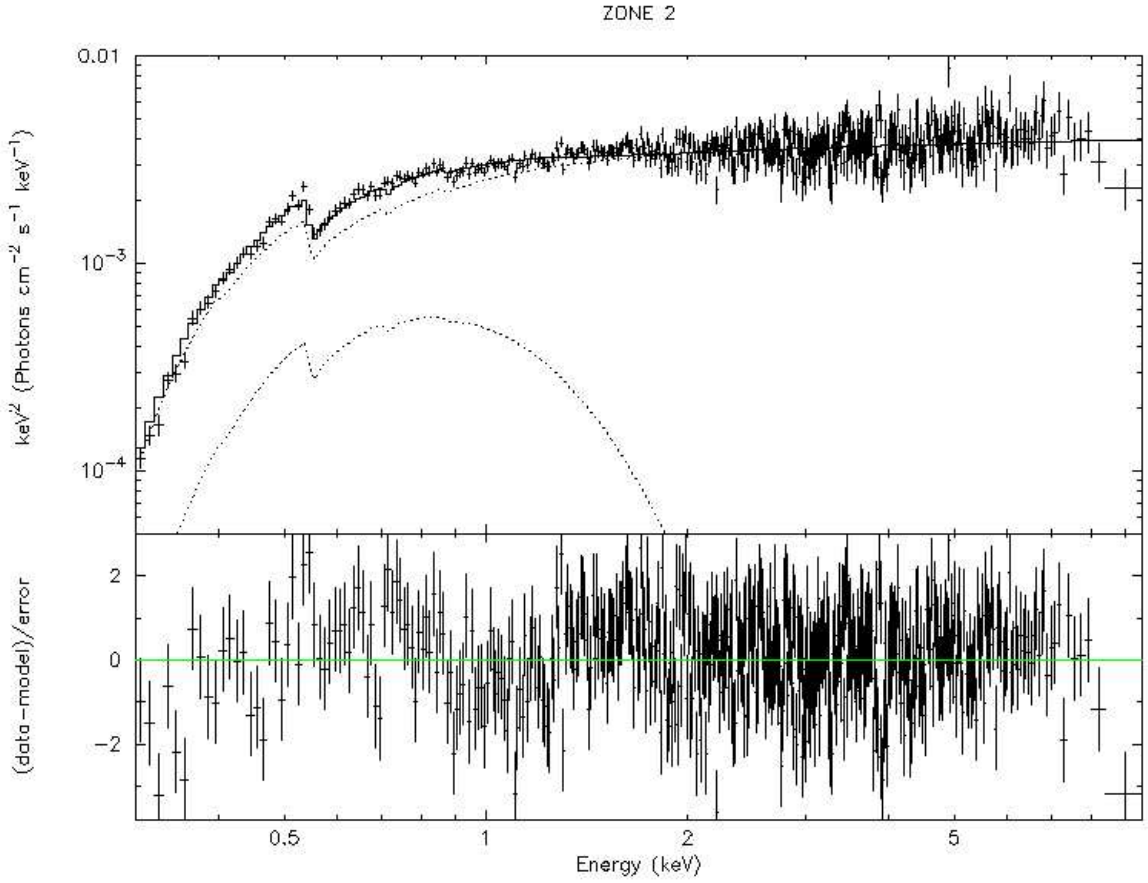

Figure 24: Plot E^2counts with residuals. Model: `tbabs(blackbody + zpowerlaw)` *zone*2

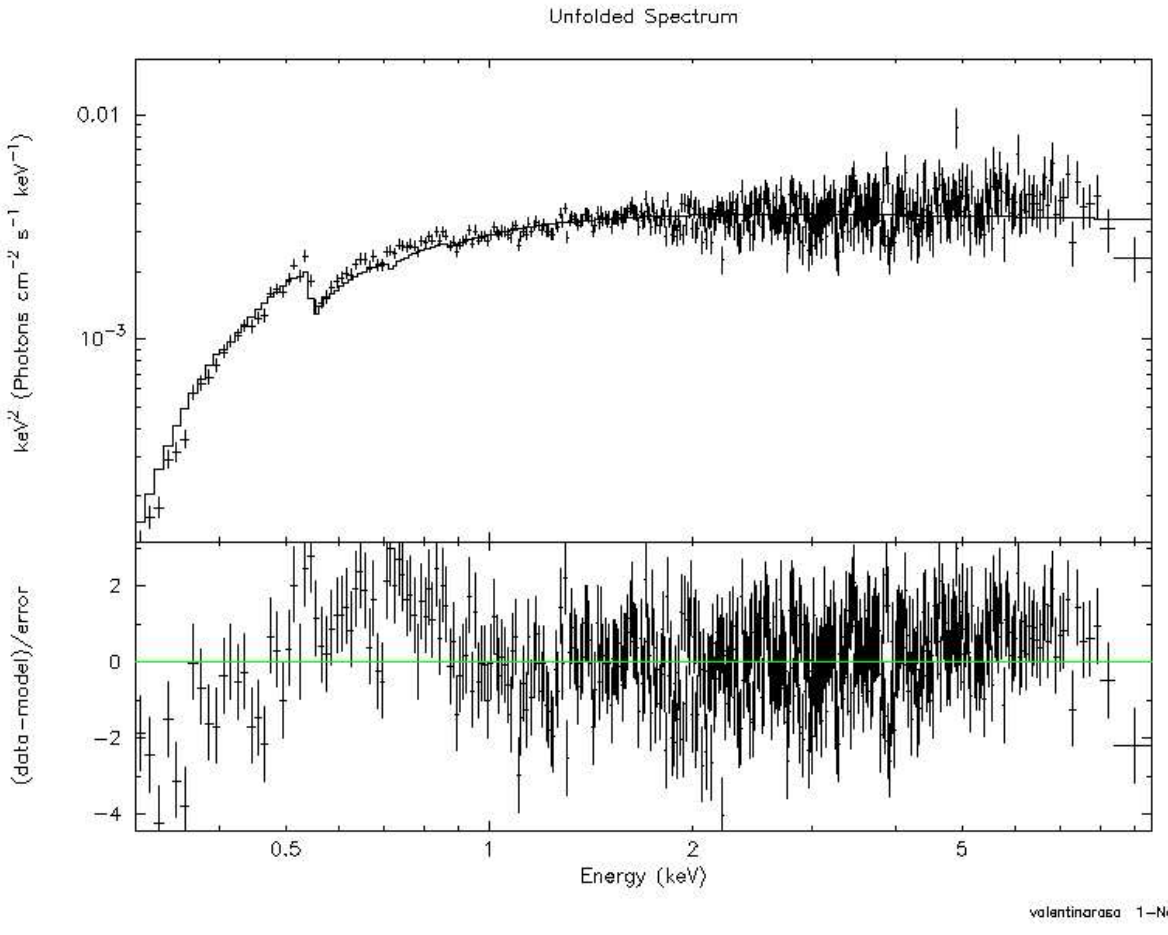

Figure 25: Plot E^2counts with residuals. Model: `tbabs(zpowerlaw)` *zone*2

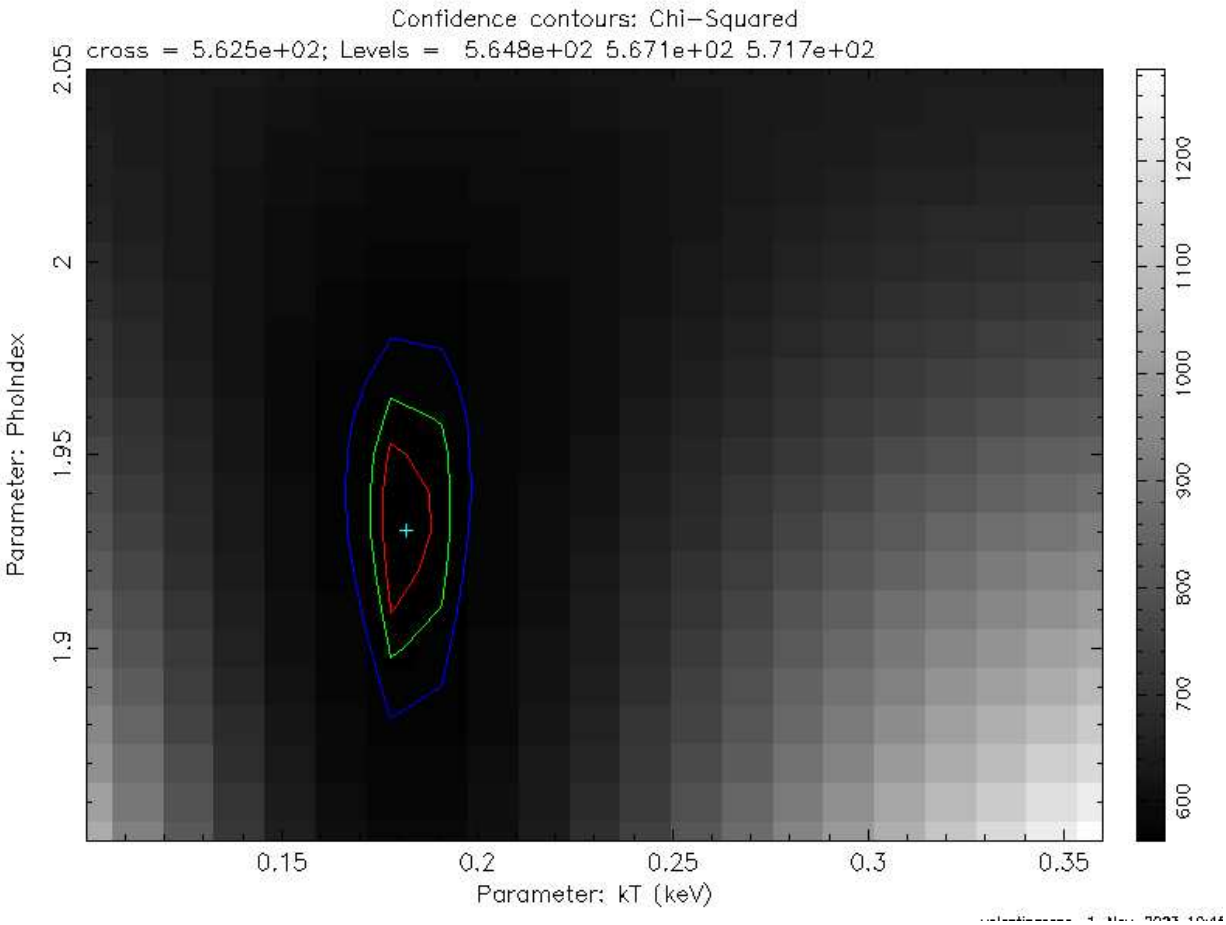

Figure 27: Contour plot, xaxis=kT values, yaxis= Γ values. The two parameters do not show significant correlation

Model	Time (MJD)	Γ_1	$Flux_1$ (10^{-11} ergs $cm^{-2}\,s^{-1}$)	E_{break} (keV)	Γ_2	$Flux_2$ (10^{-11} ergs $cm^{-2}\,s^{-1}$)	χ^2
`pow`	55043.35	1.84 ± 0.05	2.34 ± 0.11				59.47/50
`bkn`	55045.03	2.20 ± 0.10	1.45 ± 0.09	2.39 ± 0.44	1.53 ± 0.19	0.58 ± 0.07	38.42/38
`pow`	55048.03	1.95 ± 0.05	1.66 ± 0.08				29.13/40
`pow`	55051.52	2.10 ± 0.05	1.82 ± 0.10				33.14/36

Table 1: Observations of a jet emission from MJD 55043.35 to 55051.52 (2009-07-31 08:24:00 - 2009-08-08 12:28:48)

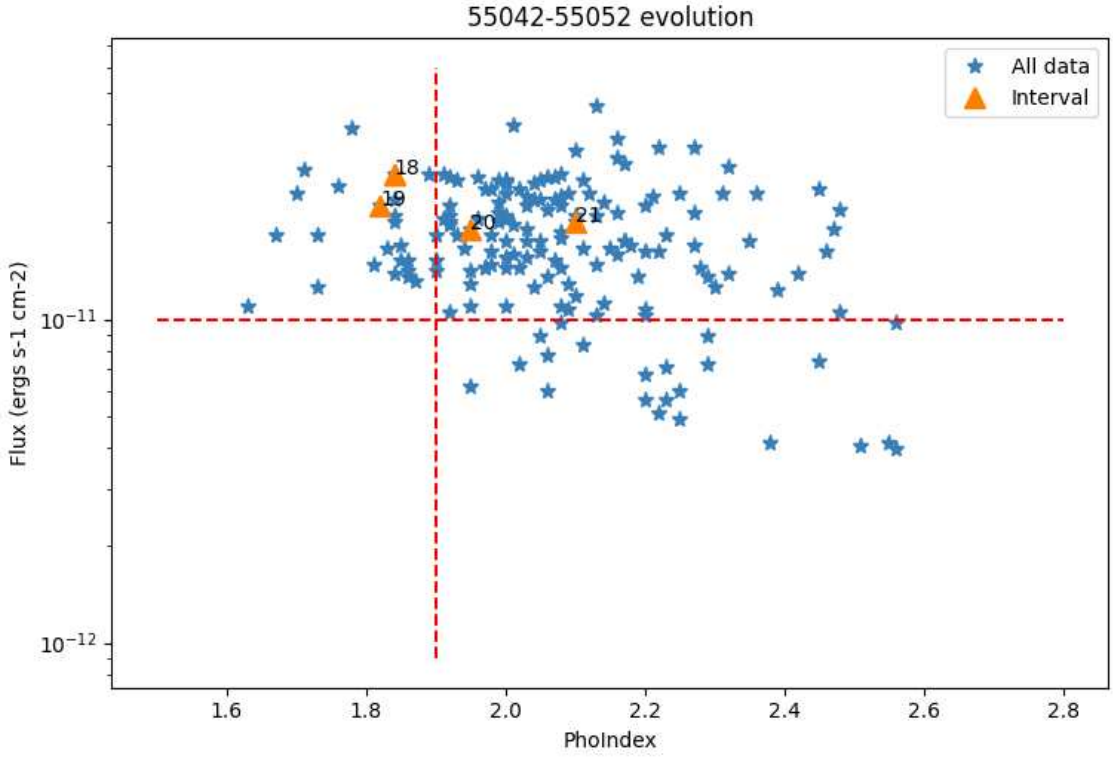

Figure 28: Evolution of Photon Index & Flux between MJDs 55042 and 55052

Model	Time (MJD)	Γ_1	$Flux_1$ (10^{-11} ergs $cm^{-2}\,s^{-1}$)	E_{break} (keV)	Γ_2	$Flux_2$ (10^{-11} ergs $cm^{-2}\,s^{-1}$)	χ^2
bkn	55525.79	2.31 ± 0.07	2.31 ± 0.10	2.74 ± 0.21	1.24 ± 0.31	0.68 ± 0.08	50.42/50
pow	55526.26	2.11 ± 0.04	2.57 ± 0.08				58.25/58
bkn	55527.74	2.25 ± 0.14	1.13 ± 0.09	1.46 ± 0.17	1.68 ± 0.14	1.40 ± 0.09	44.06/36
bkn	55528.13	2.25 ± 0.13	1.75 ± 0.08	2.47 ± 0.61	1.75 ± 0.22	0.57 ± 0.05	39.17/33
pow	55529.14	2.13 ± 0.05	2.12 ± 0.11				48.72/43
Model	Time (MJD)	Γ_1	$Flux_1$ (10^{-11} ergs $cm^{-2}\,s^{-1}$)	E_{break} (keV)	Γ_2	$Flux_2$ (10^{-11} ergs $cm^{-2}\,s^{-1}$)	χ^2
pow	56491.68	1.99 ± 0.06	2.29 ± 0.08				27.92/35
bkn	56492.10	2.28 ± 0.18	0.92 ± 0.06	1.37 ± 0.16	1.68 ± 0.11	1.58 ± 0.07	34.57/34
pow	56492.68	1.84 ± 0.06	2.27 ± 0.07				51.44/45

Table 2: Observations of jets emissions between MJDs 55525-55530 (2010-11-25, 2010-11-30) and 56491-56493 (2013-07-18, 2010-11-30)

In this case we were able to obtain spectra from observations separated only by two or three days. We can deduce from the fitting models that on MJD 55045.03, the jet component has emerged and we were able to distinguish it from the coronal component. During MJD 55043.35 the hardening of the spectrum can be explained by either the influence of a previous jet emission on the coronal environment or an increase of the electron velocities as a starting condition for a second jet emission.

After the jet emission it looks that the environment slowly cools down but keeping the flux values high.

The observations between MJDs 55525 and 55529, show evidence of a jet emission that dominates the spectrum during MJD 55527.74. Since both the hard and soft components of the following supposed emission are consistent within confidence intervals, I was driven to the assumption that either we are observing very fast and alternate self-similar jet emissions, or we are seeing the same

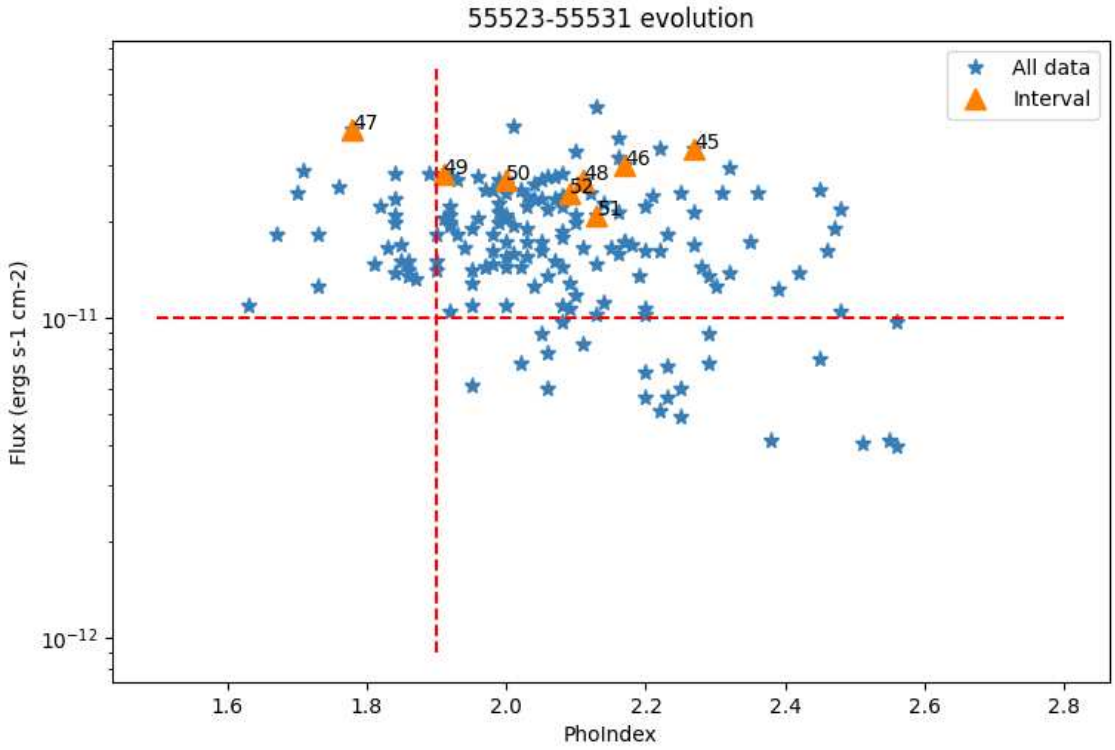

Figure 29: Evolution of Photon Index & Flux between MJDs 55523 and 55531

emission influencing the disk-corona environment over a longer time interval.

In this case we confirm the presence of the jet emission with a good fit of broken powerlaw models for our data. Looking at the observations before and after the emissions we see that slopes of powerlaw models lie in the soft range, but significantly high flux values are measured.

Between MJDs 56491 and 56493 a steeper slope of the powerlaw remains after the jet emission yelding $\Gamma = 1.84$ with still above average flux values.

We conclude that the jet and the corona are tightly linked together as the jet ejection is generated through the acceleration of hot electrons in the corona. How the jet interacts with the environment during the emission is still a mystery, as in some cases a hardening of the spectrum is observed, while in other observations only high flux values are measured with softer spectra.

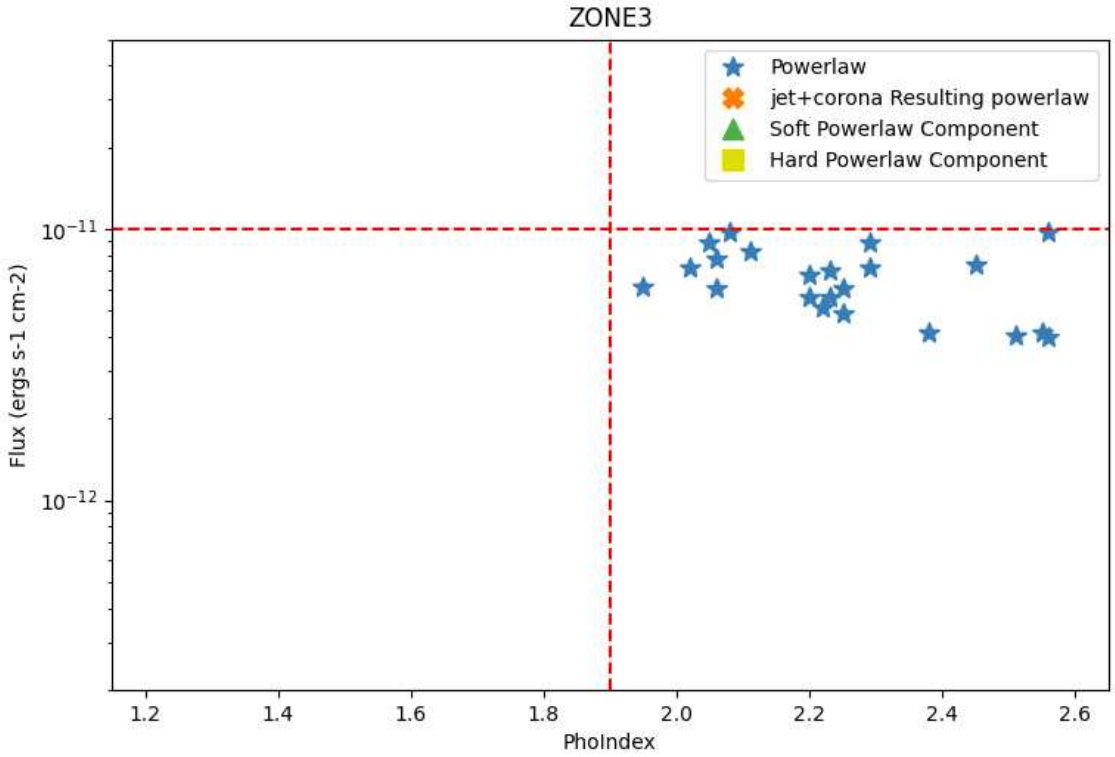

Figure 30: Photon Index flux graph of *zone* 3 observations

6.1.1.5 ZONE 3

Here data are described by low fluxes single powerlaws with photon index Γ_3 that approaches the typical values found in non jetted Narrow Line Seyfert 1 Galaxies.

Since flux values in the 0.3-10.0 band are lower and spectra are softer, one suggested hypothesis states that no jet emission is occurring during these observations.

In the graph, data points belonging to *zone* 3 are plotted, showing also the broken powerlaw components.

As a model for *zone* 3 average spectrum, a powerlaw with $\Gamma = 2.23 \pm 0.05$ was the best fit for the data. Indeed a softer spectrum with a significantly lower

Mod	*zone*	Γ_1	Flux_1 (10^{-11} ergs $\text{cm}^{-2}\,s^{-1}$)	E_{break} (keV)	Γ_2	Flux_2 (10^{-11} ergs $\text{cm}^{-2}\,s^{-1}$)	χ^2
`bkn`	1	1.96 ± 0.03	2.31 ± 0.10	2.47 ± 0.11	1.74 ± 0.06	0.68 ± 0.08	466.54/350
`pow`	2	2.07 ± 0.03	1.59 ± 0.04				642.94/472
`pow`	3	2.23 ± 0.05	0.69 ± 0.07				130.01/124

Table 3: Parameters inferred with XSPEC spectral models

	H (10^{-11} ergs $\text{cm}^{-2}\,s^{-1}$)	S (10^{-11} ergs $\text{cm}^{-2}\,s^{-1}$)	R_H
zone 1	1.06	0.58	0.29
zone 2	0.96	0.68	0.17
zone 3	0.29	0.31	-0.04

Table 4: Hardness ratios of the 3 averaged spectra

$F_\nu\nu$ is observed compared to the previous two.

Here is what I obtained:

As an additional method, useful to charachterize these differences between the three phases in the X-ray band, I have calculated the hardness ratio R_H, defined as:

$$R_H = \frac{H - S}{H + S} \tag{6.1}$$

Here H is the flux measured between 2.0 and 10.0 keV, while S is the flux value measured in the 0.3 and 2.0 keV energy band.

I also plotted the evolution in time of the hardness ratio, showing that the values are decreasing in more recent observations.

To interpret these ratios, I will first summarize some key concepts regarding spectral hardening in BHXRBs. In these sources, spectral hardening is observed

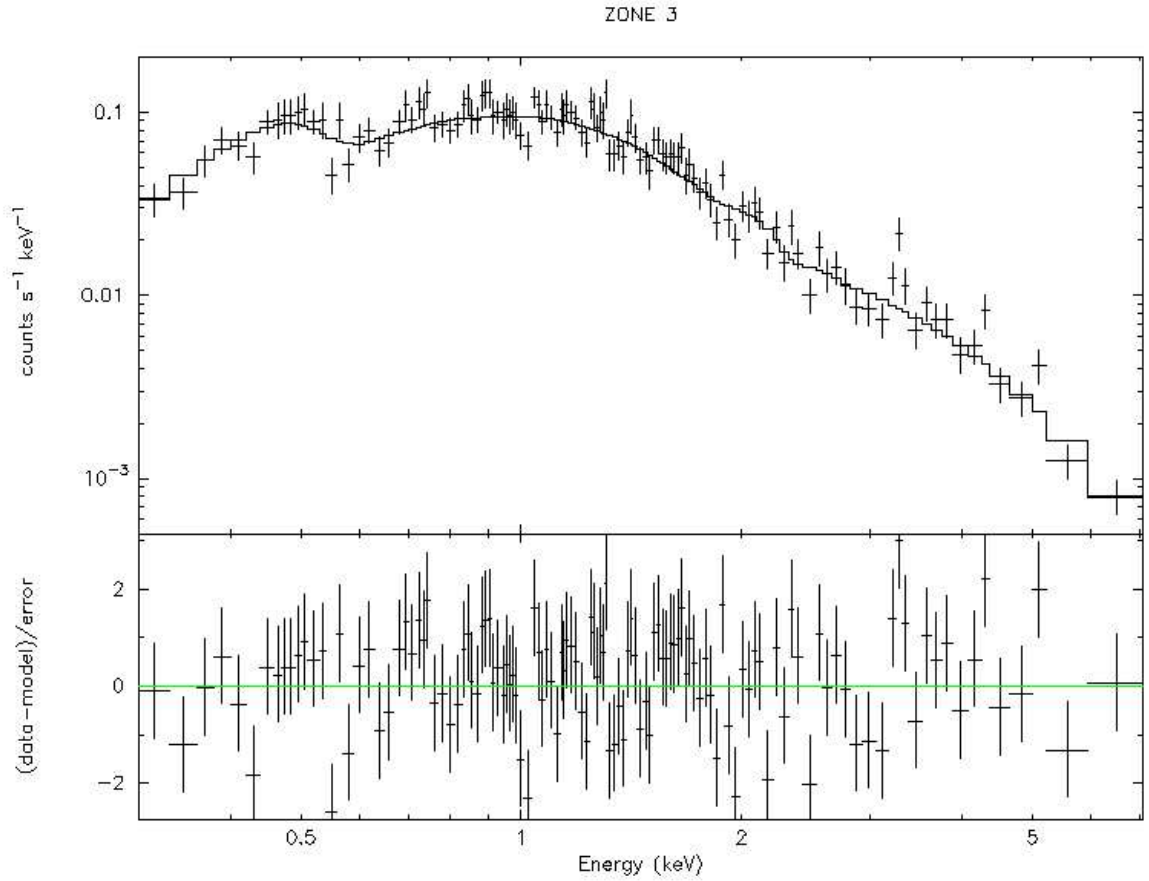

Figure 31: count rate of *zone* 3 with residuals, between 0.3-10.0 keV

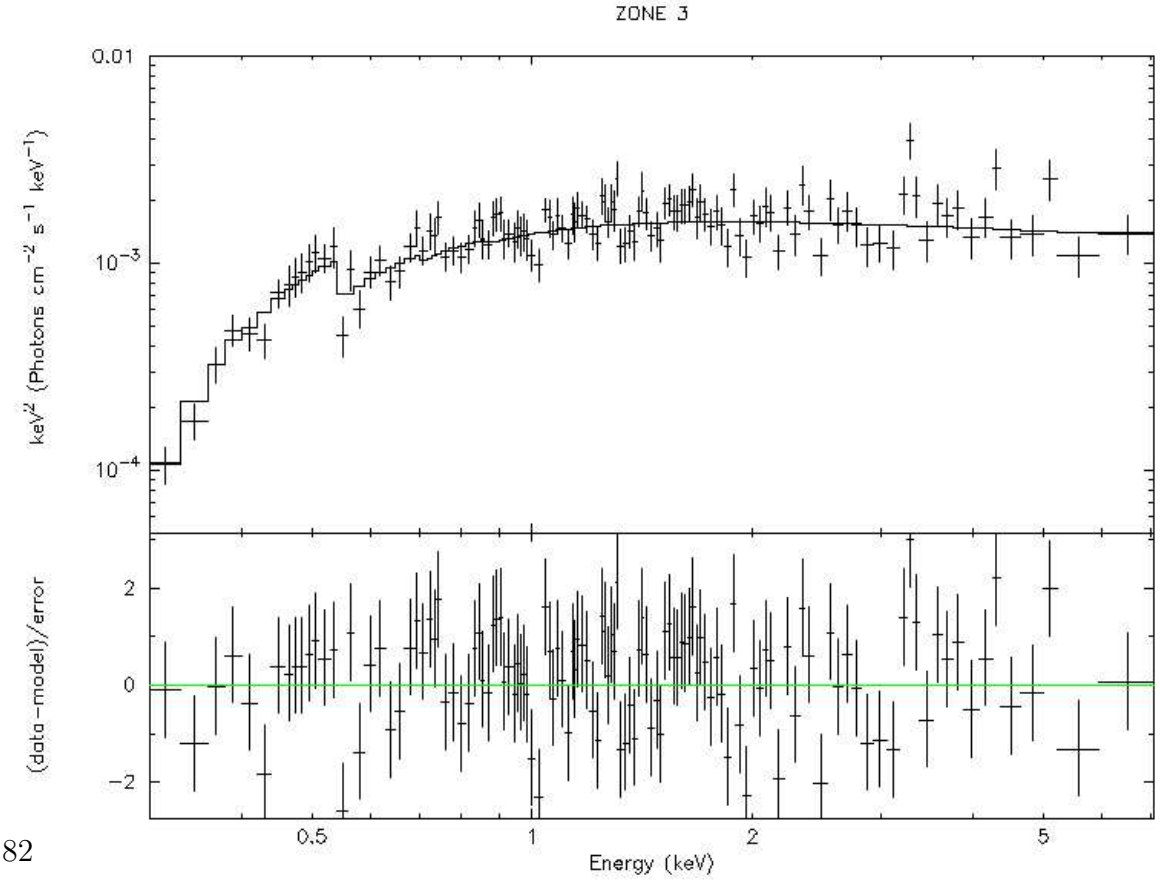

Figure 32: Plot E^2counts with residuals *zone* 3

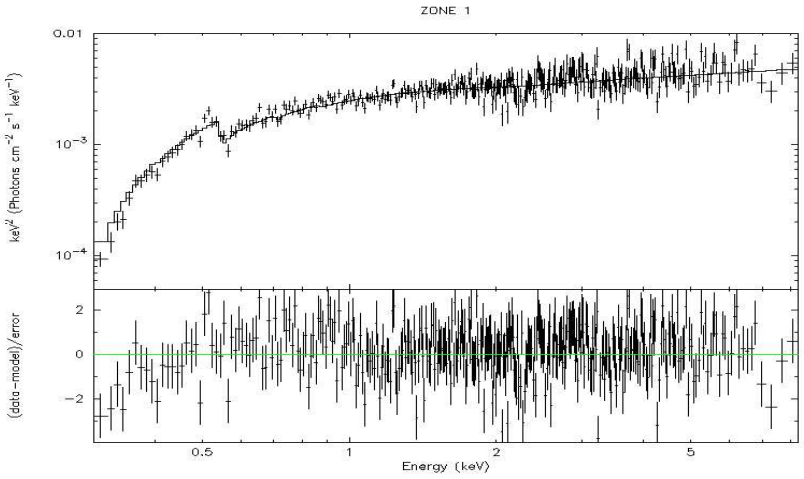

Figure 34: X-ray average spectrum ZONE 1

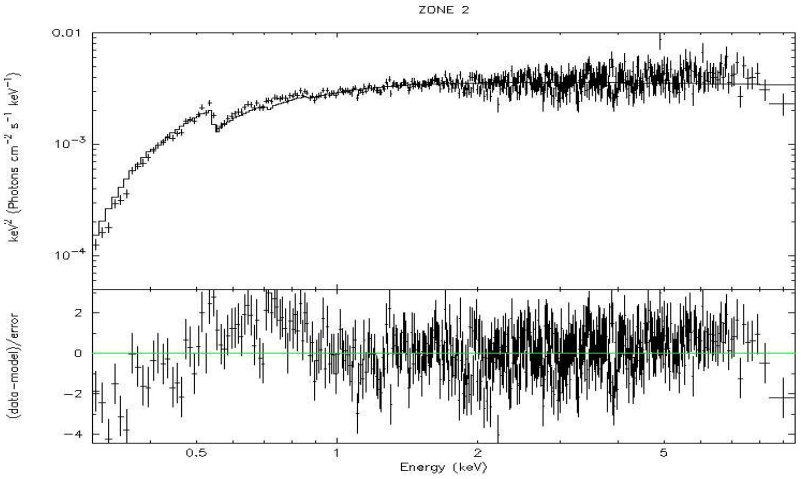

Figure 35: X-ray average spectrum ZONE 2

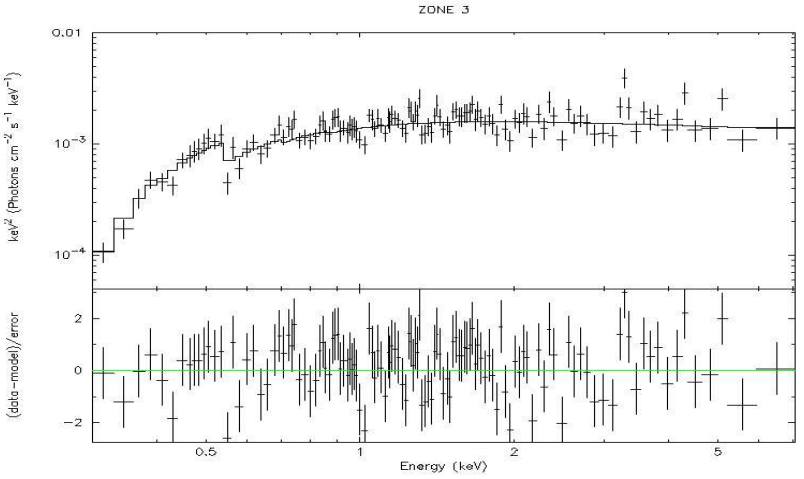

Figure 36: X-ray average spectrum ZONE 3

Figure 37: Comparing spectra of the three *zones*.

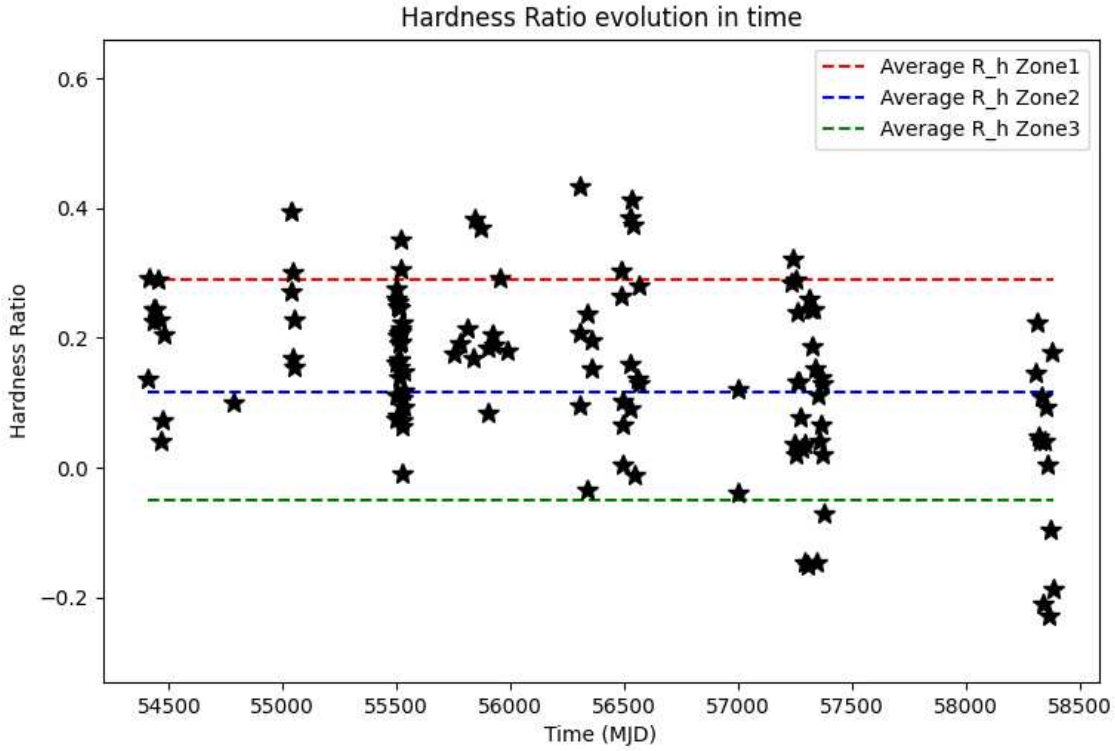

Figure 38: Hardness Ratio evolution over time. The dashed lines are referring to the average values of R_H in the three zones.

with a steep rise in intensity associated with a jet, followed by a softening of the spectrum. Then the jet dissipates and intensity drops to the quiescent state.

The Hardness Ratio is used to classify these states quantitatively and in a model independent manner.

Searches for R_H states in AGN analogous to BHXRB have been carried out for 20 years. We note AGN are not expected to exhibit a state change despite their high variability, since unlike BHXRBs the time-scale in AGN for such a change is extremely long, but we will dive deeper into this topic in the following paragraphs.

If we consider $R_H = 0$ as the separator between "harder when brighter behaviour", usually associated to jetted AGN and "softer when brighter" behaviour, typical of Seyfert Galaxies, we notice that observations from *zone* 1 and 2 belong to the first cathegory, while phase 3 more likely belongs to the latter.

Following the qualitative description of the physical processes occurring in R_H variability, provided from Peretz and Behar (2018), we consider that if the slope of R_H is positive, so if Hardness Ratio tends to increase during later observations, Compton cooling dominates its beginning and transitions into coronae dominated by energy injection.

The study also suggests that one explanation of different R_H values and slopes among Seyfert Galaxies, could be linked to geometry: the "softer-when-brighter" objects are expected to have coronae positioned predominantly above and around the black hole keeping a minimum distance from it. When the R_H increases, indicating "harder-when-brighter" conditions, it could be a consequence of the corona that drops towards the black hole.

Variations in flux are primarily attributed to the energetic processes happening within the corona and its close surroundings.

As we know that the corona of NLS1s is highly dynamic and can undergo under significant changes in a short time, we want to understand what mechanism could have occurred switching from *zone* 2 to *zone* 3.

6.1.2 X-ray parameters evolution in time

In the light curve plot, one can observe two major changes towards recent observations:

- An overall decrease of the flux values.
- Ceased broken powerlaw modeled data.

If we also plot the photon index evolution in time, we notice that there is a slight increase in its values.

Finally, dividing the observations in three time intervals:

1. $\mathbf{I}_1$: 54000-56000 MJDs (2006-09-22,2012-03-14), represented in the graph as orange stars.
2. $\mathbf{I}_2$: 56000-57500 MJDs (2012-03-14,2016-04-22), represented in the graph as green squares.
3. $\mathbf{I}_3$: 57500-60000 MJDs (2016-04-22,2023-02-25), represented in the graph as purple triangles.

We can notice some analogies between the 3 time interval classification and the 3 *zones*: data belonging to *zone* 3, were entirely obtained during the third period between 57500-6000 MJDs suggesting that a change of phase has occurred in the last years.

The observed alterations are characterized by a reduction in flux levels and a discernible softening of the spectral slopes. Furthermore, the additional evidence provided by the calculated hardness ratio (R_{H_3}) underscores this evolving scenario, as it switches to a negative value, together with the observed spectral transformations.

For a more comprehensive and detailed elucidation of the temporal dynamics at

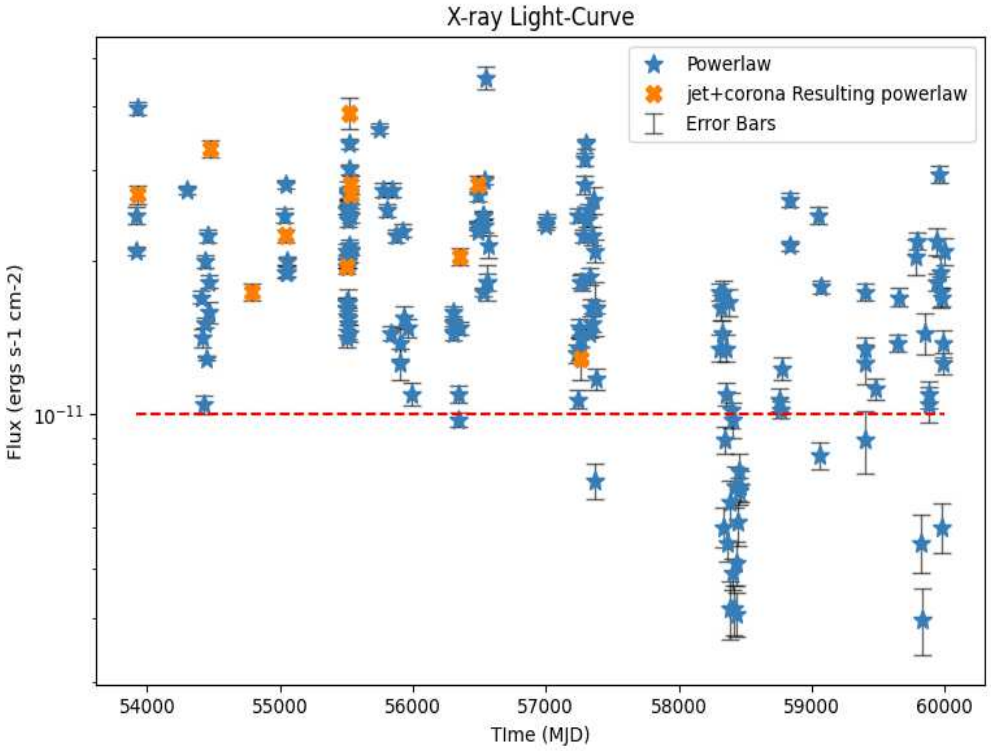

Figure 39: X-ray Lightcurve

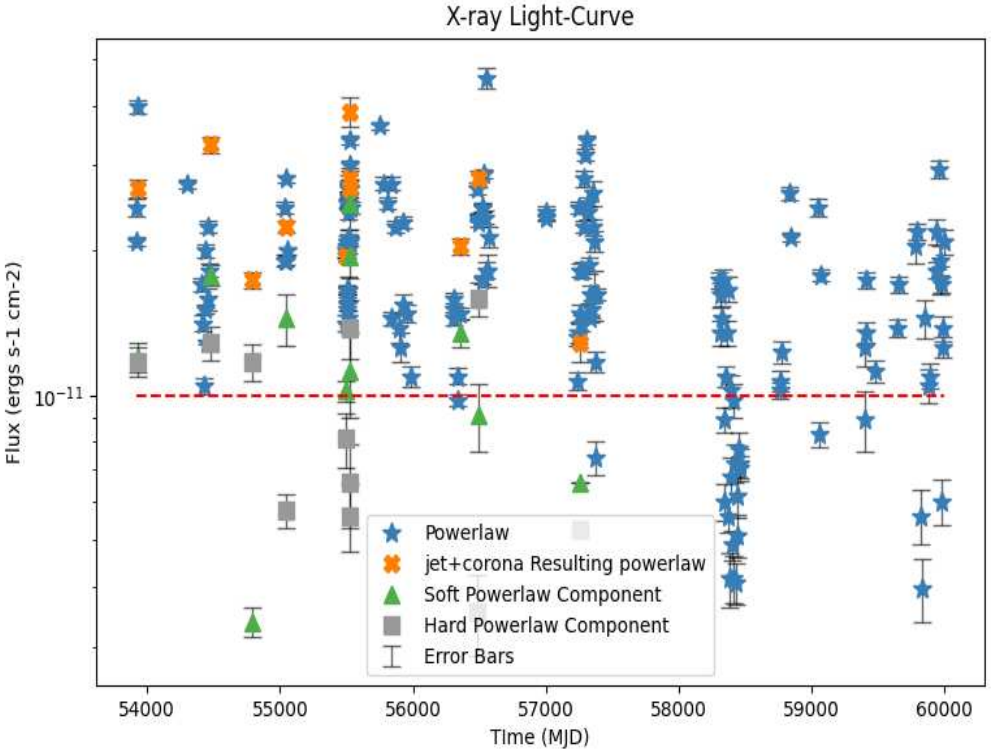

Figure 40: X-ray Lightcurve with error bars

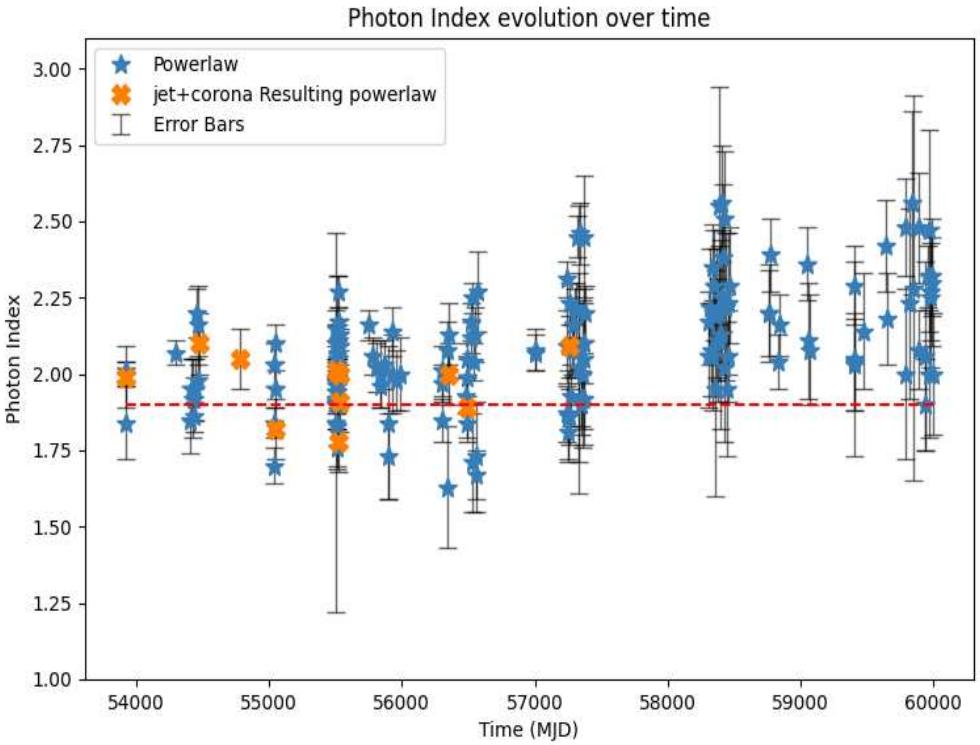

Figure 41: Photon index evolution over time

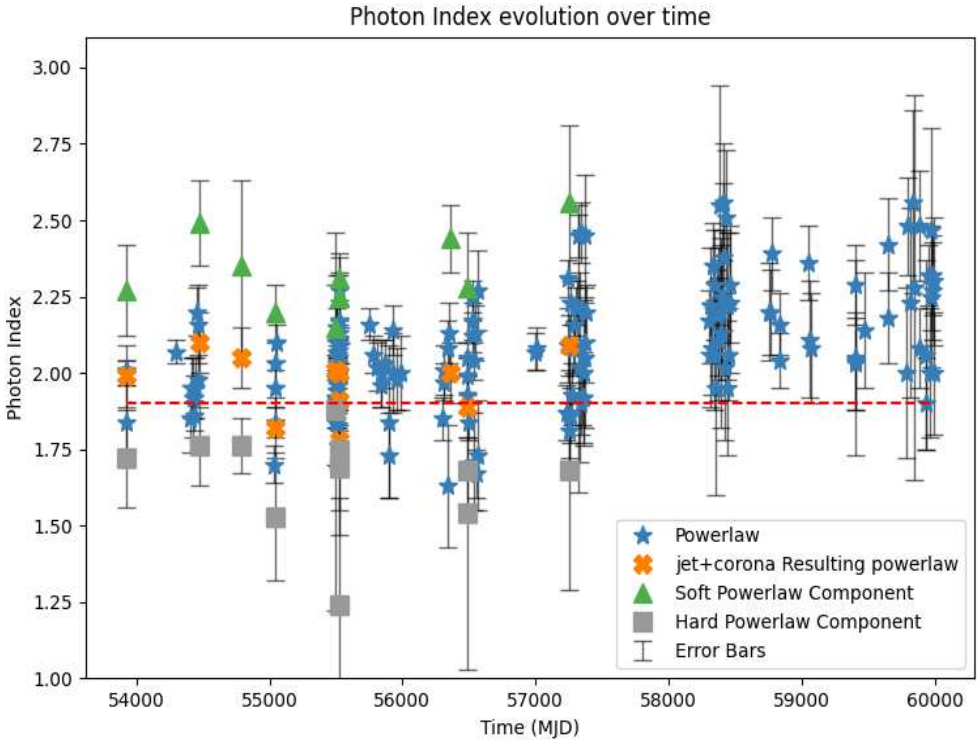

Figure 42: Photon index evolution over time with broken powerlaw components

play, the dataset is further dissected into six distinct time intervals. By plotting these intervals onto the photon index-flux graph, we can trace the evolution of critical parameters, providing a finer perspective on the intricate interplay of these processes.

Power law originating from the corona could be changing in intensity or shape for a number of reasons. For example, a cooling of the corona, or changes in the magnetic field, or ejection of the corona from the system. These would constitute intrinsic changes in the luminosity or shape of the power law due to physical changes in the corona.

I also plotted the values without the two components of the broken powerlaw.

The examination of these plots reveals distinct patterns within different temporal intervals. Notably, the first four intervals display a dynamic alternation between *zone*s 1 and 2, with *zone* 2 predominating during interval I4. In the subsequent intervals, I5 and I6, the observed values transition between *zone* 2 and 3. It is important to note that no data modeled with a broken powerlaw configuration are present during these later intervals. These distinctive features give rise to several pertinent considerations:

- The intermittent transitions between *zone*s 1 and 2 suggest that specific environmental conditions may become conducive to jet emission, likely influenced by the state of the coronal and potentially disk components. The alternate emergence of jets during these phases underlines the role of these conditions in regulating jet activity.
- During these intervals, it appears that the environmental factors do not favor the initiation of jet emission, showing features of non-jetted NLS1 galaxies. We suggest that the apparent absence of jets during such periods may be attributed to multiple interconnected reasons.

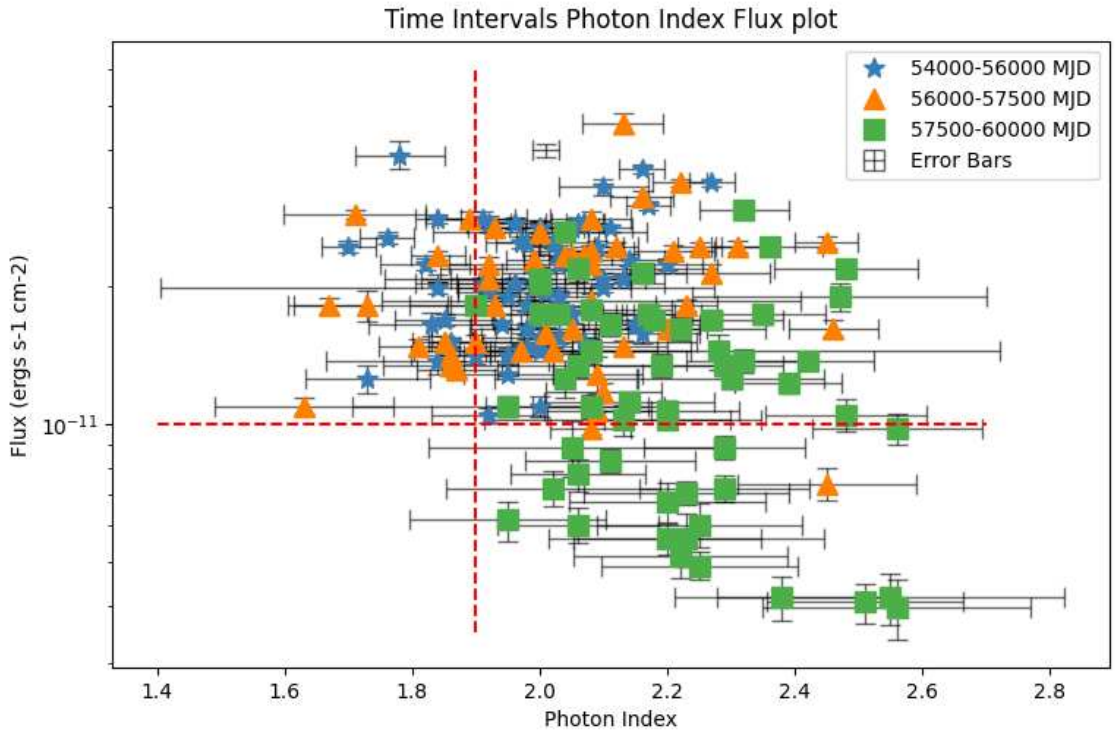

Figure 43: Photon index flux plot in 3 time intervals: 54000-56000 as orange stars, 56000-57500 as green squares, 57500-6000 as purple triangles.

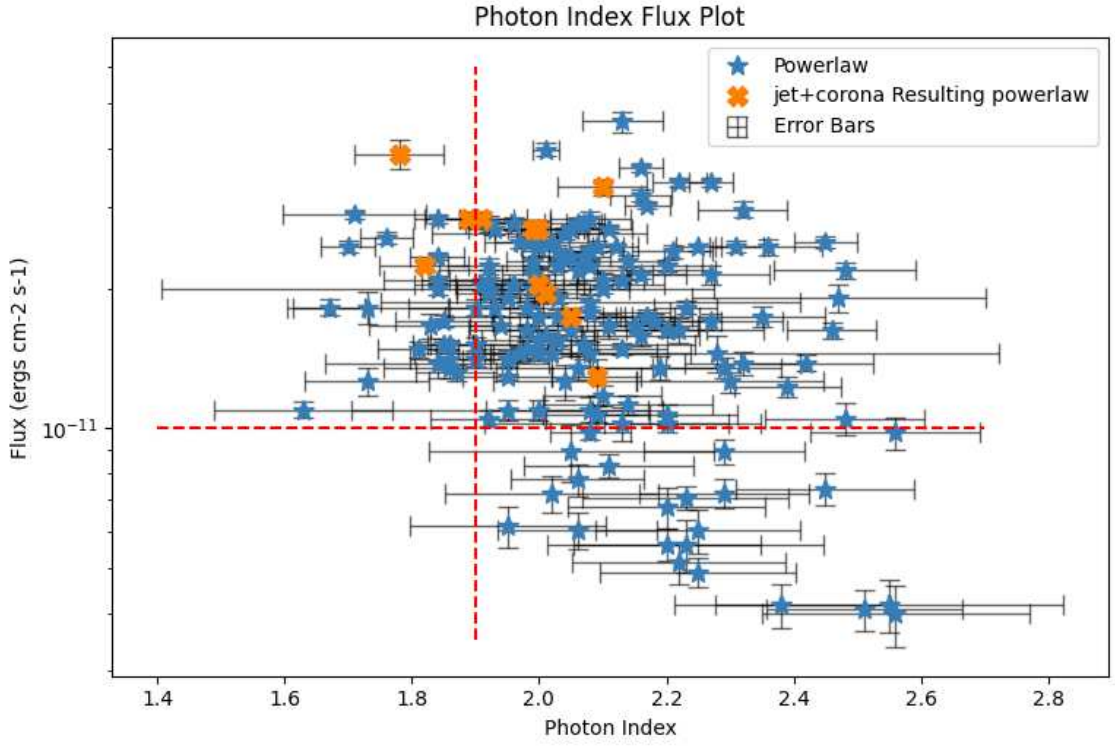

Figure 44: Areas of different Photon Index and Flux power. The area on the bottom left is the 'Zone of Avoidance'

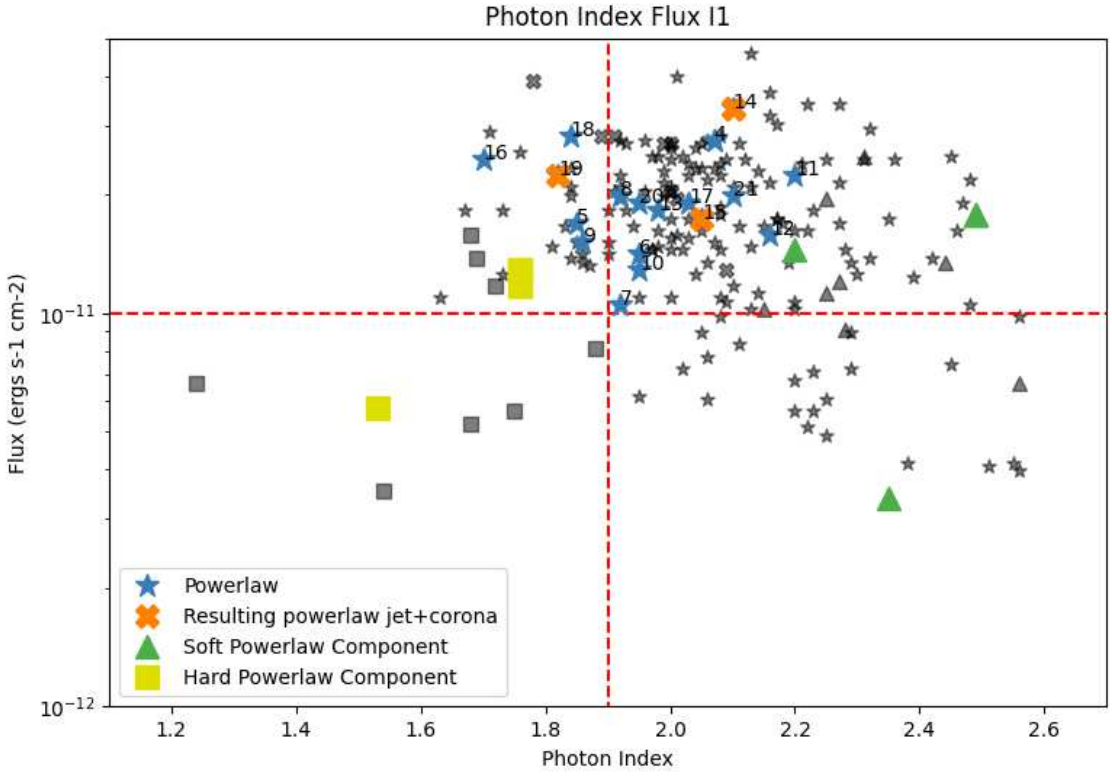

Figure 45: Photon index flux plot of interval I1=54000-55200 (2006-09-22, 2010-01-04)

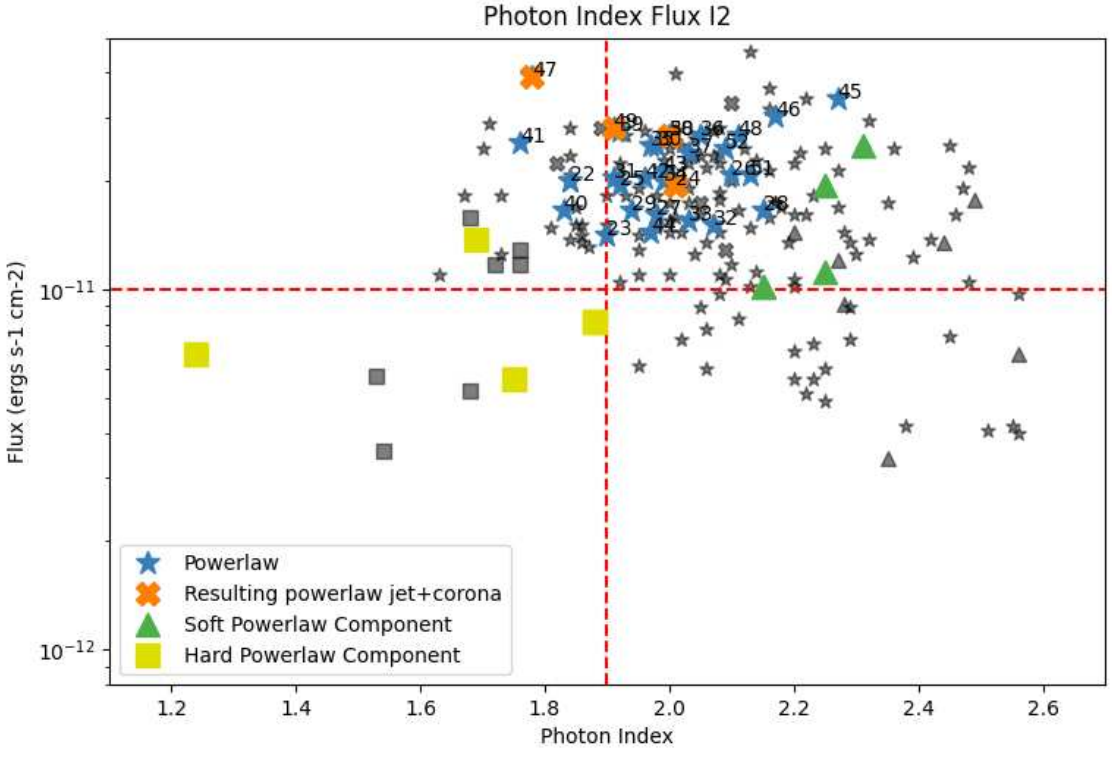

Figure 46: Photon index flux plot of interval I2=55200-55600 (2010-01-04, 2011-02-08)

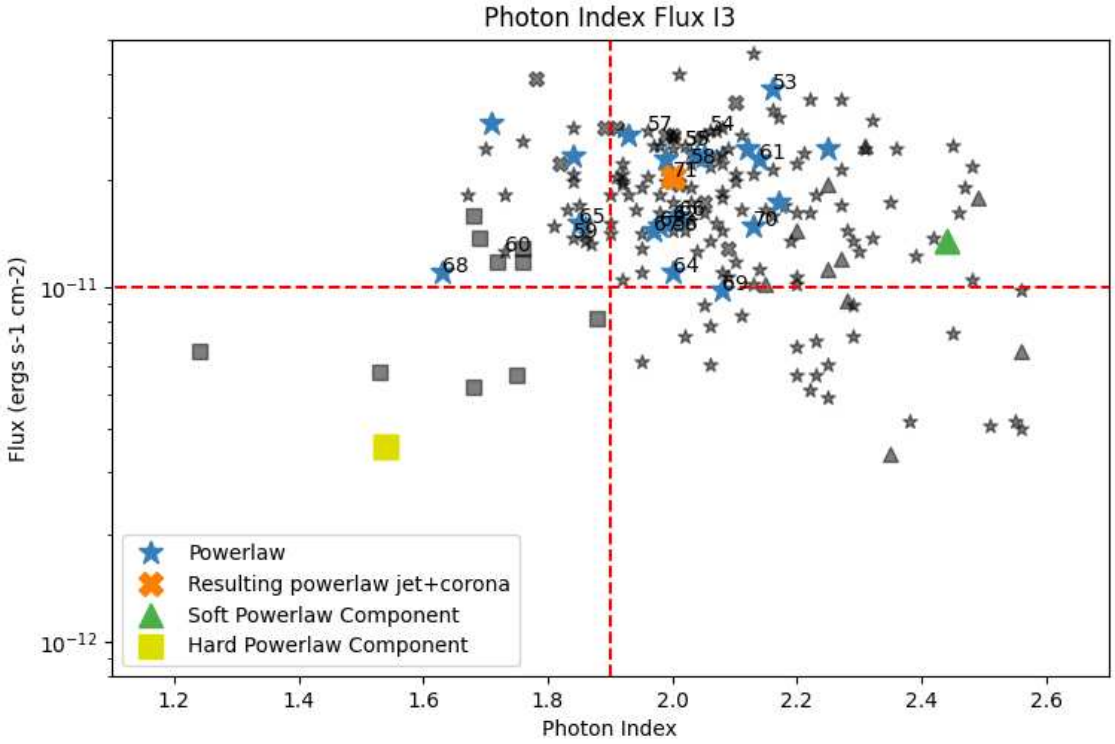

Figure 47: Photon index flux plot of interval I3=55600-56400 (2011-02-08, 2013-04-18)

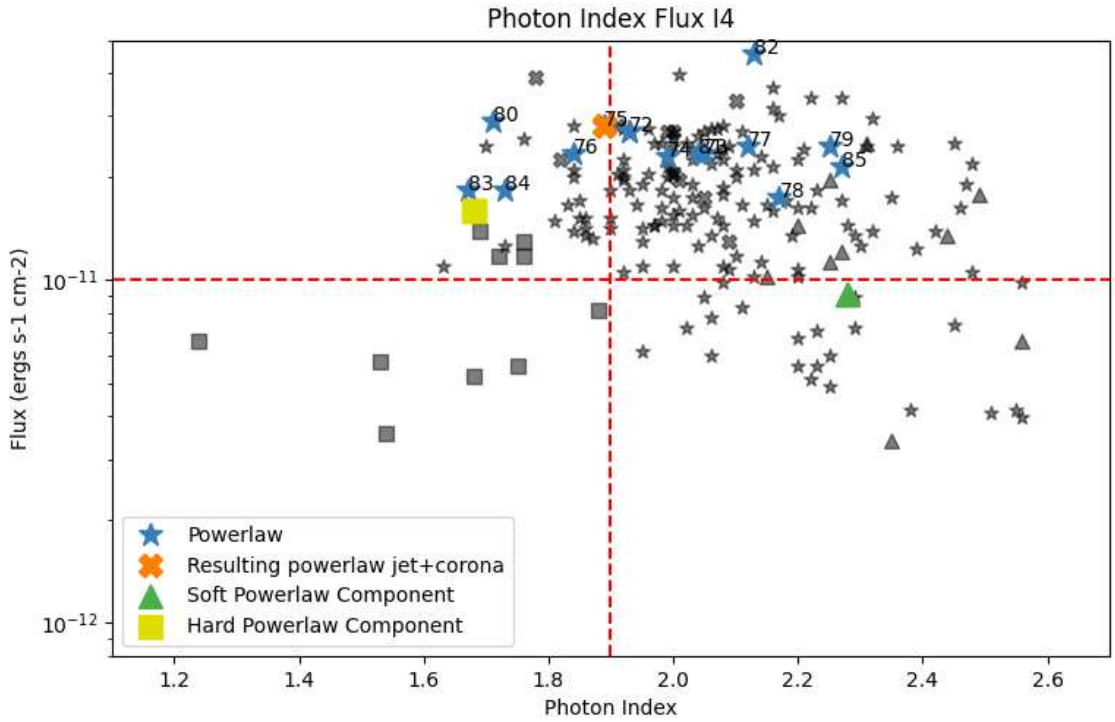

Figure 48: Photon index flux plot of interval I4=56400-56600 (2013-04-18, 2013-11-04)

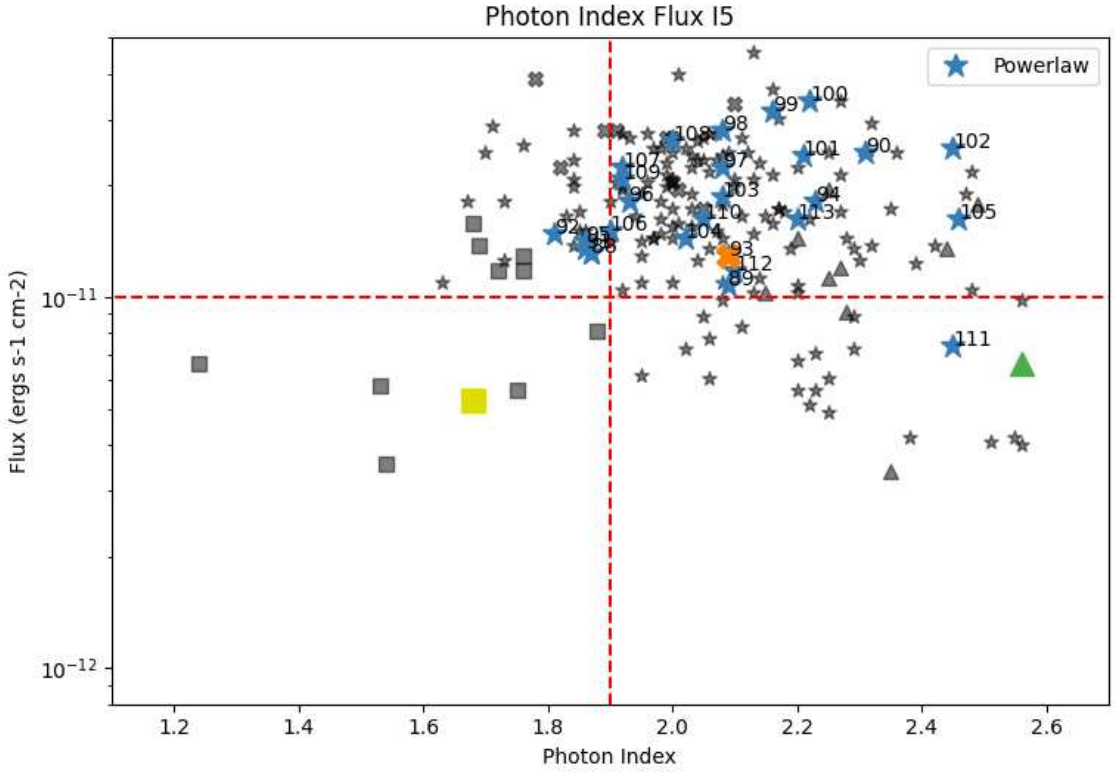

Figure 49: Photon index flux plot of interval I5=57200-57400 (2013-11-04, 2016-01-13)

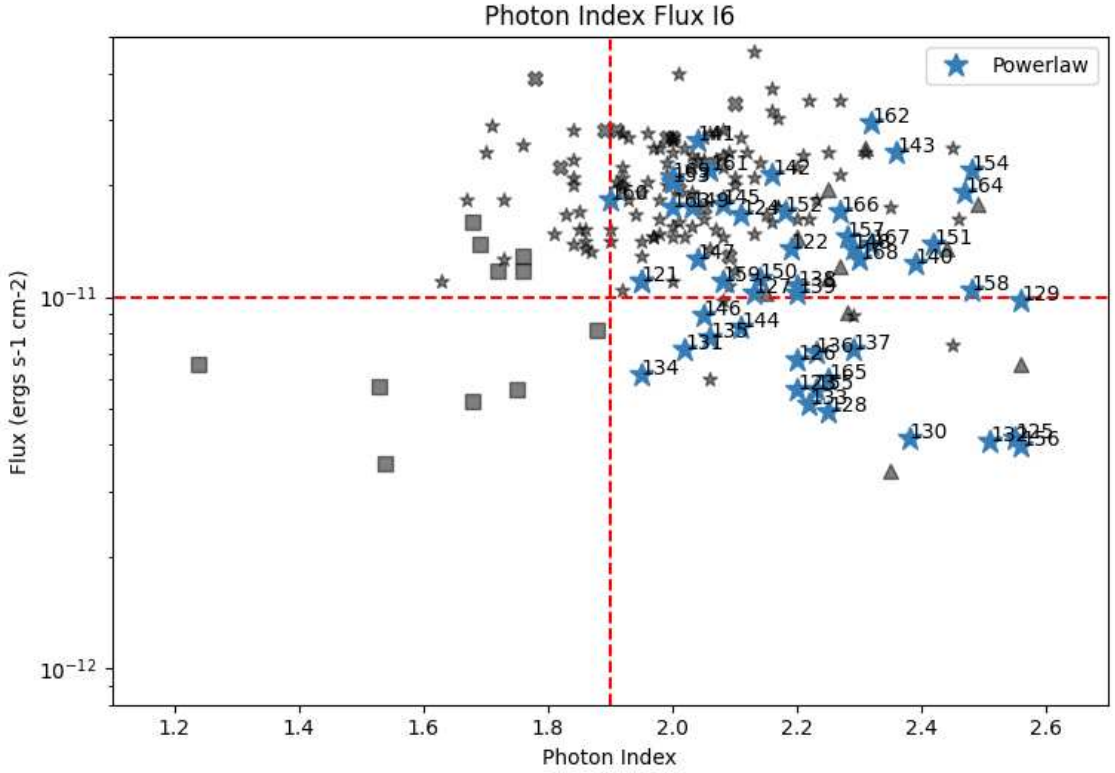

 Figure 50: Photon index flux plot of interval I6=57400-60000 (2016-01-13,2023-02-25)

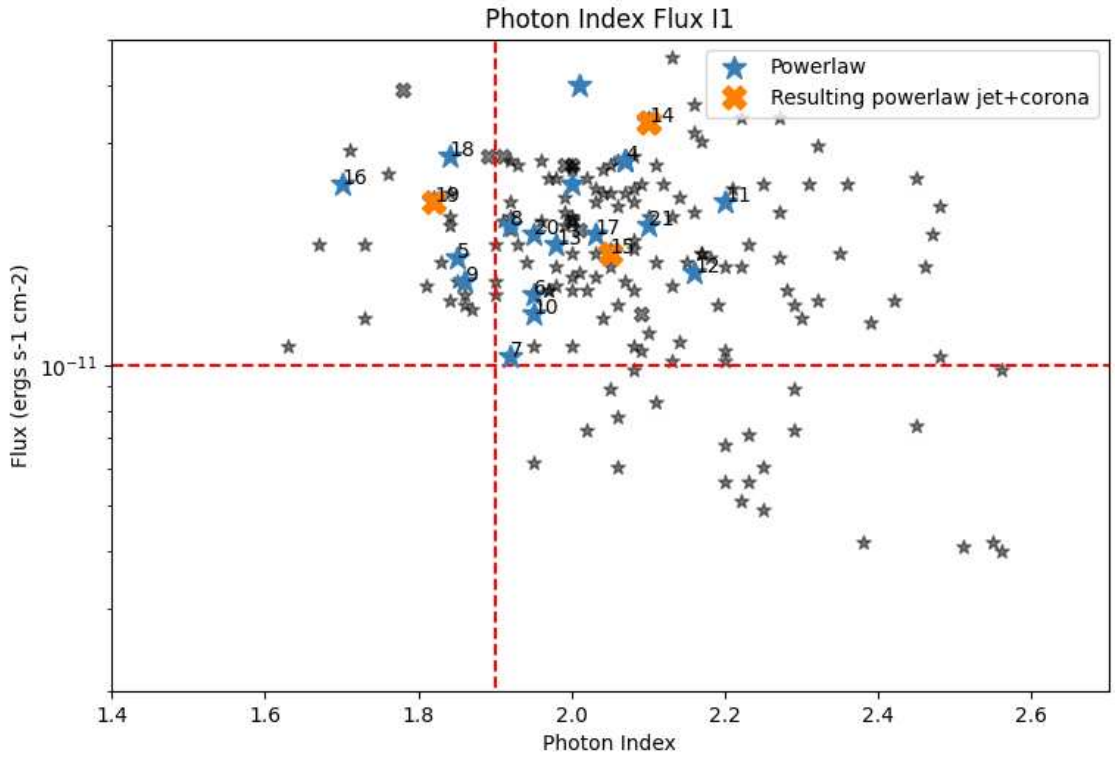

Figure 51: Photon index flux plot of interval I1=54000-55200

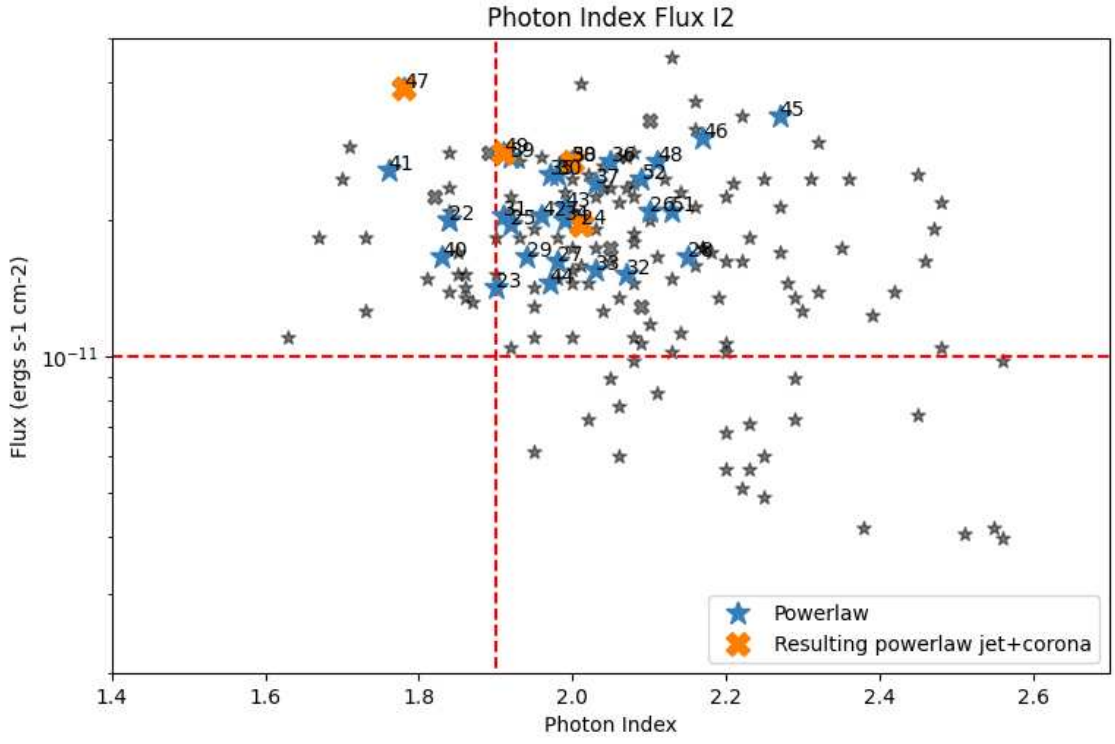

Figure 52: Photon index flux plot of interval I2=55200-55600

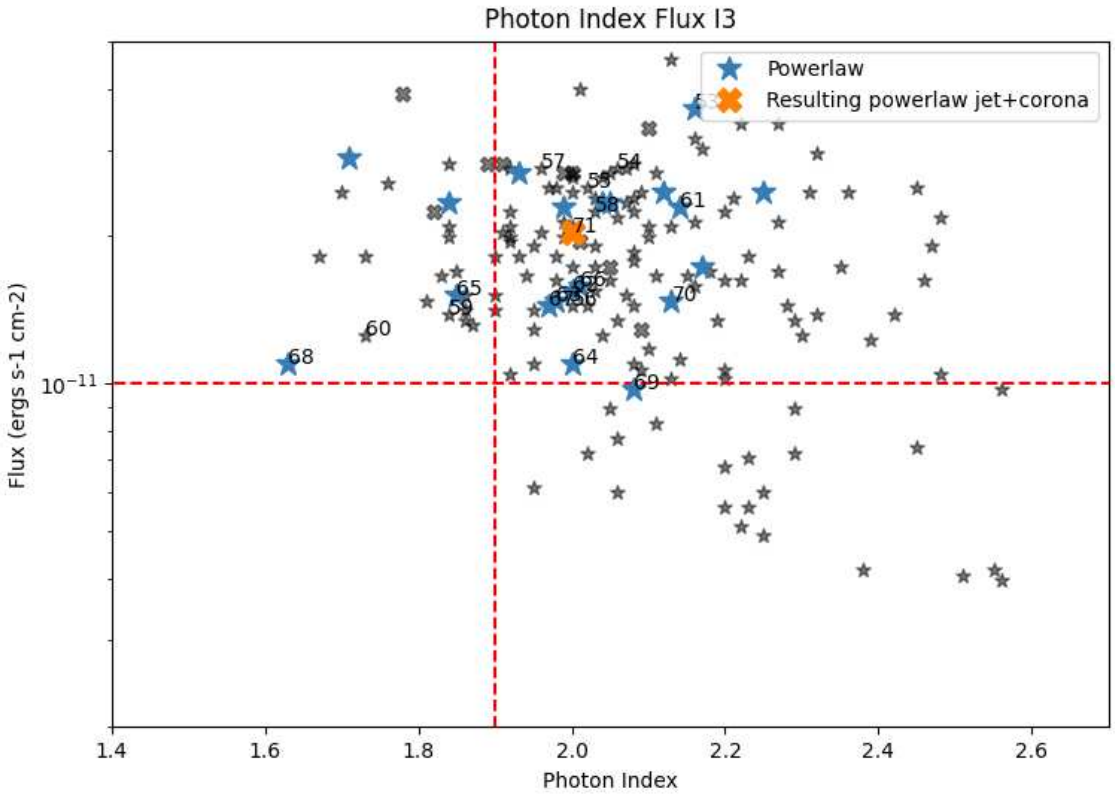

Figure 53: Photon index flux plot of interval I3=55600-56400

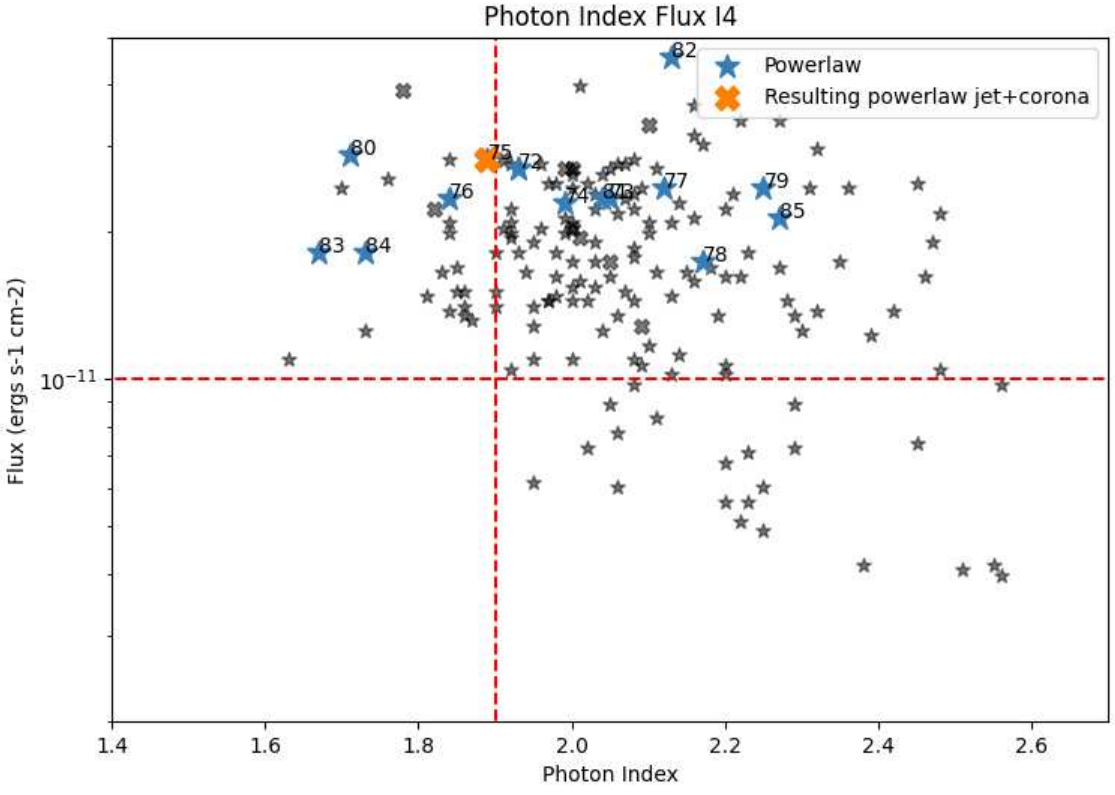

Figure 54: Photon index flux plot of interval I4=56400-56600

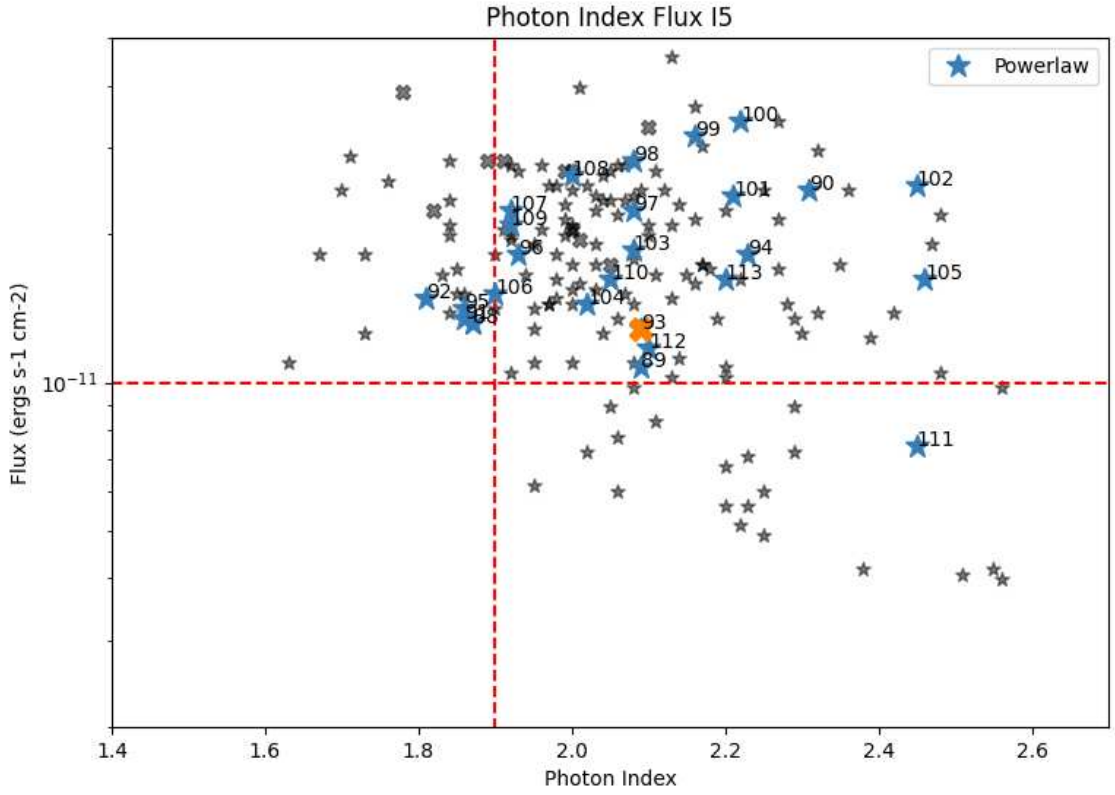

Figure 55: Photon index flux plot of interval I5=57200-57400

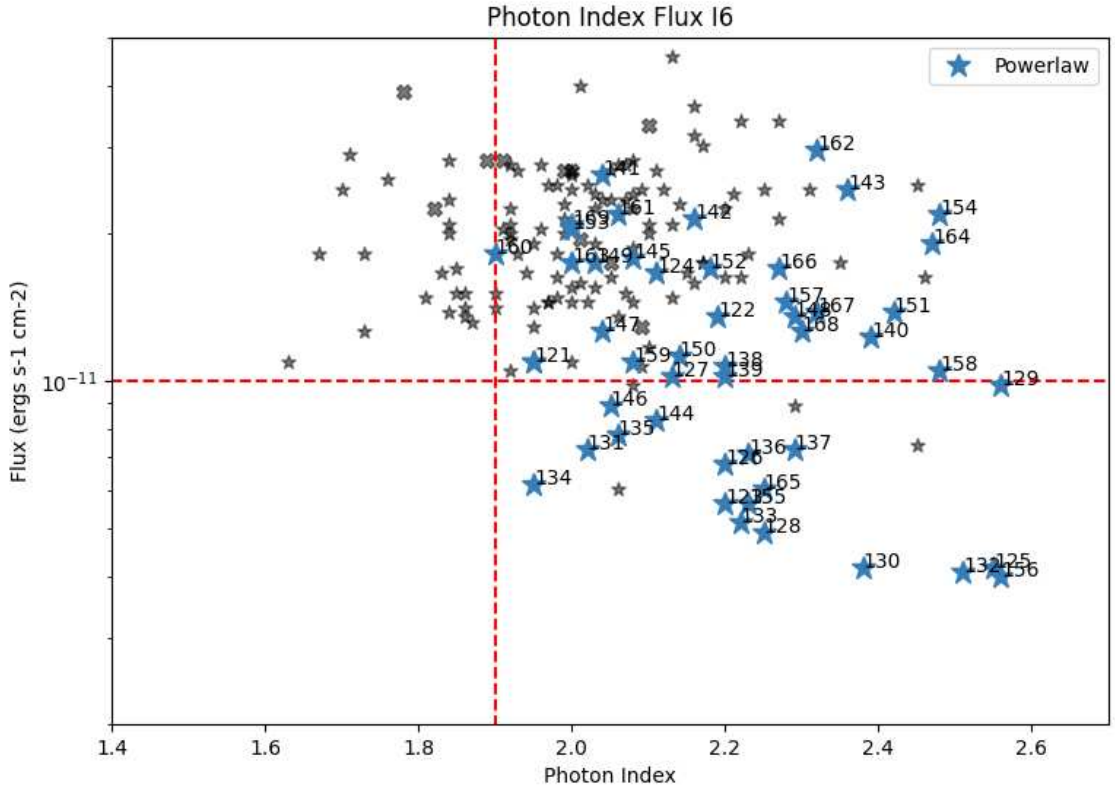

Figure 56: Photon index flux plot of interval I6=57400-60000

- We notice the absence of transitions from *zone* 1 to *zone* 3, which aligns with the hypothesis that jet generation may be closely linked to the coronal electron processes. This specific pattern further strengthens the association between certain coronal conditions and the presence of jets.
- We question whether the decrease in flux can be justified by a change in the accretion rate, which could also constitute an explanation for the absence of jets.

Another interesting feature is observed especially in Interval 2 data: these data exhibit high flux values overall. The peculiar feature is the apparent trend linking harder powerlaw indices with lower fluxes and vice versa, which can may be a result from absorption of higher frequency radiation.

Looking closely to the I2 interval graph, observing the annotations to points, one can notice that points placed on the upper right area of the graph (high flux-softer powerlaws), are followed almost immediately from points placed in the lower left area of the graph (lower fluxes - harder powerlaws) and this could mean that the first condition is what favours a jet emission.

To gain a deeper understanding of these observed features we now analyse UVOT parameters to see if any of the values exhibit variation counterparts.

6.2 UVOT data

Keeping the same intervals introduced above, I plotted light curves showing optical, UV and X-ray fluxes:

Up to approximately MJD 56000, these bands tend to roughly mirror the patterns observed in X-ray fluxes.

However, a distinct deviation from this behavior was remarkably evident during

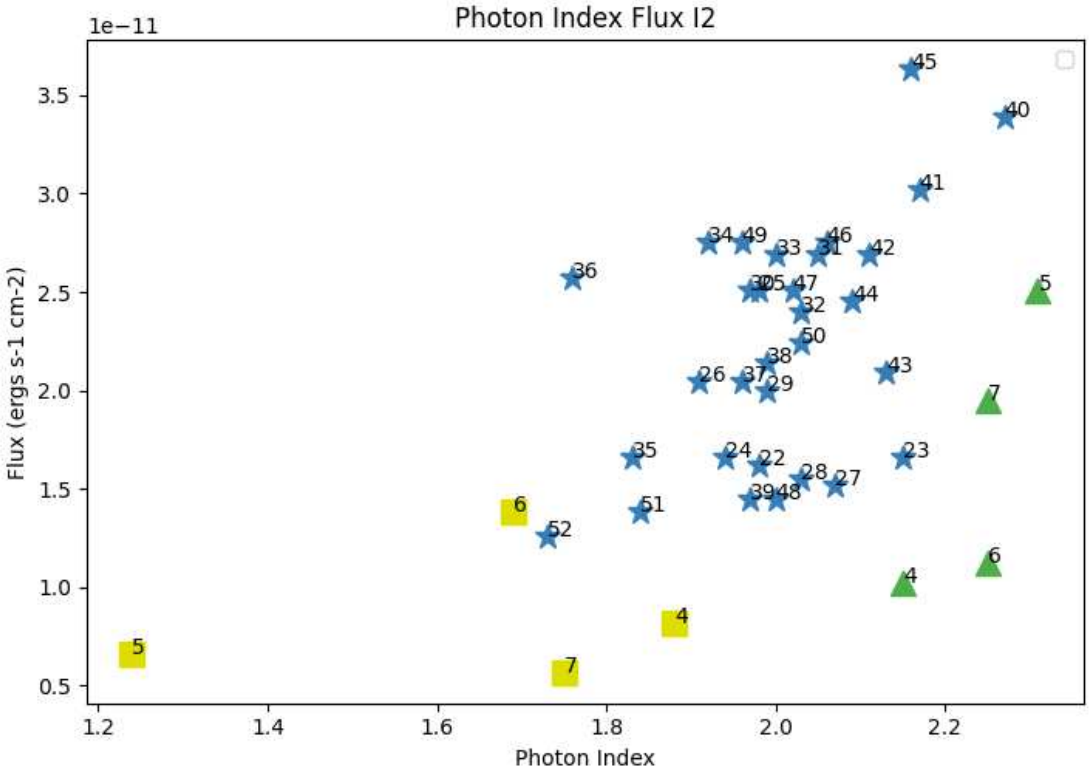

Figure 57: Photon index flux plot of interval I2 with broken powerlaw components

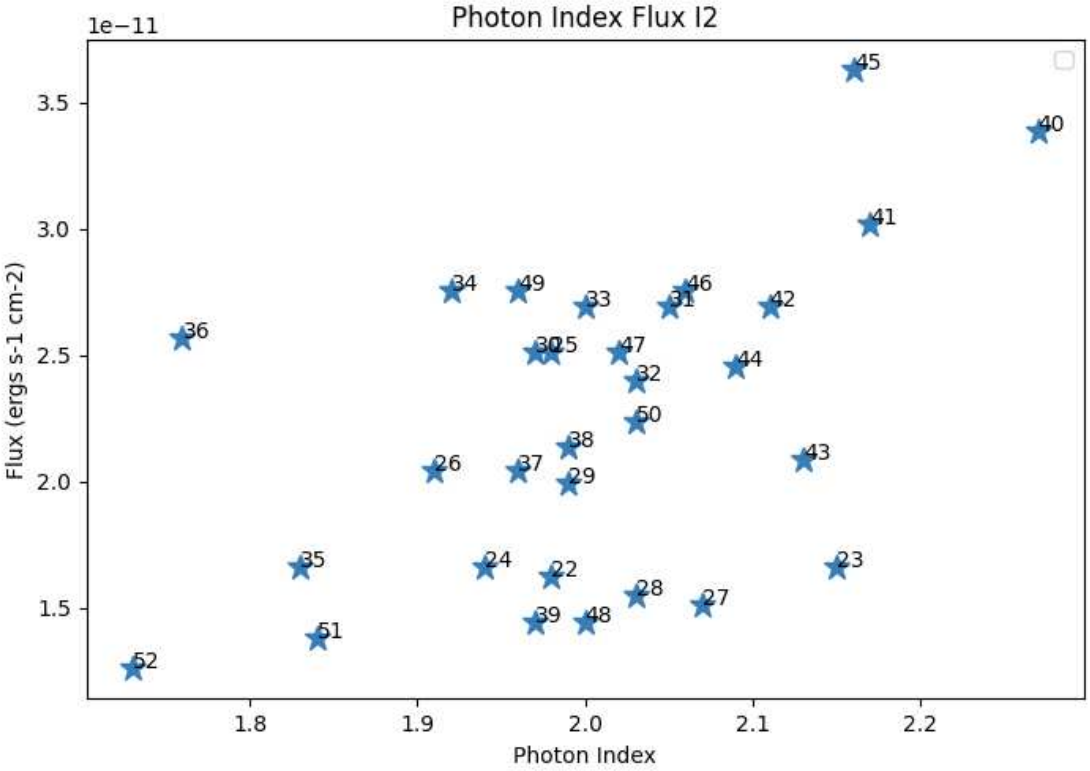

Figure 58: Photon index flux plot of interval I2

Figure 59: I2 trend with points labeled according to temporal order

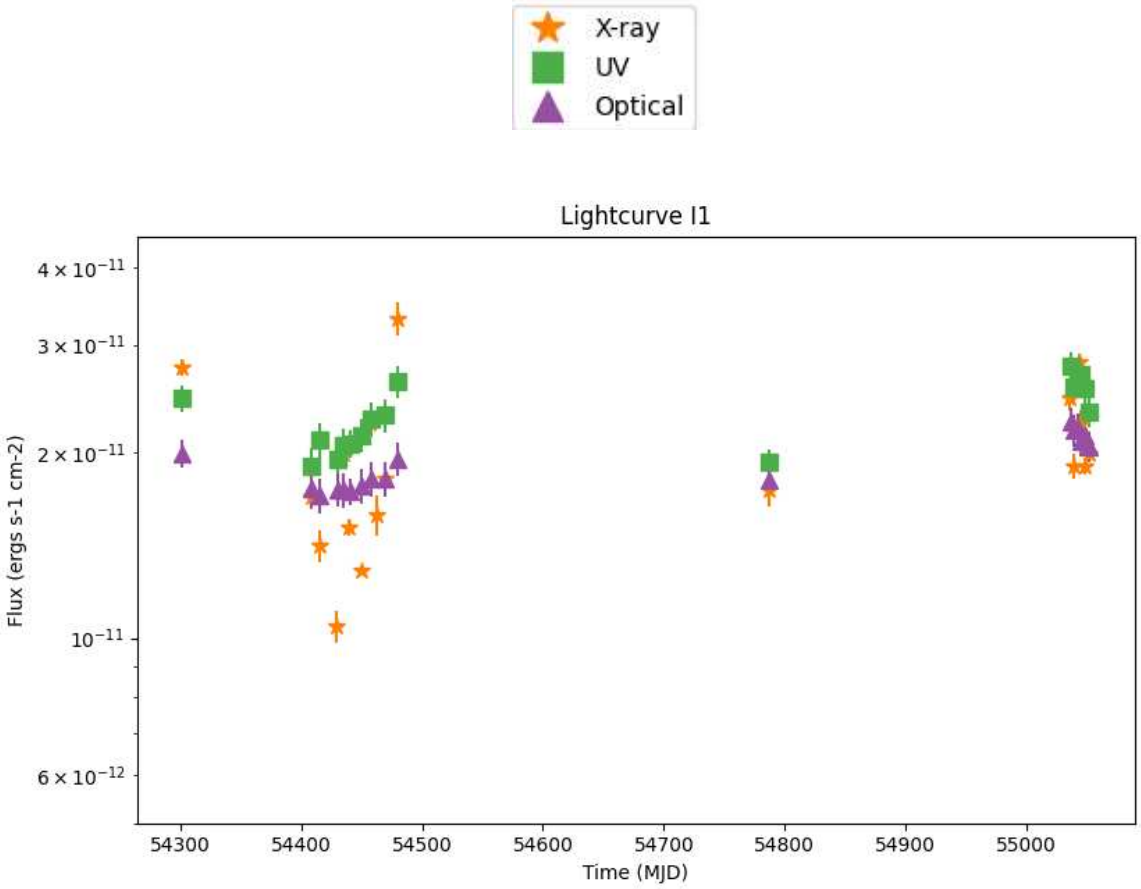

Figure 60: Lightcurve plot of interval I1=54000-55200

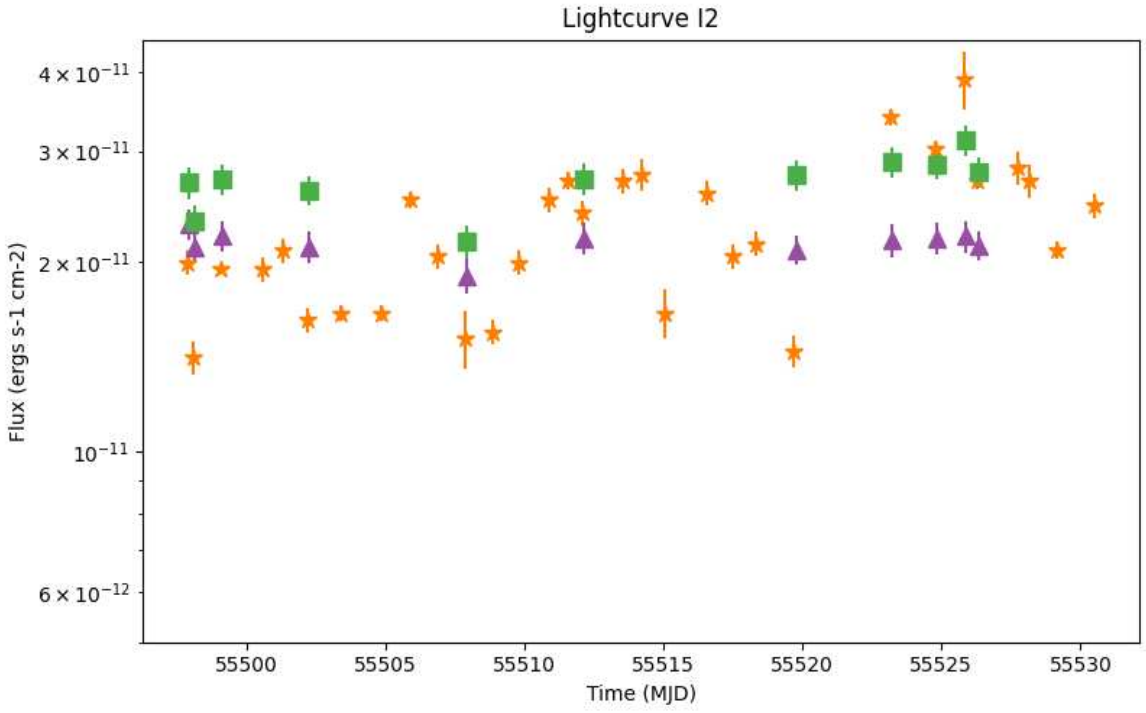

Figure 61: Lightcurve plot of interval I2=55200-55600

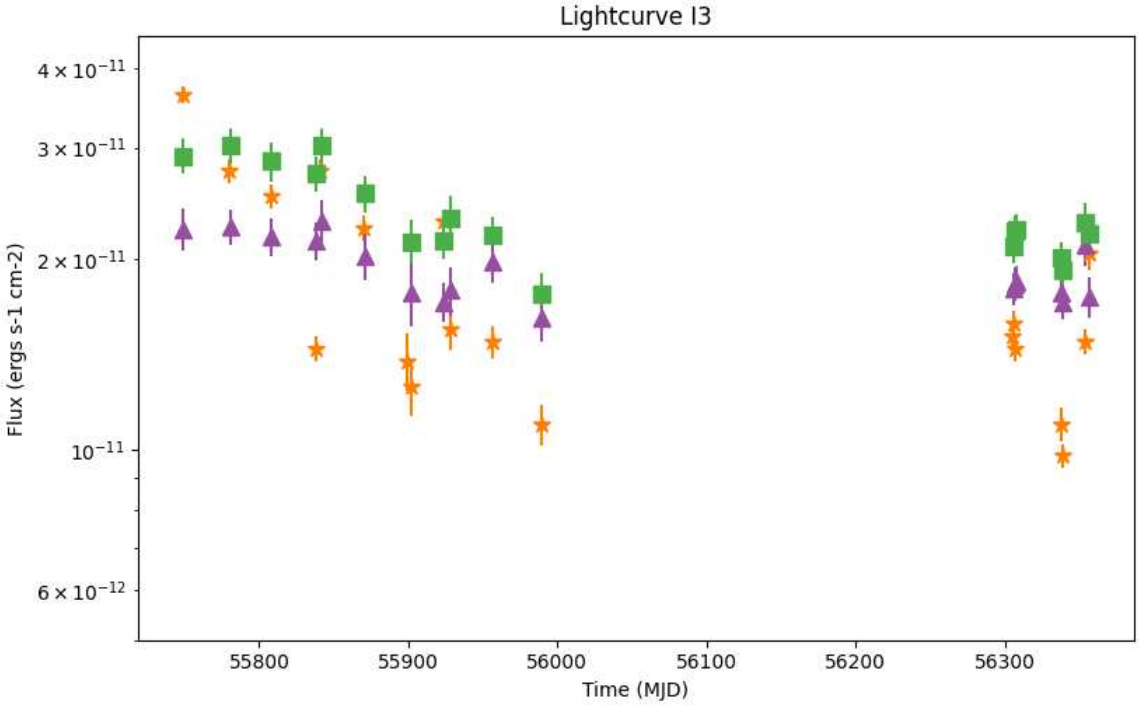

Figure 62: Lightcurve plot of interval I3=55600-56400

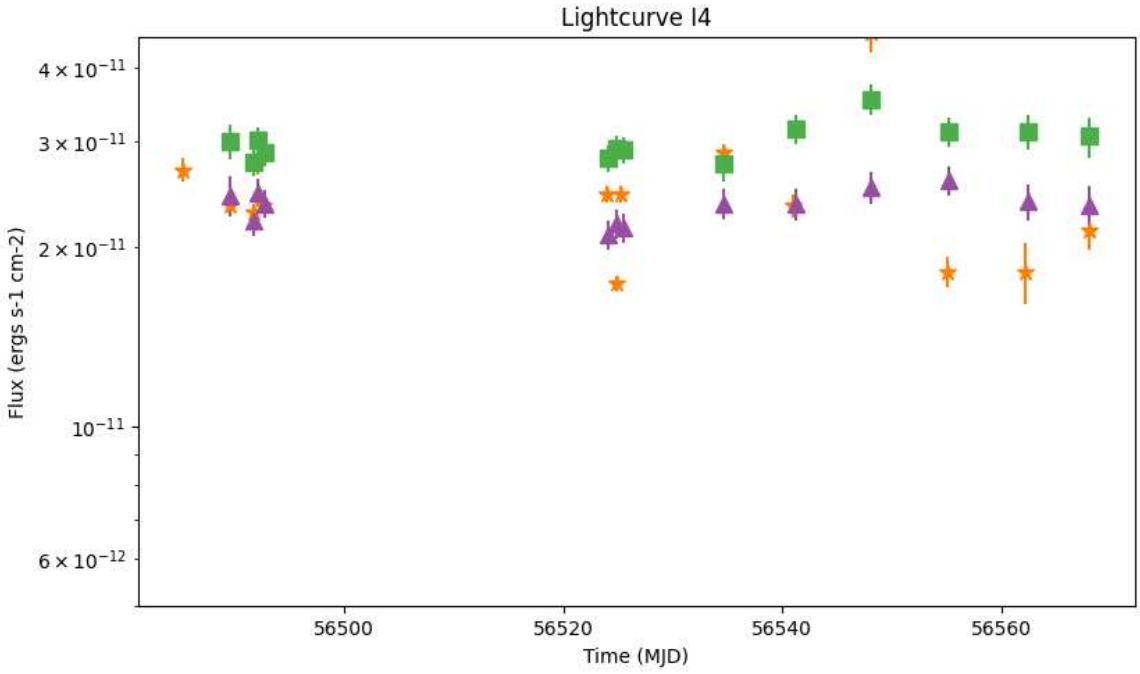

Figure 63: Lightcurve plot of interval I4=56400-56600

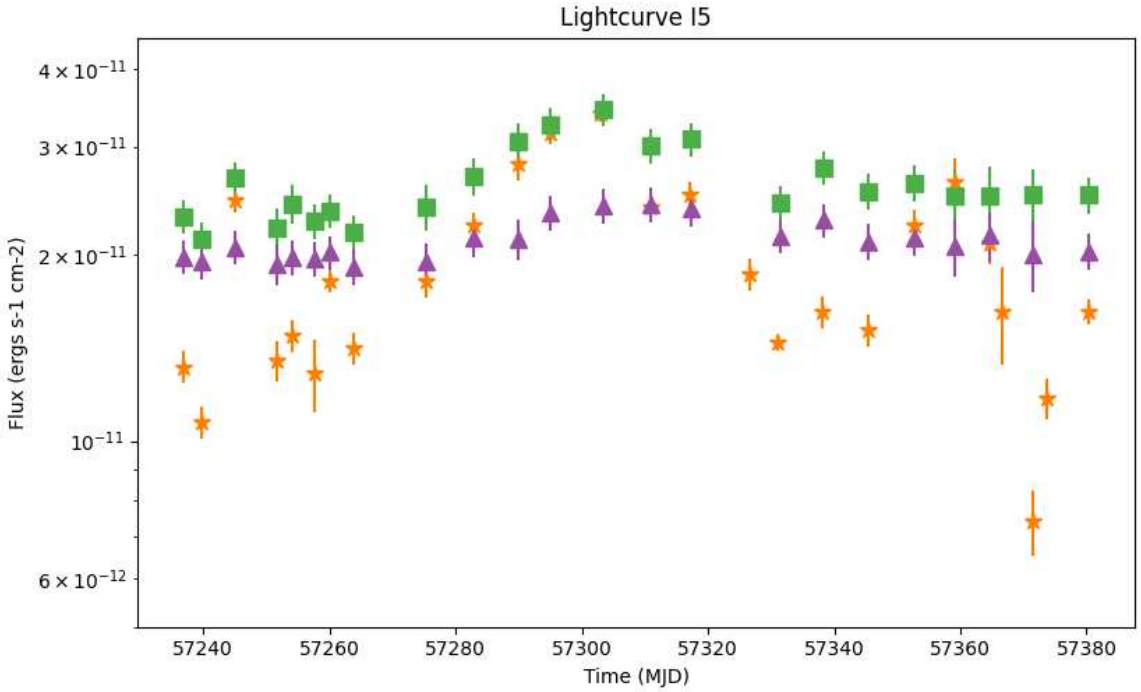

Figure 64: Lightcurve plot of interval I5=57200-57400

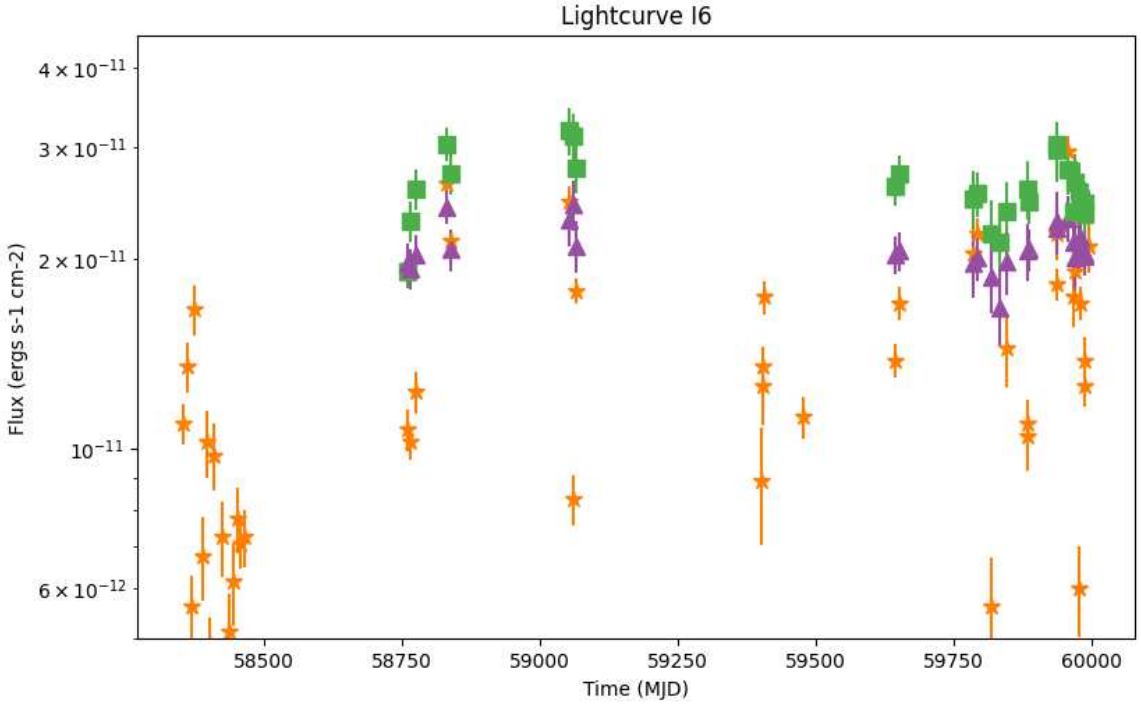

Figure 65: Lightcurve plot of interval I6=57400-60000

the intervals labeled as I5 and I6. During these specific timeframes, X-ray flux values displayed a notable decline, while UV and optical fluxes appeared to maintain relatively constant levels.

This affirmation finds further support in the plots representing data from the three defined *zone*s. The visual representation of data attributed to *zone*3, in particular, reaffirms our previous assertions.

Within the UV band, the fluxes in *zone* 3 do not display the declining trend observed in X-ray fluxes during the specified intervals.

This divergence in behavior prompts a closer examination of the underlying mechanisms responsible for the observed dynamics in different spectral domains and their relationship with X-ray flux variations.

Looking at the graph plotting UVOT fluxes as functions of X-ray flux, we notice that even though there is a subtle increasing trend in UV flux values as X-ray fluxes increase, the values themselves exhibit limited variation across the distinct *zone*s under consideration.

We are driven to dismiss the explanation suggesting that a decline in the accretion rate has occurred. The key indicators in the UV/optical bands, primarily associated with disk emission, remain relatively stable. Instead, our focus turns to the possibility of variations in the coronal plasma within the AGN system to explain the decline of the jet emission.

To characterize these distinct *zones* further in terms of UV and optical fluxes, an evaluation of the average flux levels in each zone was performed. The results confirmed that the fluxes within these bands did not exhibit significant changes across the different *zones*.

Additionally, aiming to gain deeper insights, I computed the average spectral

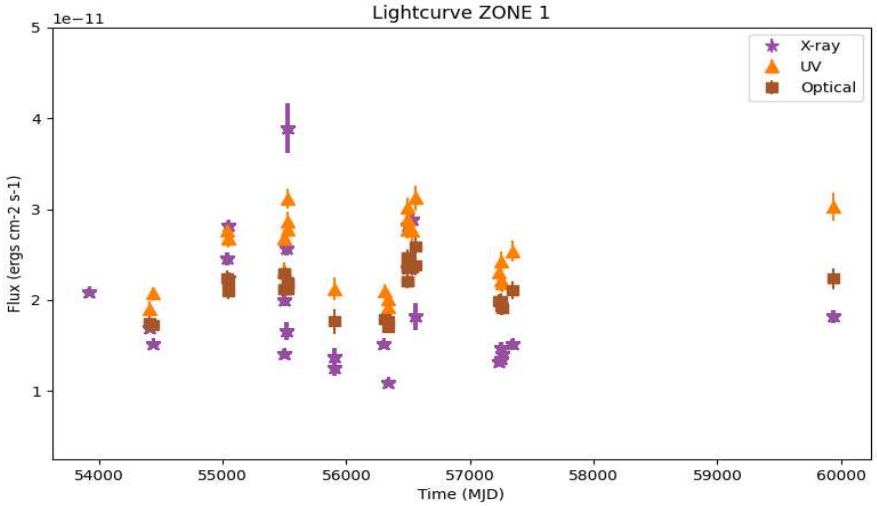

Figure 66: Lightcurve plot of *zone* 1

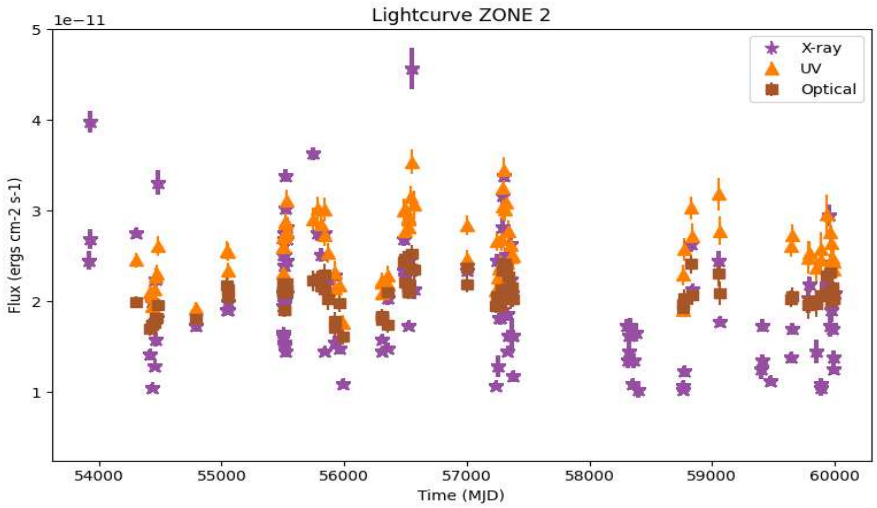

Figure 67: Lightcurve plot of *zone* 2

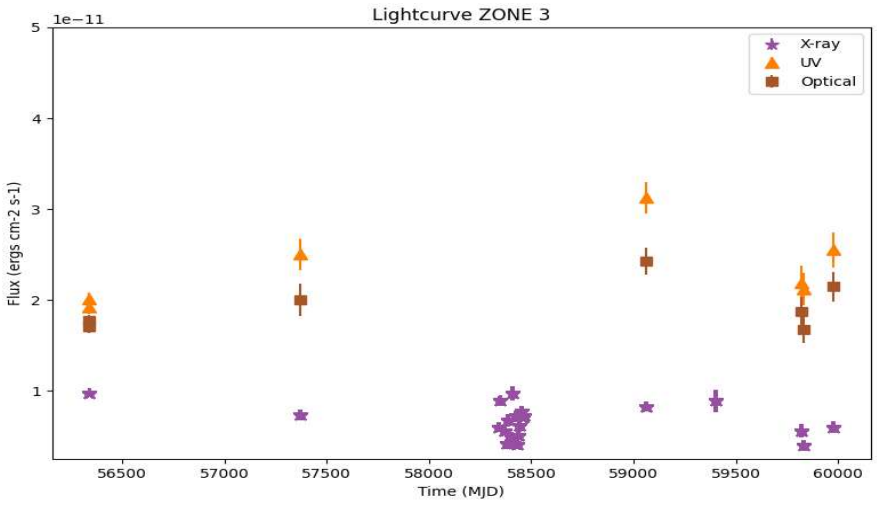

Figure 68: Lightcurve plot of *zone* 3

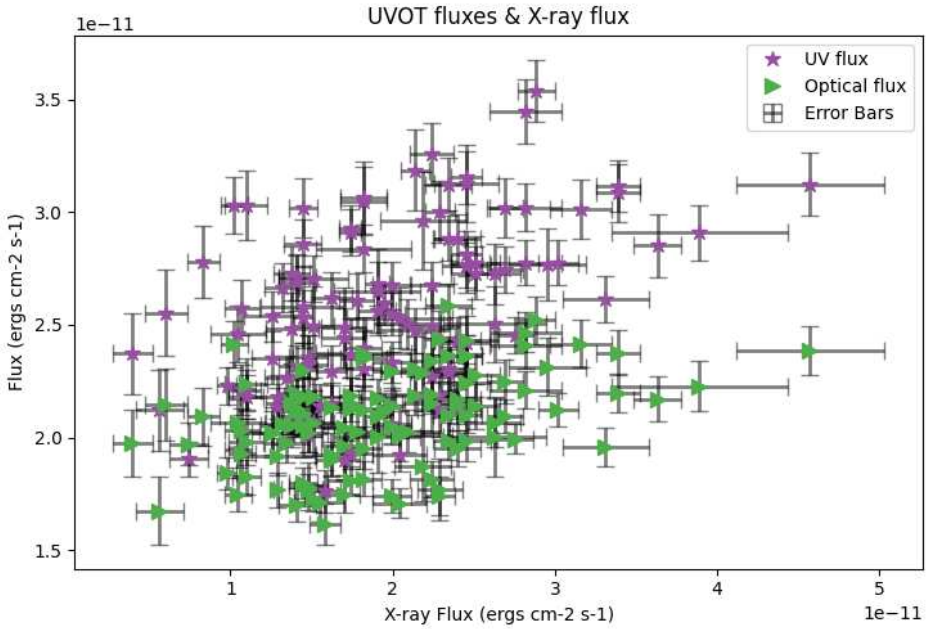

Figure 69: UVOT fluxes as functions of X-ray flux

	α_{UV}	α_{opt}
zone 1	-0.176 ± 0.048	0.629 ± 0.021
zone 2	-0.226 ± 0.062	0.601 ± 0.034
zone 3	-0.106 ± 0.015	0.809 ± 0.012

Table 5: Average spectral indices for the three zones

indices for each *zone* within the UV and optical bands. What emerged from this investigation was intriguing: *zone* 3 data showed power laws bending towards lower frequencies in both the UV and optical bands.

When examining the averaged spectral slopes, the distinct pattern came to light. Graphs plotting $f^{-\alpha}$ as a function of frequency f in the UV and optical bands revealed that *zone* 3 data displayed a pronounced distribution towards lower frequencies in both spectral domains. This intriguing observation can lead to interesting considerations related to accretion disk variations in temperature, for example.

While the accretion rate itself may not have experienced a noticeable decrease,

the shift towards lower frequencies suggests that various processes could be at play, possibly leading to a cooling of the accretion disk. It is plausible that these processes are intricately linked to the observed cessation of jet emission within the AGN.

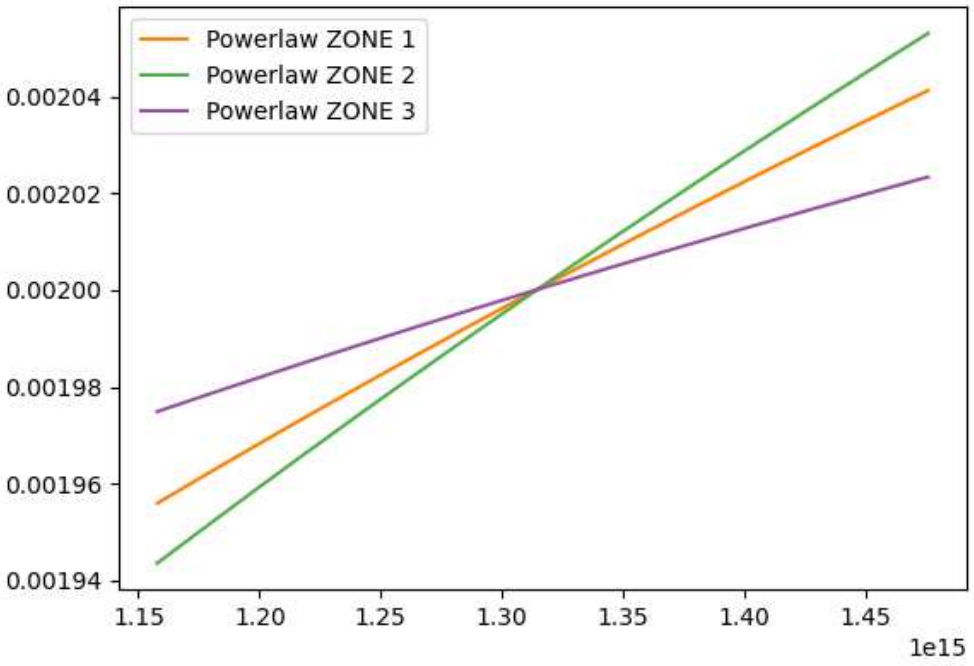

Figure 70: Plot of $f^{-\alpha}$, f frequency values in the UV band.

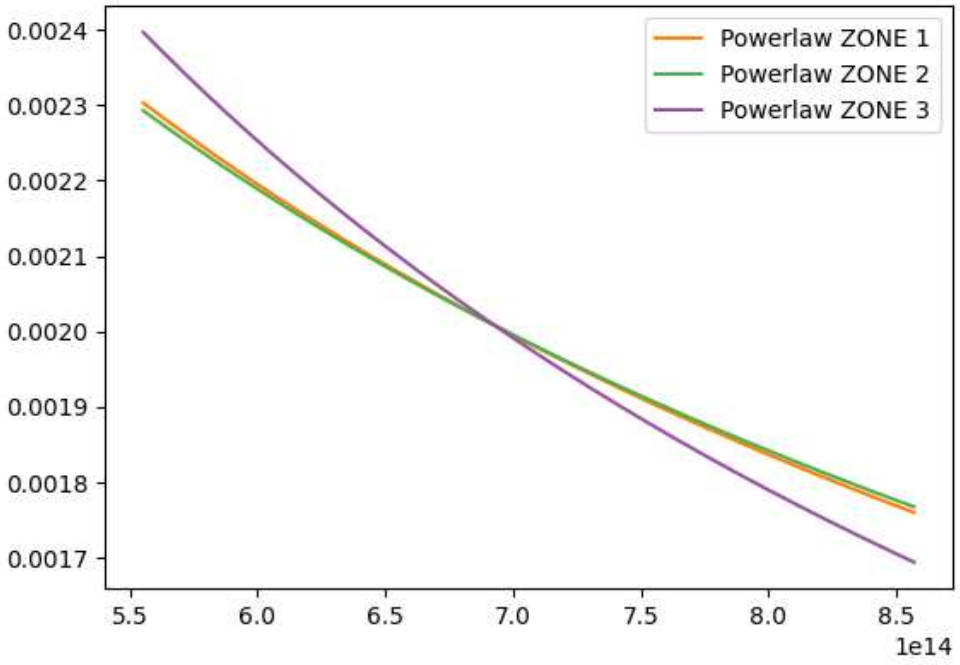

Figure 71: Plot of $f^{-\alpha}$, f frequency values in the optical band.

6.3 X-ray and Gamma Ray correlations

The gamma-ray photon index-flux plot roughly follows the trend shown during the X-ray analysis. In this case no equivalent counterpart of the X-ray *zone* 2 is distinguished.

Unfortunately, only a limited number of X-ray observations has a corresponding dataset in the Fermi LAT Database, so we use a limited set of "checks" to assess the expected jet emission.

I decided to roughly divide Fermi LAT data into two time intervals: I_1 containing observations taken before MJD 57000 (2014-12-09) and I_2 containing observations taken after MJD 57000. The photon index-flux plot shows both a softening of the spectrum, with higher values of Γ_γ and lower flux values.

Consequently, this prompts us to consider the possibility that the jet emission may have gradually decreased over time without a complete depletion.

We emphasize though, that these available gamma-ray data are insufficient for a precise and direct comparison with the X-ray observations, we use them for a general and approximate confront.

I also plotted the gamma ray flux as a function of x-ray flux values selecting XRT observations taken within 2 days from gamma observations.

We observe that generally low values for X-ray flux correspond to low values in the gamma ray band. The trend is more complex at higher X-ray values confirming the previous affirmations on the role of the corona dominating the X-ray spectrum in various situations.

To perform a more detailed analysis I selected some interesting time-intervals to compare the X-ray spectral values with the gamma-ray ones aiming to char-

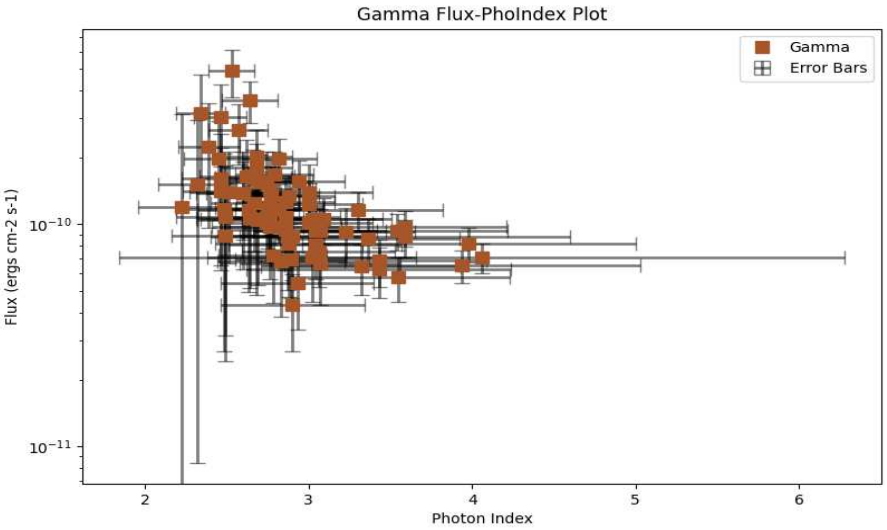

Figure 72: Gamma ray photon index-flux graph with error bars.

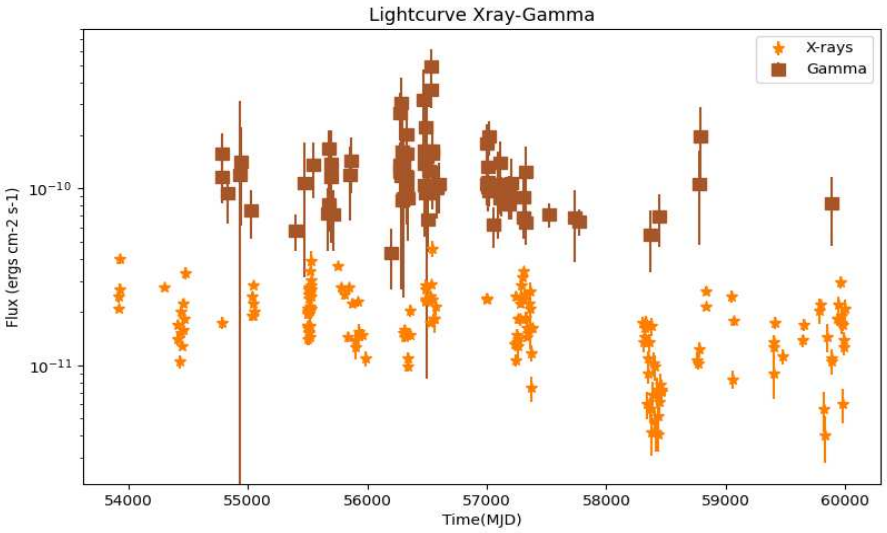

Figure 73: Gamma and X-ray light-curves in logarithmic scale

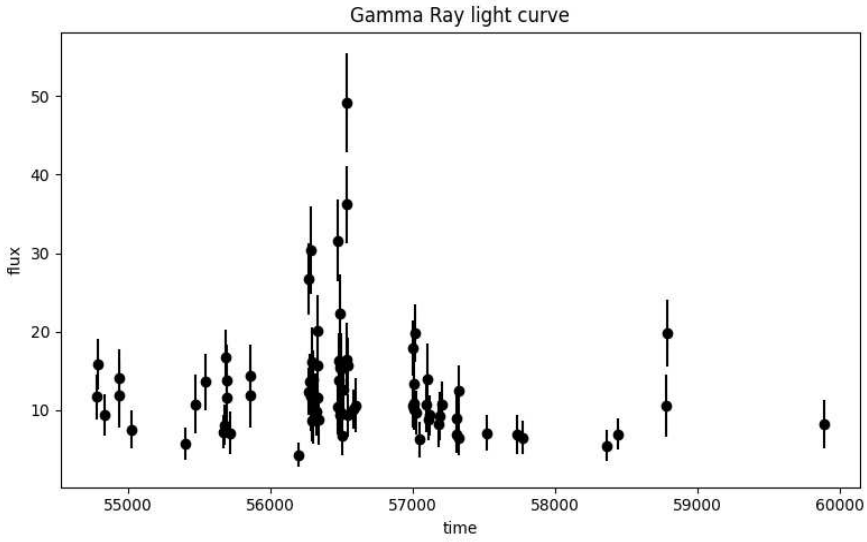

Figure 74: Gamma ray light-curve plot

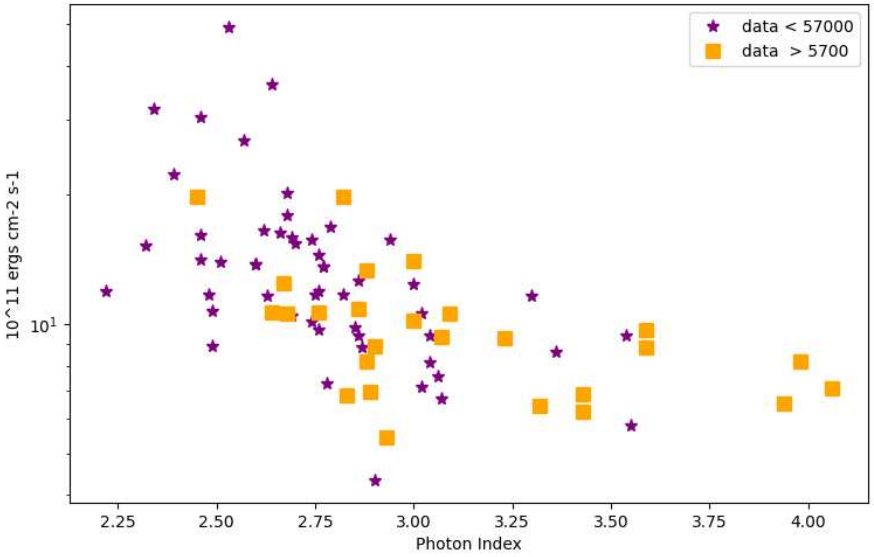

Figure 75: Plot of I_1 and I_2 Photon Index-Flux

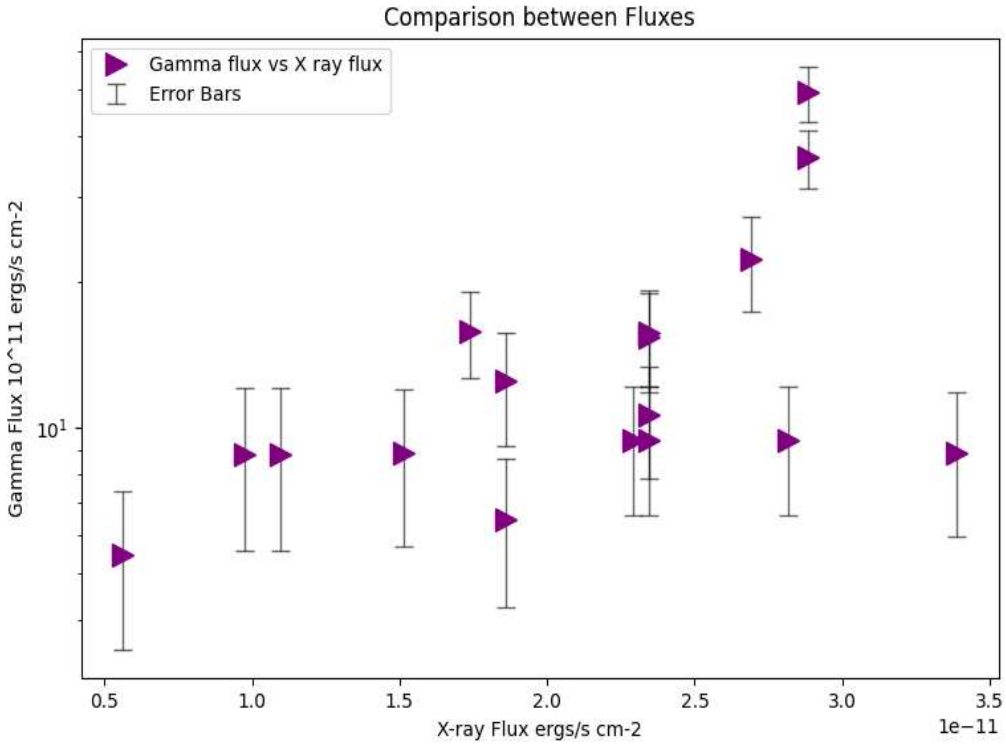

Figure 76: Gamma ray flux against X-ray flux

Table 6: X-ray and Gamma Ray data 56533-56536

Time MJD	PhoIndex	Flux $10^{-11}\ ergs\,cm^{-2}s^{-1}$
56535	1.71 ± 0.16	2.88 ± 0.02
Time MJD	PhoIndex	Flux $10^{-14}\ ergs\,cm^{-2}s^{-1}$
56533	-2.64 ± 0.17	36.18 ± 4.95
56536	-2.53 ± 0.14	49.17 ± 6.36

Table 7: X-ray and Gamma Ray data 56483-56489

Time MJD	PhoIndex	Flux $10^{-11}\ ergs\,cm^{-2}s^{-1}$
56485	1.93 ± 0.06	2.69 ± 0.03
56489	2.05 ± 0.05	2.34 ± 0.03
Time MJD	PhoIndex	Flux $10^{-14}\ ergs\,cm^{-2}s^{-1}$
56483	-2.66 ± 0.17	16.32 ± 3.47
56486	-2.39 ± 0.19	22.33 ± 4.96
56489	-2.70 ± 0.24	15.42 ± 3.55

acterise the jet's emission.

The highest gamma ray fluxes are detected during 56533 (2013-08-29) and 56336 (2013-02-13) dates and we have an X-ray detection the day after, whose spectrum is modeled by a single powerlaw with a very hard photon index, 1.74 displaying also one of the highest X-ray flux value.

Other high gamma ray detections were obtained between days 56486 (2013-07-13) and 56489 (2013-07-16) and correspond to high fluxes in the X ray band, even though powerlaws do not exhibit very hard slopes.

Table 8: X-ray and Gamma Ray data 56998-57007

Time MJD	PhoIndex	Flux $10^{-11}\ ergs\,cm^{-2}s^{-1}$
57001	2.07 ± 0.06	2.34 ± 0.02
57003	2.08 ± 0.07	2.42 ± 0.03
Time MJD	PhoIndex	Flux $10^{-11}\ ergs\,cm^{-2}s^{-1}$
56998	-2.68 ± 0.22	17.94 ± 3.53
57001	-3.09 ± 0.42	10.6 ± 2.77
57007	-2.86 ± 0.33	10.83 ± 2.8

6.4 Possible explanations

The observed decreasing flux in the X-ray band can have multiple origins. Here below we list some interesting scenarios as suggested explanations for X-ray variations.

6.4.1 The Blandford-Znajek theory revisited

To motivate our observations we provide references to the revised theory of Blandford-Znajek (BZ) by Foschini (2012b)).

In this scenario, it is not only the black hole spin which determines the power of the jet, but also the angular frequency of the magnetic field lines $\omega_{\rm F}$, related to the rotation velocity of the disk itself. More precisely the slip factor s was defined to characterize this process:

$$s = 1 - \frac{\omega_{\rm H}}{\omega_{\rm F}} \tag{6.2}$$

where $\omega_{\rm H}$ is the black hole angular velocity.

There can be several situations that can lead to different outcomes, in particular we cite two scenarios that can be related to our source conditions:

- $\omega_H > \omega_F$, $s < 0$: the black hole angular speed is greater than that of magnetic field lines. The machine works as generator and the BZ power is positive so jet emission is occurring. The rotational power of the black hole is converted into the electromagnetic jet power.
- $\omega_H < \omega_F$, $0 < s < 1$: the BZ power is negative, the machine works as a motor. The rotational energy of the magnetic field, which rotates faster than the BH, is extracted to power the motion of the black hole and no jet is generated. If the BH increases its angular speed sufficiently to surpass that of the field, then it changes to the condition explained above.

Now, in the context of our observations, we suspect that there might have been changes in the magnetic field lines angular velocity and, presumably, the rotation of the accretion disk and hence leading to a ceased emission. This change could be a key factor in explaining why we no longer observe jet emission in our source.

6.4.2 Disk Instability

An alternative explanation for this behavior is derived from the study conducted by Czerny et al. (2009).

In their investigation they associate the existence of short-lived compact radio sources with the intermittent activity of the central engine, caused by a radiation pressure instability within an accretion disk.

It was already known that AGN were subject to subsequent stages of varying activity levels. They show an intermittent behavior, likely triggered by minor mergers or instabilities in the accretion flow over extended timescales, up to 10^8

years.

However, discrepancies arose from several studies revealing an excess of compact ("young") sources compared to galaxies with extended old radio structures. In response, a scenario suggesting intermittent activity occurring at a faster rate than the known long scale intermittent behaviour was proposed. According to this model, the source is reborn every few thousand years, without displaying strong evidence of the previous activity phase, as extensively discussed by various authors. The plausible explanation is an accretion disk instability manifesting on timescales much shorter than 10^8 years. In fact, cold accretion disks experience two types of instabilities: ionization instability, acting over longer timescales, and radiation pressure instability, operating on shorter timescales and causing periodic outbursts.

The time evolution of an accretion disk under radiation pressure instability is rapid, with the exact boundary of the unstable region being mostly depending on the accretion rate. The instability occurs if $\dot{M} > 0.025$ approximately. The radiation pressure instability implies alternating between thermally stable states: an outburst with a high-accretion rate and a low accretion rate state. During an outburst, the disk remains nearly stationary, with a constant accretion rate, on timescales shorter than hundreds/thousands of years.

The temporary accretion rate during this state exceeds the Eddington rate, and thermal stability is maintained by energy advection to the black hole. Conversely, a low state ensues between outbursts, marked by a rapid decline in accretion rate, making the disk significantly nonstationary. Thermal stability in this state then results from a reduction in radiation pressure.

The variability timescales depend strongly on mass, with longer timescales related to higher black hole masses. Therefore, a specific cathegory is preferred

if we aim to observe such variations, as it shows evidence of lower mass black holes: narrow-line Seyfert 1 galaxies. For these sources the transition between states can occur in less than 40 years.

Let us focus specifically on the case of 1H 0323+342 and investigate whether the observed features can be related to such mechanisms. The softer and decreasing X-ray flux suggests a cooling in the inner regions. The UV-optical counterpart of the accretion disk component provides however an ambiguous feedback. As flux values do not decrease, we do not find enough evidence of a decreasing accretion rate. While fluxes remain constant, the spectral indices evaluated in *zone* 3 suggest that spectral powerlaws are bent towards lower frequencies, and therefore possibly lower temperatures. So we observe an overall change of behaviour in the inner environment, without however confirming a disk instability. Further research is needed to evaluate and eventually confirm this hypothesis.

Conclusions

The comprehensive analysis conducted in this thesis sheds light on the intricate dynamics of the jetted Narrow Line Seyfert 1 galaxy, 1H 0323+342, conducting a research over a 16-year period of observations. I performed a spectral analysis of X-ray data from the Swift-XRT telescope, integrating it with photometric analysis of UV and optical data from the Swift-UVOT telescope. Ultimately an additional combination of Fermi-LAT lightcurve values, has contributed to provide valuable insights into the temporal evolution of this intriguing AGN.

The identification of three distinct *zones* on the Photon Index-Flux plot has been a significantly relevant outcome of this study. The first phase (*zone* 1) is defined from fluxes $> 10^{-11}$ ergs $s^{-1}\,cm^{-2}$ and photon indices $\Gamma < 1.9$. Since it is characterized by high fluxes and hard spectra, we associate it to a scenario of vigorous jet activity. The second phase (*zone* 2) is defined from fluxes $> 10^{-11}$ ergs $s^{-1}\,cm^{-2}$ and photon indices $\Gamma > 1.9$, and is marked by high fluxes and soft spectra, suggesting a phase where the acceleration of coronal particles diminishes, potentially leading to a decline in jet emission. Most observations before MJD 57000 switch beetween *zone* 1 and 2, suggesting that *zone* 2 is the phase anticipating and /or following a jet emission. Finally, the third phase (*zone* 3) is defined from flux values $< 10^{-11}$ ergs $s^{-1}\,cm^{-2}$ and $\Gamma > 1.9$, so characterized by lower fluxes and soft spectra. This behaviour is particularly evident in recent observations, implying a possible cessation of jet emission. For every zone also a useful parameter was evaluated: the hardness ratio R_H, exhibiting a negative value in the average *zone* 3 spectra opposed to the two

positive values shown for *zone* 1 and 2 (with *zone* 1 having a higher value than *zone* 2). This parameter supports the supposed change of behaviour in this source, at least in the X-ray band.

UV and optical flux values exhibit a general stability over the observation period, therefore these observations do not confirm properly the variations observed in the X-ray band. However, subtle changes in UV and optical spectral indices suggest potential alterations within the accretion disk: the average UV spectral index $\alpha_{\mathrm{UV}} = -0.106 \acute{s} 0.015$, is higher than the average values calculated or *zone* 1 and 2, hence suggesting softer spectra. Also the value found for $\alpha_{\mathrm{opt}} = 0.809 \acute{s} 0.012$ is higher than the others. Furthermore, a small correlation between high X-ray flux and elevated UV and optical fluxes hints at underlying changes in the accretion disk. These observed features could indicate some minor changes in the accretion disk emission, without however exhibiting a proper decrease in the accretion rate.

Gamma-ray data from Fermi LAT, while exhibiting similarities to X-ray trends, can confirm only partially Swift observations, as the temporal overlap between the two survey datasets is limited. Nevertheless, the observed decreasing trend in gamma-ray values aligns with the overall diminishing trend seen in X-ray data, offering additional support for the hypothesis of decreased jet activity.

A number of scenarios could attempt to explain the observed behaviour; in this dissertation I propose two interesting hypothesis which both need subsequent research to be confirmed. The first one refers to the The Blandford-Znajek theory revisited, according to which the ceased emission could be related to changes in the magnetic field lines angular velocity and, presumably, the rotation of the accretion disk. The second one suggests that the ceased emission could be related to disk instabilities that in NLS1 galaxies can occur in less

than 40 years.

In conclusion, this thesis contributes to the field of AGN research, particularly in the context of jetted Narrow Line Seyfert 1 galaxies. The detailed multi-wavelength analysis shows the need for multiple techniques and approaches to unravel the intricate mechanisms that regulate the disk-corona-jet interactions. I believe they occur consistently, influencing the different components. This research provides material for future investigation regarding the short scale observed variations and their origin, so I hope it will open future avenues for exploring the broader implications of the observed phenomena. By comparing my results with other sources, I wish to add useful pieces to the intricate puzzle of AGN.

Appendix: XRT Parameters

Time MJD	Model	Γ_1	Flux$_1$ 10^{-11} $ergs\,cm^{-2}s^{-1}$	BreakE keV	Γ_2	Flux$_2$ 10^{-11} $ergs\,cm^{-2}s^{-1}$	χ^2
53921.56	Powerlaw	1.84 ± 0.12	2.09 ± 0.04				11.53/12
53922.04	Powerlaw	2.0 ± 0.04	2.45 ± 0.1				93.73/94
53925.45	Bknpowerlaw	2.27 ± 0.15	1.2 ± 0.08	1.49 ± 0.38	1.72 ± 0.16	1.17 ± 0.08	32.85/31
53925.99	Powerlaw	2.01 ± 0.03	3.98 ± 0.12				141.87/112
54301.71	Powerlaw	2.07 ± 0.04	2.75 ± 0.06				89.68/92
54408.13	Powerlaw	1.85 ± 0.11	1.7 ± 0.05				17.66/14
54415.09	Powerlaw	1.95 ± 0.1	1.41 ± 0.06				7.71/14
54429.75	Powerlaw	1.92 ± 0.13	1.05 ± 0.04				18.15/11
54435.18	Powerlaw	1.92 ± 0.07	2.0 ± 0.06				23.91/27
54440.01	Powerlaw	1.86 ± 0.05	1.51 ± 0.03				62.00/53
54449.38	Powerlaw	1.95 ± 0.1	1.29 ± 0.01				12.08/15
54457.35	Powerlaw	2.2 ± 0.08	2.24 ± 0.07				17.17/28
54462.28	Powerlaw	2.16 ± 0.13	1.58 ± 0.08				3.67/10
54469.18	Powerlaw	1.98 ± 0.08	1.82 ± 0.05				18.66/25
54479.35	Bknpowerlaw	2.49 ± 0.14	1.78 ± 0.09	1.45 ± 0.26	1.76 ± 0.13	1.29 ± 0.10	61.12/39
54786.73	Bknpowerlaw	2.35 ± 0.28	0.34 ± 0.02	1.04 ± 0.27	1.76 ± 0.09	1.17 ± 0.11	33.92/36
55036.13	Powerlaw	1.7 ± 0.06	2.45 ± 0.07				37.12/45
55039.34	Powerlaw	2.03 ± 0.07	1.91 ± 0.06				56.10/33
55043.35	Powerlaw	1.84 ± 0.05	2.82 ± 0.06				59.47/50
55045.03	Bknpowerlaw	2.2 ± 0.09	1.45 ± 0.17	1.53 ± 0.21	0.58 ± 0.05	38.42/38	
55048.03	Powerlaw	1.95 ± 0.06	1.91 ± 0.04				29.13/40
55051.52	Powerlaw	2.1 ± 0.06	2.0 ± 0.04				33.14/36
55497.90	Powerlaw	1.84 ± 0.62	2.0 ± 0.06				16.48/22

Time MJD	Model	Γ_1	$Flux_1$ $10^{-11}\ ergs\,cm^{-2}s^{-1}$	BreakE keV	Γ_2	$Flux_2$ $10^{-11}\ ergs\,cm^{-2}s^{-1}$	χ^2
55498.09	Powerlaw	1.9 ± 0.08	1.41 ± 0.06				8.44/13
55499.10	Bknpowerlaw	2.15 ± 0.14	1.02 ± 0.05	1.67 ± 0.61	1.88 ± 0.18	0.81 ± 0.11	27.09/32
55500.57	Powerlaw	1.92 ± 0.07	1.95 ± 0.06				28.60/37
55501.31	Powerlaw	2.1 ± 0.06	2.09 ± 0.06				40.51/37
55502.18	Powerlaw	1.98 ± 0.07	1.62 ± 0.05				57.59/33
55503.38	Powerlaw	2.15 ± 0.06	1.66 ± 0.03				31.60/36
55504.86	Powerlaw	1.94 ± 0.07	1.66 ± 0.03				22.34/29
55505.87	Powerlaw	1.98 ± 0.07	2.51 ± 0.05				49.95/44
55506.87	Powerlaw	1.91 ± 0.06	2.04 ± 0.06				40.54/35
55507.87	Powerlaw	2.07 ± 0.25	1.51 ± 0.11				3.58/5
55508.88	Powerlaw	2.03 ± 0.08	1.55 ± 0.05				18.89/22
55509.81	Powerlaw	1.99 ± 0.07	2.0 ± 0.06				26.52/34
55510.88	Powerlaw	1.97 ± 0.08	2.51 ± 0.08				29.75/26
55511.54	Powerlaw	2.05 ± 0.06	2.69 ± 0.05				64.53/52
55512.08	Powerlaw	2.03 ± 0.08	2.4 ± 0.07				34.70/32
55513.55	Powerlaw	2.0 ± 0.07	2.69 ± 0.08				33.18/32
55514.22	Powerlaw	1.92 ± 0.05	2.75 ± 0.11				57.41/51
55515.03	Powerlaw	1.83 ± 0.14	1.66 ± 0.1				7.97/9
55516.57	Powerlaw	1.76 ± 0.06	2.57 ± 0.08				53.10/43
55517.50	Powerlaw	1.96 ± 0.08	2.04 ± 0.06				30.86/26
55518.30	Powerlaw	1.99 ± 0.07	2.14 ± 0.06				39.05/35
55519.66	Powerlaw	1.97 ± 0.08	1.45 ± 0.06				28.07/25
55523.18	Powerlaw	2.27 ± 0.05	3.39 ± 0.07				49.40/53
55524.79	Powerlaw	2.17 ± 0.05	3.02 ± 0.06				65.07/51

Time MJD	Model	Γ_1	$Flux_1$ $10^{-11}\ ergs\,cm^{-2}s^{-1}$	BreakE keV	Γ_2	$Flux_2$ $10^{-11}\ ergs\,cm^{-2}s^{-1}$	χ^2
55525.79	Bknpowerlaw	2.31 ± 0.07	2.51 ± 0.3	1.46 ± 0.32	1.24 ± 0.35	0.66 ± 0.13	44.06/36
55526.26	Powerlaw	2.11 ± 0.05	2.69 ± 0.05				50.42/50
55527.74	Bknpowerlaw	2.25 ± 0.14	1.12 ± 0.22	2.48 ± 0.61	1.69 ± 0.14	1.38 ± 0.19	58.25/58
55528.14	Bknpowerlaw	2.25 ± 0.08	1.95 ± 0.19	2.15 ± 0.22	1.75 ± 0.28	0.56 ± 0.09	31.74/28
55529.14	Powerlaw	2.13 ± 0.05	2.09 ± 0.04				48.72/43
55530.49	Powerlaw	2.09 ± 0.06	2.45 ± 0.07				38.82/42
55749.00	Powerlaw	2.16 ± 0.05	3.63 ± 0.07				51.06/46
55780.24	Powerlaw	2.06 ± 0.06	2.75 ± 0.08				34.36/36
55808.00	Powerlaw	2.02 ± 0.08	2.51 ± 0.08				11.01/22
55837.76	Powerlaw	2.0 ± 0.11	1.45 ± 0.04				18.52/17
55841.05	Powerlaw	1.96 ± 0.07	2.75 ± 0.08				40.73/31
55870.20	Powerlaw	2.03 ± 0.08	2.24 ± 0.07				15.98/25
55899.64	Powerlaw	1.84 ± 0.25	1.38 ± 0.1				5.50/8
55902.05	Powerlaw	1.73 ± 0.14	1.26 ± 0.09				19.68/22
55923.37	Powerlaw	2.14 ± 0.08	2.29 ± 0.07				7.69/10
55928.04	Powerlaw	2.0 ± 0.13	1.55 ± 0.08				20.20/16
55956.66	Powerlaw	1.98 ± 0.1	1.48 ± 0.06				3.56/8
55989.34	Powerlaw	2.0 ± 0.12	1.1 ± 0.05				27.57/32
56305.46	Powerlaw	1.85 ± 0.07	1.51 ± 0.05				19.75/26
56306.32	Powerlaw	2.01 ± 0.08	1.58 ± 0.05				42.96/34
56307.39	Powerlaw	1.97 ± 0.06	1.45 ± 0.04				21.04/21
56338.32	Powerlaw	1.63 ± 0.2	1.1 ± 0.04				24.22/22
56338.78	Powerlaw	2.08 ± 0.09	0.98 ± 0.03				8.20/15
56353.67	Powerlaw	2.13 ± 0.1	1.48 ± 0.04				23.44/21

Time MJD	Model	Γ_1	Flux$_1$ $10^{-11}\ ergs\,cm^{-2}s^{-1}$	BreakE keV	Γ_2	Flux$_2$ $10^{-11}\ ergs\,cm^{-2}s^{-1}$	χ^2
56356.61	Bknpowerlaw	2.44 ± 0.11	1.35 ± 0.09	2.45 ± 0.42	1.54 ± 0.51	0.35 ± 0.07	21.20/22
56485.29	Powerlaw	1.93 ± 0.06	2.69 ± 0.08				24.87/42
56489.61	Powerlaw	2.05 ± 0.05	2.34 ± 0.05				55.28/54
56491.68	Powerlaw	1.99 ± 0.06	2.29 ± 0.05				27.92/35
56492.10	Bknpowerlaw	2.28 ± 0.18	0.91 ± 0.15	1.37 ± 0.21	1.68 ± 0.11	1.58 ± 0.13	34.57/34
56492.68	Powerlaw	1.84 ± 0.06	2.34 ± 0.05				51.44/43
56524.00	Powerlaw	2.12 ± 0.05	2.45 ± 0.05				49.62/54
56524.80	Powerlaw	2.17 ± 0.06	1.74 ± 0.03				30.41/40
56525.27	Powerlaw	2.25 ± 0.05	2.45 ± 0.05				63.85/55
56534.67	Powerlaw	1.71 ± 0.16	2.88 ± 0.06				46.56/34
56541.01	Powerlaw	2.04 ± 0.06	2.34 ± 0.07				41.82/35
56548.03	Powerlaw	2.13 ± 0.09	4.57 ± 0.23				29.88/25
56555.09	Powerlaw	1.67 ± 0.08	1.82 ± 0.07				35.09/26
56562.18	Powerlaw	1.73 ± 0.18	1.82 ± 0.15				11.90/7
56567.98	Powerlaw	2.27 ± 0.13	2.14 ± 0.11				16.08/11
57001.71	Powerlaw	2.07 ± 0.06	2.34 ± 0.05				47.17/44
57003.30	Powerlaw	2.08 ± 0.07	2.40 ± 0.07				44.02/27
57236.79	Powerlaw	1.87 ± 0.09	1.32 ± 0.05				14.35/19
57239.72	Powerlaw	2.09 ± 0.12	1.07 ± 0.04				23.18/15
57245.05	Powerlaw	2.31 ± 0.06	2.45 ± 0.07				43.39/38
57251.57	Powerlaw	1.86 ± 0.15	1.35 ± 0.07				7.89/6
57254.10	Powerlaw	1.81 ± 0.09	1.48 ± 0.06				21.59/17
57257.62	Bknpowerlaw	2.56 ± 0.25	0.66 ± 0.01	2.11 ± 0.36	1.68 ± 0.39	0.52 ± 0.01	25.07/21
57260.02	Powerlaw	2.23 ± 0.07	1.82 ± 0.05				37.71/29

Time MJD	Model	Γ_1	Flux$_1$ $10^{-11}\ ergs\,cm^{-2}s^{-1}$	BreakE keV	Γ_2	Flux$_2$ $10^{-11}\ ergs\,cm^{-2}s^{-1}$	χ^2
57263.81	Powerlaw	1.86 ± 0.09	1.41 ± 0.06				10.55/18
57275.37	Powerlaw	1.93 ± 0.1	1.82 ± 0.07				12.15/15
57282.75	Powerlaw	2.08 ± 0.08	2.24 ± 0.07				21.50/22
57289.88	Powerlaw	2.08 ± 0.09	2.82 ± 0.11				16.18/20
57295.00	Powerlaw	2.16 ± 0.07	3.16 ± 0.09				37.31/37
57303.05	Powerlaw	2.22 ± 0.06	3.39 ± 0.07				40.06/42
57310.90	Powerlaw	2.21 ± 0.09	2.4 ± 0.07				23.21/24
57317.22	Powerlaw	2.45 ± 0.07	2.51 ± 0.08				33.67/29
57326.70	Powerlaw	2.08 ± 0.47	1.86 ± 0.07				28.53/26
57331.05	Powerlaw	2.02 ± 0.31	1.45 ± 0.03				33.51/22
57338.21	Powerlaw	2.46 ± 0.1	1.62 ± 0.06				25.63/19
57345.41	Powerlaw	1.9 ± 0.1	1.51 ± 0.06				14.01/15
57352.64	Powerlaw	1.92 ± 0.09	2.24 ± 0.09				25.39/23
57359.16	Powerlaw	2.0 ± 0.24	2.63 ± 0.16				3.84/3
57364.74	Powerlaw	1.92 ± 0.15	2.09 ± 0.10				14.81/10
57366.62	Powerlaw	2.05 ± 0.23	1.62 ± 0.19				66.22/66
57371.54	Powerlaw	2.45 ± 0.2	0.74 ± 0.06				40.91/51
57373.72	Powerlaw	2.1 ± 0.13	1.17 ± 0.06				66.49/77
57380.30	Powerlaw	2.2 ± 0.09	1.62 ± 0.05				15.36/20
58304.46	Powerlaw	2.17 ± 0.1	1.74 ± 0.07				23.05/15
58311.04	Powerlaw	2.06 ± 0.17	1.35 ± 0.08				7.55/6
58318.14	Powerlaw	2.22 ± 0.19	1.62 ± 0.1				9.64/8
58325.66	Powerlaw	2.08 ± 0.15	1.45 ± 0.09				2.11/6
58332.69	Powerlaw	2.35 ± 0.14	1.74 ± 0.09				12.49/8
58339.53	Powerlaw	2.06 ± 0.18	0.6 ± 0.05				44.41/101

Time MJD	Model	Γ_1	Flux$_1$ $10^{-11}\ ergs\,cm^{-2}s^{-1}$	BreakE keV	Γ_2	Flux$_2$ $10^{-11}\ ergs\,cm^{-2}s^{-1}$	χ^2
58346.25	Powerlaw	2.29 ± 0.18	0.89 ± 0.05				2.81/2
58353.03	Powerlaw	1.95 ± 0.35	1.1 ± 0.05				18.49/16
58360.12	Powerlaw	2.19 ± 0.15	1.35 ± 0.08				32.81/54
58367.91	Powerlaw	2.2 ± 0.21	0.56 ± 0.04				5.31/8
58374.06	Powerlaw	2.11 ± 0.2	1.66 ± 0.1				3.67/3
58381.57	Powerlaw	2.55 ± 0.39	0.42 ± 0.05				16.43/15
58388.02	Powerlaw	2.2 ± 0.22	0.68 ± 0.07				65.75/62
58395.60	Powerlaw	2.13 ± 0.31	1.02 ± 0.08				64.65/60
58402.16	Powerlaw	2.25 ± 0.22	0.49 ± 0.03				34.25/30
58409.26	Powerlaw	2.56 ± 0.19	0.98 ± 0.08				44.23/43
58416.03	Powerlaw	2.38 ± 0.24	0.42 ± 0.05				56.71/55
58423.01	Powerlaw	2.02 ± 0.24	0.72 ± 0.07				84.45/70
58430.25	Powerlaw	2.51 ± 0.22	0.41 ± 0.04				68.13/61
58437.55	Powerlaw	2.22 ± 0.24	0.51 ± 0.05				34.25/30
58444.01	Powerlaw	1.95 ± 0.22	0.62 ± 0.06				38.13/31
58451.1	Powerlaw	2.06 ± 0.15	0.78 ± 0.06				74.45/69
58458.09	Powerlaw	2.23 ± 0.23	0.71 ± 0.04				37.27/34
58465.06	Powerlaw	2.29 ± 0.19	0.72 ± 0.05				64.55/58
58759.28	Powerlaw	2.2 ± 0.16	1.07 ± 0.05				68.13/61
58765.13	Powerlaw	2.2 ± 0.14	1.02 ± 0.04				14.25/10
58774.49	Powerlaw	2.39 ± 0.12	1.23 ± 0.06				3.67/3
58831.67	Powerlaw	2.04 ± 0.09	2.63 ± 0.08				6.97/7
58838.31	Powerlaw	2.16 ± 0.1	2.14 ± 0.04				5.31/8
59051.70	Powerlaw	2.36 ± 0.12	2.45 ± 0.1				42.91/54
59059.61	Powerlaw	2.11 ± 0.19	0.83 ± 0.05				18.49/16

Time MJD	Model	Γ_1	Flux$_1$ $10^{-11}\ ergs\,cm^{-2}s^{-1}$	BreakE keV	Γ_2	Flux$_2$ $10^{-11}\ ergs\,cm^{-2}s^{-1}$	χ^2
59065.31	Powerlaw	2.08 ± 0.18	1.78 ± 0.05				74.41/91
59402.47	Powerlaw	2.05 ± 0.32	0.89 ± 0.12				13.03/15
59403.33	Powerlaw	2.04 ± 0.16	1.26 ± 0.11				2.41/5
59405.12	Powerlaw	2.29 ± 0.13	1.35 ± 0.07				12.88/16
59406.66	Powerlaw	2.03 ± 0.15	1.74 ± 0.07				26.71/19
59476.01	Powerlaw	2.14 ± 0.19	1.12 ± 0.06				11.31/14
59644.70	Powerlaw	2.42 ± 0.15	1.38 ± 0.06				68.87/61
59651.20	Powerlaw	2.18 ± 0.15	1.7 ± 0.07				3.56/8
59786.30	Powerlaw	2.0 ± 0.28	2.04 ± 0.16				87.15/95
59792.26	Powerlaw	2.48 ± 0.16	2.19 ± 0.09				76.23/73
59818.85	Powerlaw	2.23 ± 0.31	0.56 ± 0.07				14.53/13
59833.64	Powerlaw	2.56 ± 0.3	0.4 ± 0.06				12.56/15
59846.69	Powerlaw	2.28 ± 0.63	1.45 ± 0.13				36.41/32
59882.96	Powerlaw	2.48 ± 0.18	1.05 ± 0.08				39.52/35
59885.15	Powerlaw	2.08 ± 0.13	1.1 ± 0.07				16.13/20
59936.42	Powerlaw	1.9 ± 0.15	1.82 ± 0.07				21.35/21
59937.76	Powerlaw	2.06 ± 0.31	2.19 ± 0.13				32.81/34
59957.16	Powerlaw	2.32 ± 0.1	2.95 ± 0.12				28.49/26
59966.23	Powerlaw	2.0 ± 0.21	1.74 ± 0.12				43.05/55
59968.87	Powerlaw	2.47 ± 0.33	1.91 ± 0.13				56.49/67
59976.37	Powerlaw	2.25 ± 0.23	0.6 ± 0.07				5.72/7
59981.0	Powerlaw	2.27 ± 0.16	1.7 ± 0.07				2.36/4
59986.43	Powerlaw	2.32 ± 0.13	1.38 ± 0.08				65.13/71
59988.22	Powerlaw	2.3 ± 0.21	1.26 ± 0.06				42.74/38
59995.50	Powerlaw	2.0 ± 0.2	2.09 ± 0.13				49.15/44

Appendix: UVOT Parameters

.1 Optical Band

.2 UV band

Table 9: UVOT optical band fluxes and spectral index

Time MJD	α_{opt}	V $10^{-11}\ ergs\,cm^{-2}s^{-1}$	B $10^{-11}\ ergs\,cm^{-2}s^{-1}$	U $10^{-11}\ ergs\,cm^{-2}s^{-1}$
54301.950	0.67 ± 0.13	1.90 ± 0.02	1.90 ± 0.02	2.19 ± 0.02
54408.173	1.02 ± 0.17	1.79 ± 0.03	1.68 ± 0.02	1.77 ± 0.03
54415.137	0.77 ± 0.16	1.65 ± 0.03	1.64 ± 0.02	1.82 ± 0.02
54429.802	0.75 ± 0.16	1.66 ± 0.03	1.72 ± 0.02	1.86 ± 0.02
54435.259	0.74 ± 0.16	1.66 ± 0.03	1.69 ± 0.02	1.86 ± 0.02
54440.188	0.80 ± 0.13	1.69 ± 0.02	1.66 ± 0.02	1.84 ± 0.02
54449.425	0.90 ± 0.16	1.74 ± 0.03	1.75 ± 0.02	1.82 ± 0.02
54457.421	0.71 ± 0.17	1.71 ± 0.03	1.80 ± 0.02	1.94 ± 0.03
54469.231	0.74 ± 0.16	1.74 ± 0.03	1.77 ± 0.02	1.95 ± 0.03
54479.398	0.73 ± 0.16	1.89 ± 0.03	1.86 ± 0.03	2.13 ± 0.03
54786.783	0.86 ± 0.13	1.78 ± 0.02	1.76 ± 0.02	1.89 ± 0.02
55036.203	0.63 ± 0.14	2.14 ± 0.03	2.08 ± 0.02	2.51 ± 0.03
55039.451	0.76 ± 0.14	2.14 ± 0.03	2.02 ± 0.02	2.37 ± 0.03
55042.464	0.53 ± 0.15	2.02 ± 0.03	2.07 ± 0.02	2.48 ± 0.03
55045.105	0.65 ± 0.14	1.97 ± 0.03	2.02 ± 0.02	2.29 ± 0.03
55048.084	0.49 ± 0.14	1.86 ± 0.03	2.23 ± 0.02	2.33 ± 0.03
55051.628	0.65 ± 0.15	1.88 ± 0.03	2.09 ± 0.02	2.19 ± 0.03
55497.949	0.55 ± 0.14	2.09 ± 0.03	2.24 ± 0.03	2.54 ± 0.03
55498.144	0.54 ± 0.14	1.94 ± 0.03	2.04 ± 0.02	2.37 ± 0.03
55499.147	0.62 ± 0.14	2.07 ± 0.03	2.08 ± 0.03	2.45 ± 0.03
55502.227	0.56 ± 0.14	1.95 ± 0.03	2.05 ± 0.02	2.36 ± 0.03
55507.919	1.24 ± 0.16	1.86 ± 0.03	2.18 ± 0.02	1.67 ± 0.02
55512.126	0.59 ± 0.14	2.00 ± 0.03	2.16 ± 0.03	2.38 ± 0.03
55519.800	0.52 ± 0.12	1.91 ± 0.02	2.03 ± 0.02	2.35 ± 0.03
55523.231	0.50 ± 0.15	1.91 ± 0.03	2.22 ± 0.03	2.37 ± 0.03
55524.844	0.49 ± 0.15	1.96 ± 0.03	2.15 ± 0.02	2.44 ± 0.03
55525.882	0.50 ± 0.14	2.03 ± 0.03	2.03 ± 0.02	2.53 ± 0.03
55526.315	0.37 ± 0.12	1.91 ± 0.02	1.95 ± 0.02	2.51 ± 0.03
55749.014	0.43 ± 0.19	2.03 ± 0.04	2.06 ± 0.03	2.60 ± 0.04
55780.654	0.49 ± 0.16	2.00 ± 0.04	2.24 ± 0.03	2.51 ± 0.03

Time MJD	α_{opt}	V $10^{-11}\ ergs\,cm^{-2}s^{-1}$	B $10^{-11}\ ergs\,cm^{-2}s^{-1}$	U $10^{-11}\ ergs\,cm^{-2}s^{-1}$
55808.018	0.43 ± 0.17	1.94 ± 0.04	2.08 ± 0.03	2.49 ± 0.03
55837.832	0.49 ± 0.17	1.93 ± 0.04	2.07 ± 0.03	2.41 ± 0.03
55841.528	0.60 ± 0.19	2.17 ± 0.04	2.16 ± 0.03	2.57 ± 0.04
55870.878	0.60 ± 0.21	1.82 ± 0.04	2.09 ± 0.03	2.16 ± 0.04
55902.056	0.97 ± 0.28	1.82 ± 0.06	1.65 ± 0.04	1.84 ± 0.04
55923.411	0.74 ± 0.18	1.63 ± 0.03	1.68 ± 0.02	1.83 ± 0.03
55928.051	0.62 ± 0.24	1.65 ± 0.05	1.76 ± 0.03	1.94 ± 0.03
55956.672	0.75 ± 0.20	1.93 ± 0.04	1.86 ± 0.03	2.15 ± 0.03
55989.354	0.90 ± 0.20	1.62 ± 0.04	1.53 ± 0.03	1.70 ± 0.03
56305.831	0.75 ± 0.14	1.72 ± 0.03	1.75 ± 0.02	1.92 ± 0.02
56306.667	0.83 ± 0.15	1.84 ± 0.03	1.66 ± 0.02	1.98 ± 0.03
56307.664	0.75 ± 0.15	1.78 ± 0.03	1.76 ± 0.02	1.98 ± 0.02
56338.404	0.69 ± 0.14	1.66 ± 0.02	1.75 ± 0.02	1.90 ± 0.02
56338.866	0.74 ± 0.15	1.64 ± 0.03	1.65 ± 0.02	1.84 ± 0.02
56353.682	0.57 ± 0.19	1.87 ± 0.04	2.19 ± 0.03	2.25 ± 0.03
56356.624	0.74 ± 0.18	1.68 ± 0.04	1.67 ± 0.02	1.88 ± 0.02
56489.621	0.65 ± 0.19	2.29 ± 0.05	2.35 ± 0.04	2.66 ± 0.04
56491.763	0.74 ± 0.14	2.15 ± 0.03	2.07 ± 0.02	2.41 ± 0.03
56492.169	0.52 ± 0.13	2.2 ± 0.03	2.49 ± 0.03	2.71 ± 0.03
56492.767	0.62 ± 0.13	2.18 ± 0.03	2.34 ± 0.03	2.57 ± 0.03
56524.075	0.47 ± 0.14	1.9 ± 0.03	2.01 ± 0.02	2.39 ± 0.03
56524.873	0.62 ± 0.14	2.05 ± 0.03	2.1 ± 0.02	2.41 ± 0.03
56525.439	0.39 ± 0.14	1.87 ± 0.03	2.15 ± 0.02	2.44 ± 0.03
56534.686	0.56 ± 0.14	2.18 ± 0.03	2.28 ± 0.03	2.63 ± 0.03
56541.158	0.37 ± 0.15	2.07 ± 0.03	2.29 ± 0.03	2.72 ± 0.03
56548.071	0.52 ± 0.16	2.29 ± 0.04	2.45 ± 0.03	2.82 ± 0.04

Time MJD	α_{opt}	V $10^{-11}\ ergs\,cm^{-2}s^{-1}$	B $10^{-11}\ ergs\,cm^{-2}s^{-1}$	U $10^{-11}\ ergs\,cm^{-2}s^{-1}$
56555.134	0.43 ± 0.14	2.32 ± 0.04	2.47 ± 0.03	2.96 ± 0.04
56562.354	0.51 ± 0.17	2.18 ± 0.04	2.28 ± 0.03	2.69 ± 0.04
56567.986	0.41 ± 0.20	2.09 ± 0.05	2.25 ± 0.04	2.71 ± 0.04
57001.752	0.62 ± 0.15	2.23 ± 0.04	2.26 ± 0.03	2.63 ± 0.03
57003.351	0.53 ± 0.15	2.01 ± 0.03	2.08 ± 0.02	2.47 ± 0.03
57236.838	0.73 ± 0.16	1.88 ± 0.03	1.96 ± 0.02	2.12 ± 0.03
57239.764	0.73 ± 0.16	1.87 ± 0.03	1.87 ± 0.02	2.11 ± 0.03
57245.092	0.47 ± 0.16	1.87 ± 0.03	1.96 ± 0.03	2.35 ± 0.03
57251.608	0.57 ± 0.19	1.77 ± 0.04	1.89 ± 0.03	2.13 ± 0.03
57254.146	0.70 ± 0.17	1.87 ± 0.03	1.95 ± 0.03	2.13 ± 0.03
57257.669	0.80 ± 0.16	1.93 ± 0.03	1.90 ± 0.02	2.10 ± 0.03
57260.092	0.72 ± 0.15	1.94 ± 0.03	1.93 ± 0.02	2.20 ± 0.03
57263.853	0.83 ± 0.16	1.88 ± 0.03	1.83 ± 0.02	2.03 ± 0.03
57275.414	0.62 ± 0.19	1.82 ± 0.04	1.89 ± 0.03	2.15 ± 0.03
57282.832	0.67 ± 0.18	2.00 ± 0.04	2.08 ± 0.03	2.31 ± 0.03
57289.947	0.38 ± 0.20	1.86 ± 0.04	2.09 ± 0.03	2.43 ± 0.03
57295.042	0.34 ± 0.16	2.05 ± 0.04	2.24 ± 0.03	2.74 ± 0.04
57303.350	0.42 ± 0.16	2.14 ± 0.04	2.32 ± 0.03	2.76 ± 0.04
57310.937	0.43 ± 0.16	2.19 ± 0.04	2.26 ± 0.03	2.80 ± 0.04
57317.291	0.38 ± 0.16	2.11 ± 0.04	2.25 ± 0.03	2.77 ± 0.04
57331.448	0.55 ± 0.15	1.95 ± 0.03	2.12 ± 0.03	2.37 ± 0.03
57338.282	0.47 ± 0.16	2.08 ± 0.04	2.14 ± 0.03	2.62 ± 0.03
57345.446	0.55 ± 0.17	1.90 ± 0.04	2.10 ± 0.03	2.32 ± 0.03
57352.690	0.78 ± 0.16	2.07 ± 0.04	2.05 ± 0.03	2.28 ± 0.03
57359.163	0.49 ± 0.26	1.90 ± 0.06	1.92 ± 0.04	2.37 ± 0.05
57364.748	0.82 ± 0.24	2.09 ± 0.07	2.11 ± 0.03	2.26 ± 0.03
57371.548	0.83 ± 0.39	1.93 ± 0.05	2.00 ± 0.03	2.08 ± 0.10
57380.416	0.70 ± 0.17	1.89 ± 0.03	2.03 ± 0.03	2.16 ± 0.03
58759.302	0.60 ± 0.18	1.81 ± 0.04	1.94 ± 0.03	2.16 ± 0.03
58765.143	0.73 ± 0.18	1.84 ± 0.04	1.87 ± 0.03	2.07 ± 0.03

Time MJD	α_{opt}	V $10^{-11}\ ergs\,cm^{-2}s^{-1}$	B $10^{-11}\ ergs\,cm^{-2}s^{-1}$	U $10^{-11}\ ergs\,cm^{-2}s^{-1}$
58774.508	0.79 ± 0.18	1.99 ± 0.04	1.94 ± 0.03	2.18 ± 0.03
58831.707	0.42 ± 0.16	2.14 ± 0.04	2.34 ± 0.03	2.76 ± 0.04
58838.320	0.27 ± 0.20	1.75 ± 0.04	2.05 ± 0.03	2.40 ± 0.04
59051.708	0.3 ± 0.23	1.96 ± 0.05	2.31 ± 0.04	2.65 ± 0.05
59059.617	0.69 ± 0.23	2.27 ± 0.06	2.42 ± 0.04	2.60 ± 0.05
59065.325	0.65 ± 0.23	2.00 ± 0.05	1.94 ± 0.04	2.33 ± 0.04
59644.811	0.67 ± 0.17	1.94 ± 0.04	1.90 ± 0.03	2.25 ± 0.03
59651.343	0.46 ± 0.18	1.84 ± 0.04	1.99 ± 0.03	2.34 ± 0.03
59786.310	0.46 ± 0.29	1.80 ± 0.06	1.81 ± 0.04	2.28 ± 0.05
59792.276	0.72 ± 0.20	1.91 ± 0.04	1.94 ± 0.03	2.16 ± 0.04
59818.861	0.78 ± 0.31	1.83 ± 0.06	1.78 ± 0.05	2.01 ± 0.05
59833.649	0.94 ± 0.34	1.62 ± 0.06	1.74 ± 0.05	1.66 ± 0.04
59846.704	1.01 ± 0.27	2.05 ± 0.06	1.83 ± 0.04	2.04 ± 0.05
59882.971	0.07 ± 0.27	1.69 ± 0.05	1.95 ± 0.04	2.53 ± 0.05
59885.490	0.34 ± 0.20	1.75 ± 0.04	2.11 ± 0.03	2.34 ± 0.04
59936.702	0.56 ± 0.19	2.05 ± 0.04	2.17 ± 0.03	2.49 ± 0.04
59937.765	0.76 ± 0.28	2.25 ± 0.07	2.12 ± 0.05	2.50 ± 0.06
59957.174	0.53 ± 0.21	2.10 ± 0.05	2.26 ± 0.04	2.58 ± 0.04
59966.240	0.6 ± 0.24	1.94 ± 0.05	2.12 ± 0.04	2.31 ± 0.04
59968.883	0.46 ± 0.30	1.75 ± 0.06	2.06 ± 0.05	2.21 ± 0.05
59976.381	0.98 ± 0.27	2.28 ± 0.07	1.86 ± 0.04	2.30 ± 0.05
59986.446	0.47 ± 0.19	1.87 ± 0.04	1.91 ± 0.03	2.35 ± 0.04
59981.081	0.72 ± 0.19	2.06 ± 0.04	2.07 ± 0.03	2.32 ± 0.03
59988.239	0.64 ± 0.18	1.89 ± 0.04	1.96 ± 0.03	2.21 ± 0.03

Table 10: UVOT ultraviolet bands fluxes and spectral index

Time MJD	α_{UV}	W_1 $10^{-11}\ ergs\,cm^{-2}s^{-1}$	M_2 $10^{-11}\ ergs\,cm^{-2}s^{-1}$	W_2 $10^{-11}\ ergs\,cm^{-2}s^{-1}$
54301.950	-0.26 ± 0.19	2.03 ± 0.02	2.59 ± 0.03	2.75 ± 0.03
54408.173	-0.24 ± 0.27	1.60 ± 0.02	1.95 ± 0.04	2.16 ± 0.03
54415.137	-0.34 ± 0.24	1.73 ± 0.02	2.18 ± 0.04	2.39 ± 0.03
54429.802	-0.25 ± 0.25	1.63 ± 0.02	2.0 ± 0.03	2.21 ± 0.03
54435.259	-0.4 ± 0.25	1.66 ± 0.02	2.2 ± 0.04	2.33 ± 0.03
54440.188	-0.09 ± 0.2	1.73 ± 0.02	2.24 ± 0.03	2.25 ± 0.02
54449.425	-0.35 ± 0.24	1.76 ± 0.02	2.19 ± 0.04	2.44 ± 0.03
54457.421	-0.51 ± 0.25	1.81 ± 0.03	2.40 ± 0.04	2.60 ± 0.03
54469.231	-0.35 ± 0.24	1.87 ± 0.03	2.46 ± 0.04	2.59 ± 0.03
54479.398	-0.58 ± 0.23	2.08 ± 0.03	2.71 ± 0.04	3.05 ± 0.03
54786.783	-0.19 ± 0.2	1.64 ± 0.02	1.97 ± 0.03	2.18 ± 0.02
55036.203	-0.37 ± 0.21	2.26 ± 0.03	2.87 ± 0.04	3.16 ± 0.03
55039.451	-0.25 ± 0.22	2.15 ± 0.03	2.63 ± 0.04	2.91 ± 0.03
55042.464	-0.31 ± 0.22	2.2 ± 0.03	2.82 ± 0.04	3.02 ± 0.03
55045.105	-0.33 ± 0.21	2.22 ± 0.03	2.76 ± 0.04	3.07 ± 0.03
55048.084	-0.12 ± 0.21	2.15 ± 0.03	2.67 ± 0.04	2.83 ± 0.03
55051.628	-0.15 ± 0.23	1.94 ± 0.02	2.51 ± 0.04	2.56 ± 0.03
55497.949	-0.07 ± 0.21	2.28 ± 0.03	2.79 ± 0.05	2.96 ± 0.03
55498.144	0.26 ± 0.22	2.05 ± 0.03	2.47 ± 0.04	2.45 ± 0.03
55499.147	-0.26 ± 0.21	2.22 ± 0.03	2.90 ± 0.04	3.01 ± 0.03
55502.227	-0.14 ± 0.21	2.18 ± 0.03	2.72 ± 0.04	2.88 ± 0.03
55507.919	0.19 ± 0.24	1.95 ± 0.03	2.13 ± 0.03	2.38 ± 0.03
55512.126	-0.49 ± 0.22	2.2 ± 0.03	2.75 ± 0.04	3.16 ± 0.03
55519.800	-0.37 ± 0.22	2.23 ± 0.03	2.9 ± 0.04	3.11 ± 0.03
55523.231	-0.44 ± 0.22	2.29 ± 0.03	3.11 ± 0.04	3.24 ± 0.04
55524.844	-0.39 ± 0.22	2.32 ± 0.03	3.0 ± 0.04	3.26 ± 0.04
55525.882	-0.34 ± 0.21	2.54 ± 0.03	3.3 ± 0.05	3.51 ± 0.04
55526.315	-0.1 ± 0.21	2.33 ± 0.03	2.95 ± 0.04	3.04 ± 0.03
55749.014	-0.46 ± 0.24	2.35 ± 0.03	3.02 ± 0.05	3.35 ± 0.04
55780.654	-0.19 ± 0.25	2.56 ± 0.04	3.08 ± 0.05	3.42 ± 0.04
55808.018	-0.46 ± 0.28	2.31 ± 0.04	2.94 ± 0.06	3.29 ± 0.04
55837.832	-0.07 ± 0.24	2.36 ± 0.03	2.76 ± 0.05	3.06 ± 0.03
55841.528	-0.23 ± 0.25	2.50 ± 0.04	3.19 ± 0.06	3.37 ± 0.04
55870.878	-0.62 ± 0.31	1.99 ± 0.04	2.67 ± 0.03	2.95 ± 0.04

Time MJD	α_{UV}	W_1 $10^{-11}\ ergs\,cm^{-2}s^{-1}$	M_2 $10^{-11}\ ergs\,cm^{-2}s^{-1}$	W_2 $10^{-11}\ ergs\,cm^{-2}s^{-1}$
55524.844	-0.39 ± 0.22	2.32 ± 0.03	3.0 ± 0.04	3.26 ± 0.04
55525.882	-0.34 ± 0.21	2.54 ± 0.03	3.3 ± 0.05	3.51 ± 0.04
55526.315	-0.1 ± 0.21	2.33 ± 0.03	2.95 ± 0.04	3.04 ± 0.03
55749.014	-0.46 ± 0.24	2.35 ± 0.03	3.02 ± 0.05	3.35 ± 0.04
55780.654	-0.19 ± 0.25	2.56 ± 0.04	3.08 ± 0.05	3.42 ± 0.04
55808.018	-0.46 ± 0.28	2.31 ± 0.04	2.94 ± 0.06	3.29 ± 0.04
55837.832	-0.07 ± 0.24	2.36 ± 0.03	2.76 ± 0.05	3.06 ± 0.03
55841.528	-0.23 ± 0.25	2.50 ± 0.04	3.19 ± 0.06	3.37 ± 0.04
55870.878	-0.62 ± 0.31	1.99 ± 0.04	2.67 ± 0.03	2.95 ± 0.04
55902.056	-0.09 ± 0.43	1.80 ± 0.04	2.24 ± 0.03	2.34 ± 0.05
55923.411	-0.33 ± 0.27	1.74 ± 0.03	2.28 ± 0.04	2.41 ± 0.03
55928.051	-0.53 ± 0.28	1.79 ± 0.03	2.59 ± 0.07	2.59 ± 0.04
55956.672	0.15 ± 0.28	1.93 ± 0.03	2.24 ± 0.03	2.37 ± 0.04
55989.354	0.2 ± 0.31	1.57 ± 0.03	1.82 ± 0.04	1.9 ± 0.03
56305.831	-0.21 ± 0.22	1.77 ± 0.02	2.14 ± 0.03	2.37 ± 0.03
56306.667	-0.28 ± 0.24	1.80 ± 0.02	2.36 ± 0.04	2.46 ± 0.03
56307.664	-0.31 ± 0.22	1.81 ± 0.02	2.39 ± 0.03	2.49 ± 0.03
56338.404	0.01 ± 0.22	1.72 ± 0.02	2.11 ± 0.03	2.19 ± 0.02
56338.866	-0.15 ± 0.23	1.63 ± 0.02	1.99 ± 0.03	2.15 ± 0.02
56353.682	-0.35 ± 0.25	1.89 ± 0.03	2.34 ± 0.05	2.63 ± 0.03
56356.624	-0.54 ± 0.24	1.74 ± 0.02	2.29 ± 0.04	2.53 ± 0.03
56489.621	-0.02 ± 0.25	2.56 ± 0.04	3.16 ± 0.06	3.29 ± 0.03
56491.763	-0.52 ± 0.21	2.25 ± 0.03	2.84 ± 0.04	3.24 ± 0.03
56492.169	-0.17 ± 0.21	2.52 ± 0.03	3.18 ± 0.04	3.35 ± 0.04
56492.767	-0.47 ± 0.21	2.34 ± 0.03	2.96 ± 0.04	3.35 ± 0.03
56524.075	-0.64 ± 0.21	2.18 ± 0.03	3.01 ± 0.04	3.25 ± 0.03
56524.873	-0.35 ± 0.21	2.4 ± 0.03	3.06 ± 0.04	3.32 ± 0.03
56525.439	-0.52 ± 0.21	2.31 ± 0.03	3.09 ± 0.04	3.34 ± 0.03
56534.686	-0.35 ± 0.25	2.29 ± 0.03	2.82 ± 0.05	3.18 ± 0.04
56541.158	-0.36 ± 0.23	2.56 ± 0.03	3.34 ± 0.05	3.56 ± 0.04
56548.071	-0.45 ± 0.23	2.83 ± 0.04	3.76 ± 0.06	4.03 ± 0.05

Time MJD	α_{UV}	W_1 $10^{-11}\ ergs\,cm^{-2}s^{-1}$	M_2 $10^{-11}\ ergs\,cm^{-2}s^{-1}$	W_2 $10^{-11}\ ergs\,cm^{-2}s^{-1}$
56555.134	-0.3 ± 0.22	2.62 ± 0.03	3.17 ± 0.05	3.58 ± 0.04
56562.354	-0.36 ± 0.26	2.52 ± 0.04	3.34 ± 0.06	3.51 ± 0.04
56567.986	-0.83 ± 0.3	2.31 ± 0.04	3.29 ± 0.07	3.6 ± 0.05
57001.752	-0.14 ± 0.23	2.39 ± 0.03	2.98 ± 0.04	3.15 ± 0.04
57003.351	0.23 ± 0.23	2.21 ± 0.03	2.56 ± 0.04	2.66 ± 0.03
57236.838	0.22 ± 0.24	2.0 ± 0.03	2.5 ± 0.04	2.42 ± 0.03
57239.764	0.27 ± 0.25	1.95 ± 0.03	2.1 ± 0.04	2.32 ± 0.03
57245.092	-0.47 ± 0.24	2.14 ± 0.03	2.78 ± 0.04	3.07 ± 0.04
57251.608	0.09 ± 0.29	1.92 ± 0.03	2.32 ± 0.05	2.4 ± 0.03
57254.146	-0.14 ± 0.24	2.07 ± 0.03	2.48 ± 0.05	2.72 ± 0.03
57257.669	-0.1 ± 0.25	1.88 ± 0.03	2.46 ± 0.04	2.46 ± 0.03
57260.092	0.04 ± 0.24	2.02 ± 0.03	2.5 ± 0.04	2.56 ± 0.03
57263.853	0.12 ± 0.26	1.9 ± 0.03	2.28 ± 0.04	2.36 ± 0.03
57275.414	-0.23 ± 0.27	1.98 ± 0.03	2.55 ± 0.07	2.67 ± 0.04
57282.832	-0.35 ± 0.27	2.18 ± 0.03	2.85 ± 0.05	3.03 ± 0.04
57289.947	-0.48 ± 0.27	2.42 ± 0.03	3.25 ± 0.07	3.47 ± 0.05
57295.042	-0.57 ± 0.24	2.6 ± 0.03	3.37 ± 0.06	3.8 ± 0.05
57303.35	-0.22 ± 0.24	2.93 ± 0.04	3.47 ± 0.05	3.94 ± 0.05
57310.937	-0.14 ± 0.26	2.54 ± 0.04	3.15 ± 0.05	3.35 ± 0.04
57317.291	-0.39 ± 0.24	2.52 ± 0.03	3.2 ± 0.05	3.54 ± 0.04
57331.448	0.08 ± 0.24	2.11 ± 0.03	2.54 ± 0.04	2.64 ± 0.03
57338.282	-0.28 ± 0.25	2.3 ± 0.03	2.88 ± 0.05	3.15 ± 0.04
57345.446	0.07 ± 0.27	2.26 ± 0.03	2.52 ± 0.04	2.83 ± 0.04
57352.69	-0.01 ± 0.26	2.23 ± 0.03	2.77 ± 0.05	2.85 ± 0.04
57359.163	-0.27 ± 0.41	2.07 ± 0.05	2.6 ± 0.08	2.81 ± 0.06
57364.748	-0.06 ± 0.34	2.13 ± 0.03	2.59 ± 0.1	2.76 ± 0.06
57371.548	-0.22 ± 0.31	2.22 ± 0.04	2.32 ± 0.08	2.98 ± 0.05
57380.416	-0.03 ± 0.27	2.14 ± 0.03	2.61 ± 0.04	2.75 ± 0.04
58759.302	0.14 ± 0.23	1.73 ± 0.02	1.84 ± 0.03	2.14 ± 0.03
58765.143	-0.29 ± 0.29	1.87 ± 0.03	2.45 ± 0.05	2.56 ± 0.04

Time MJD	α_{UV}	W_1 $10^{-11}\ ergs\,cm^{-2}s^{-1}$	M_2 $10^{-11}\ ergs\,cm^{-2}s^{-1}$	W_2 $10^{-11}\ ergs\,cm^{-2}s^{-1}$
58774.508	-0.18 ± 0.28	2.12 ± 0.03	2.78 ± 0.05	2.82 ± 0.04
58831.707	-0.05 ± 0.24	2.60 ± 0.03	3.13 ± 0.05	3.36 ± 0.04
58838.320	-0.08 ± 0.29	2.32 ± 0.04	2.85 ± 0.06	3.01 ± 0.04
59051.708	-0.60 ± 0.33	2.53 ± 0.05	3.30 ± 0.07	3.73 ± 0.06
59059.617	-0.20 ± 0.32	2.64 ± 0.05	3.22 ± 0.07	3.52 ± 0.06
59065.325	-0.26 ± 0.34	2.25 ± 0.04	3.03 ± 0.07	3.06 ± 0.05
59644.811	-0.37 ± 0.26	2.14 ± 0.03	2.69 ± 0.05	2.99 ± 0.04
59651.343	-0.28 ± 0.26	2.24 ± 0.03	2.89 ± 0.05	3.06 ± 0.04
59786.310	-0.14 ± 0.43	2.05 ± 0.05	2.70 ± 0.07	2.71 ± 0.06
59792.276	-0.27 ± 0.31	2.17 ± 0.04	2.46 ± 0.05	2.96 ± 0.04
59818.861	0.06 ± 0.49	1.85 ± 0.05	2.41 ± 0.08	2.32 ± 0.06
59833.649	-0.26 ± 0.51	1.71 ± 0.05	2.34 ± 0.08	2.32 ± 0.06
59846.704	0.30 ± 0.43	2.13 ± 0.05	2.47 ± 0.07	2.52 ± 0.05
59882.971	0.38 ± 0.40	2.4 ± 0.05	2.55 ± 0.07	2.79 ± 0.06
59885.490	0.22 ± 0.30	2.21 ± 0.04	2.5 ± 0.05	2.67 ± 0.04
59936.702	-0.26 ± 0.28	2.55 ± 0.04	3.07 ± 0.06	3.46 ± 0.05
59937.765	0.03 ± 0.42	2.57 ± 0.06	3.08 ± 0.09	3.25 ± 0.07
59957.174	-0.08 ± 0.33	2.28 ± 0.04	3.07 ± 0.07	2.95 ± 0.05
59966.240	0.02 ± 0.40	1.97 ± 0.05	2.65 ± 0.07	2.49 ± 0.05
59968.883	0.16 ± 0.41	2.38 ± 0.06	2.63 ± 0.07	2.92 ± 0.06
59976.381	0.02 ± 0.44	2.08 ± 0.05	2.94 ± 0.08	2.64 ± 0.06
59986.446	-0.09 ± 0.30	2.09 ± 0.04	2.52 ± 0.05	2.72 ± 0.04
59981.081	0.16 ± 0.27	2.17 ± 0.03	2.63 ± 0.09	2.65 ± 0.04
59988.239	-0.32 ± 0.29	1.91 ± 0.03	2.51 ± 0.05	2.64 ± 0.04

Appendix: Fermi LAT Parameters

Table 11: Fermi LAT Flux and Photon Index

Time MJD	Γ_γ	γ-Flux $10^{-11}\ ergs\,cm^{-2}s^{-1}$	TS
54783	-2.82 ± 0.27	11.67 ± 2.8	35.99
54786	-2.69 ± 0.21	15.85 ± 3.19	57.84
54832	-2.86 ± 0.34	9.41 ± 2.63	23.55
54935	-2.22 ± 0.26	11.95 ± 4.24	22.73
54938	-2.46 ± 0.23	14.15 ± 3.66	37.8
55025	-3.06 ± 0.47	7.54 ± 2.46	15.2
55400	-3.55 ± 0.68	5.78 ± 2.06	12.26
55471	-2.49 ± 0.30	10.74 ± 3.72	20.83
55543	-2.77 ± 0.27	13.57 ± 3.63	26.45
55670	-2.78 ± 0.33	7.25 ± 2.19	21.63
55679	-3.04 ± 0.53	8.14 ± 2.58	16.63
55682	-2.79 ± 0.24	16.79 ± 3.51	43.1
55694	-2.63 ± 0.31	11.59 ± 4.18	17.51
55697	-2.60 ± 0.29	13.81 ± 4.5	19.95
55715	-3.02 ± 0.64	7.11 ± 2.7	11.82
55859	-2.76 ± 0.33	11.90 ± 4.06	21.75
55862	-2.76 ± 0.28	14.45 ± 3.84	29.02
56196	-2.90 ± 0.44	4.32 ± 1.48	12.71
56269	-3.00 ± 0.33	12.37 ± 2.98	34.52
56272	-2.57 ± 0.18	26.68 ± 4.59	91.67
56278	-2.77 ± 0.29	13.57 ± 3.52	31.14
56284	-2.48 ± 0.29	11.72 ± 4.34	21.35
56287	-2.46 ± 0.16	30.34 ± 5.61	91.24
56290	-2.46 ± 0.24	16.10 ± 4.39	39.65
56293	-3.36 ± 0.56	8.63 ± 2.67	17.85
56298	-2.51 ± 0.24	13.92 ± 3.69	33.15
56304	-2.49 ± 0.33	8.86 ± 3.16	17.17
56316	-2.75 ± 0.29	11.72 ± 2.98	31.68

Time MJD	Γ_γ	γ-Flux $10^{-11}\ ergs\,cm^{-2}s^{-1}$	TS
56325	-2.85 ± 0.35	9.78 ± 3.03	20.12
56328	-3.3 ± 0.52	11.6 ± 3.04	28.38
56331	-2.74 ± 0.28	15.67 ± 4.05	34.4
56334	-2.68 ± 0.22	20.14 ± 4.48	51.49
56340	-2.87 ± 0.47	8.84 ± 3.27	13.14
56473	-2.34 ± 0.15	31.61 ± 5.26	130.86
56477	-2.69 ± 0.37	10.48 ± 3.54	17.71
56480	-2.6 ± 0.23	13.81 ± 3.16	43.66
56483	-2.66 ± 0.23	16.32 ± 3.47	49.92
56486	-2.39 ± 0.19	22.33 ± 4.96	66.31
56489	-2.7 ± 0.24	15.42 ± 3.55	48.46
56492	-3.04 ± 0.38	9.4 ± 2.8	21.42
56495	-2.76 ± 0.35	9.72 ± 3.1	19.28
56498	-2.32 ± 0.24	15.2 ± 4.59	36.15
56506	-3.07 ± 0.49	6.7 ± 2.51	12.31
56512	-2.86 ± 0.3	12.59 ± 2.98	42.35
56533	-2.64 ± 0.17	36.18 ± 4.95	160.17
56536	-2.53 ± 0.14	49.17 ± 6.36	201.16
56539	-2.62 ± 0.29	16.49 ± 4.67	22.82
56542	-2.94 ± 0.28	15.66 ± 3.54	39.63
56545	-3.54 ± 0.68	9.36 ± 2.72	19.4
56584	-2.74 ± 0.26	10.12 ± 2.47	42.21
56599	-3.02 ± 0.43	10.6 ± 3.46	14.98
56998	-2.68 ± 0.22	17.94 ± 3.53	60.28
57001	-3.09 ± 0.42	10.6 ± 2.77	34.58

Time MJD	Γ_γ	γ-Flux $10^{-11}\ ergs\,cm^{-2}s^{-1}$	TS
57007	-2.86 ± 0.33	10.83 ± 2.8	29.29
57010	-2.88 ± 0.28	13.33 ± 2.87	45.95
57013	-3.0 ± 0.39	10.19 ± 2.76	26.51
57016	-2.82 ± 0.23	19.79 ± 3.62	73.59
57022	-3.59 ± 0.62	9.72 ± 2.8	21.48
57052	-3.43 ± 0.81	6.24 ± 2.29	13.07
57093	-2.64 ± 0.33	10.64 ± 3.49	22.3
57108	-3.0 ± 0.39	14.0 ± 4.49	22.65
57111	-3.59 ± 1.01	8.8 ± 2.69	18.93
57119	-3.07 ± 0.4	9.33 ± 2.51	24.95
57185	-3.98 ± 1.02	8.18 ± 2.92	11.34
57188	-3.23 ± 0.42	9.27 ± 3.11	14.66
57203	-2.76 ± 0.3	10.68 ± 3.03	24.78
57305	-2.9 ± 0.46	8.89 ± 2.94	16.35
57308	-3.43 ± 0.66	6.87 ± 2.37	13.08
57326	-2.67 ± 0.27	12.47 ± 3.29	33.53
57328	-3.32 ± 0.61	6.45 ± 2.2	13.95
57521	-4.06 ± 2.22	7.1 ± 2.26	16.48
57733	-2.83 ± 0.39	6.84 ± 2.5	13.69
57774	-3.94 ± 1.09	6.51 ± 2.14	14.31
58366	-2.93 ± 0.47	5.45 ± 1.96	14.42
58447	-2.89 ± 0.34	6.97 ± 2.04	20.18
58781	-2.68 ± 0.34	10.6 ± 3.93	15.0
58789	-2.45 ± 0.21	19.8 ± 4.2	64.78
59890	-2.88 ± 0.45	8.2 ± 3.08	11.91

Bibliography

[1] A. A. Abdo et al. «Fermi/Large Area Telescope Discovery of Gamma-Ray Emission from a Relativistic Jet in the Narrow-Line Quasar PMN J0948+0022». In: 699.2 (July 2009), pp. 976–984.

[2] A. A. Abdo et al. «Multiwavelength Monitoring of the Enigmatic Narrow-Line Seyfert 1 PMN J0948+0022 in 2009 March-July». In: 707.1 (Dec. 2009), pp. 727–737. DOI: 10.1088/0004-637X/707/1/727.

[3] Clabon Walter Allen and Arthur N Cox. *Allen's astrophysical quantities*. Springer Science & Business Media, 2000.

[4] S. Antón et al. «The colour of the narrow line Sy1-blazar 0324+3410». In: 490.2 (Nov. 2008), pp. 583–587.

[5] R. R. J. Antonucci and J. S. Miller. «Spectropolarimetry and the nature of NGC 1068.» In: 297 (Oct. 1985), pp. 621–632. DOI: 10.1086/163559.

[6] Robert Antonucci. «Unified models for active galactic nuclei and quasars.» In: 31 (Jan. 1993), pp. 473–521. DOI: 10.1146/annurev.aa.31.090193.002353.

[7] WB Atwood et al. «The large area telescope on the Fermi gamma-ray space telescope mission». In: *The Astrophysical Journal* 697.2 (2009), p. 1071.

[8] Cosimo Bambi. «X-ray Tests of General Relativity with Black Holes». In: *Symmetry* 15 (June 2023), p. 1277. DOI: 10.3390/sym15061277.

[9] Scott D Barthelmy et al. «The burst alert telescope (BAT) on the SWIFT midex mission». In: *Space Science Reviews* 120 (2005), pp. 143–164.

[10] GS Bisnovatyi-Kogan and SI Blinnikov. «Disk accretion onto a black hole at subcritical luminosity». In: *Astronomy and Astrophysics, vol. 59, no. 1, July 1977, p. 111-125.* 59 (1977), pp. 111–125.

[11] R. D. Blandford and R. L. Znajek. «Electromagnetic extraction of energy from Kerr black holes». In: *Monthly Notices of the Royal Astronomical Society* 179.3 (July 1977), pp. 433–456. ISSN: 0035-8711. DOI: 10.1093/mnras/179.3.433. URL: https://doi.org/10.1093/mnras/179.3.433.

[12] M. Błażejowski et al. «Comptonization of Infrared Radiation from Hot Dust by Relativistic Jets in Quasars». In: 545.1 (Dec. 2000), pp. 107–116.

[13] Laura W. Brenneman and Christopher S. Reynolds. «RELATIVISTIC BROADENING OF IRON EMISSION LINES IN A SAMPLE OF ACTIVE GALACTIC NUCLEI». In: *The Astrophysical Journal* 702.2 (2009), p. 1367. DOI: 10.1088/0004-637X/702/2/1367.

[14] David N Burrows et al. «The Swift X-ray telescope». In: *Space science reviews* 120 (2005), pp. 165–195.

[15] Jason A Cardelli et al. «The relationship between infrared, optical, and ultraviolet extinction». In: *Astrophysical Journal, Part 1 (ISSN 0004-637X), vol. 345, Oct. 1, 1989, p. 245-256.* 345 (1989), pp. 245–256.

[16] Bożena Czerny et al. «Accretion disk model of short-timescale intermittent activity in young radio sources». In: *The Astrophysical Journal* 698.1 (2009), p. 840.

[17] B De Marco et al. «PG 1211+ 143: probing high-frequency lags in a high-mass active galactic nucleus». In: *Monthly Notices of the Royal Astronomical Society: Letters* 417.1 (2011), pp. L98–L102.

[18] R Decarli et al. «On the geometry of broad emission region in quasars». In: *Monthly Notices of the Royal Astronomical Society* 387.3 (2008), pp. 1237–1247.

[19] Charles D. Dermer and Reinhard Schlickeiser. «Model for the High-Energy Emission from Blazars». In: 416 (Oct. 1993), p. 458.

[20] A. C. Fabian et al. «Properties of AGN coronae in the NuSTAR era». In: 451.4 (Aug. 2015), pp. 4375–4383. DOI: 10.1093/mnras/stv1218.

[21] S. A. E. G. Falle. «Plasma jets from active galactic nuclei». In: *Comparative Study of Magnetospheric Systems*. Jan. 1986, pp. 16–24.

[22] L. Foschini. «Powerful relativistic jets in narrow-line Seyfert 1 glaxies (review)». In: *Proceedings of Nuclei of Seyfert galaxies and QSOs - Central engine & conditions of star formation (Seyfert 2012). 6-8 November*. Jan. 2012, 10.

[23] Luigi Foschini. «The Blandford-Znajek theory revisited». In: *arXiv e-prints* (May 2012).

[24] Luigi Foschini. «The Unification of Relativistic Jets». In: *International Journal of Modern Physics Conference Series*. Vol. 28. International Journal of Modern Physics Conference Series. Mar. 2014, 1460188, p. 1460188.

[25] Luigi Foschini. «What We Talk about When We Talk about Blazars?» In: vol. 4. Apr. 2017. DOI: 10.3389/fspas.2017.00006.

[26] Luigi Foschini et al. «Mapping the narrow-line Seyfert 1 galaxy 1H 0323+ 342». In: *Universe* 5.9 (2019), p. 199.

[27] G. Fossati et al. «A unifying view of the spectral energy distributions of blazars». In: 299.2 (Sept. 1998), pp. 433–448. DOI: 10.1046/j.1365-8711.1998.01828.x.

[28] A. A. Galeev et al. «Structured coronae of accretion disks.» In: 229 (Apr. 1979), pp. 318–326. DOI: 10.1086/156957.

[29] Neil Gehrels et al. «The Swift gamma-ray burst mission». In: *The Astrophysical Journal* 611.2 (2004), p. 1005.

[30] G. Ghisellini et al. «A theoretical unifying scheme for gamma-ray bright blazars». In: 301.2 (Dec. 1998), pp. 451–468. DOI: 10.1046/j.1365-8711.1998.02032.x.

[31] Francesco Haardt and Laura Maraschi. «X-Ray Spectra from Two-Phase Accretion Disks». In: 413 (Aug. 1993), p. 507. DOI: 10.1086/173020.

[32] Kazuhiro Hada. «Relativistic Jets from AGN Viewed at Highest Angular Resolution». In: *Galaxies* 8.1 (Dec. 2019), p. 1. DOI: 10.3390/galaxies8010001.

[33] Sebastian Heinz and RA Sunyaev. «The non-linear dependence of flux on black hole mass and accretion rate in core-dominated jets». In: *Monthly Notices of the Royal Astronomical Society* 343.3 (2003), pp. L59–L64.

[34] E. Järvelä et al. «Near-infrared morphologies of the host galaxies of narrow-line Seyfert 1 galaxies». In: 619, A69 (Nov. 2018), A69.

[35] Emilia Järvelä et al. «Statistical multifrequency study of narrow-line Seyfert 1 galaxies». In: *Astronomy & Astrophysics* 573 (2015), A76.

[36] E Kara et al. «Revealing the X-ray source in IRAS 13224- 3809 through flux-dependent reverberation lags». In: *Monthly Notices of the Royal Astronomical Society* 430.2 (2013), pp. 1408–1413.

[37] K. I. Kellermann et al. «VLA Observations of Objects in the Palomar Bright Quasar Survey». In: 98 (Oct. 1989), p. 1195. DOI: 10.1086/115207.

[38] Edward Ye Khachikian and Daniel W Weedman. «An atlas of Seyfert galaxies». In: *Astrophysical Journal, vol. 192, Sept. 15, 1974, pt. 1, p. 581-589.* 192 (1974), pp. 581–589.

[39] Ari Laor et al. «The soft X-ray properties of a complete sample of optically selected quasars. II. Final results». In: *The Astrophysical Journal* 477.1 (1997), p. 93.

[40] Karen M. Leighly. «A Comprehensive Spectral and Variability Study of Narrow-Line Seyfert 1 Galaxies Observed by ASCA. I. Observations and Time Series Analysis». In: 125.2 (Dec. 1999), pp. 297–316.

[41] Karen M. Leighly. «A Comprehensive Spectral and Variability Study of Narrow-Line Seyfert 1 Galaxies Observed by ASCA. II. Spectral Analysis and Correlations». In: 125.2 (Dec. 1999), pp. 317–348. eprint: astro-ph/9907295 (astro-ph).

[42] Alessandro Marconi et al. «The effect of radiation pressure on virial black hole mass estimates and the case of narrow-line Seyfert 1 galaxies». In: *The Astrophysical Journal* 678.2 (2008), p. 693.

[43] J. R. Mattox et al. «The Likelihood Analysis of EGRET Data». In: 461 (Apr. 1996), p. 396. DOI: 10.1086/177068.

[44] Sergio A Mundo et al. «The origin of X-ray emission in the gamma-ray emitting narrow-line Seyfert 1 1H 0323+ 342». In: *Monthly Notices of the Royal Astronomical Society* 496.3 (2020), pp. 2922–2931.

[45] K. Nandra and K. A. Pounds. «GINGA observations of the X-ray spectra of Seyfert galaxies.» In: 268 (May 1994), pp. 405–429. DOI: 10.1093/mnras/268.2.405.

[46] Alejandro Olguín-Iglesias et al. «The disc-like host galaxies of radio-loud narrow-line Seyfert 1s». In: 492.1 (Feb. 2020), pp. 1450–1464.

[47] Donald E. Osterbrock. «Observational Model of the Ionized Gas in Seyfert and Radio-Galaxy Nuclei». In: *Proceedings of the National Academy of Sciences of the United States of America* 75.2 (1978), pp. 540–544. ISSN: 00278424. URL: http://www.jstor.org/stable/67820 (visited on 10/23/2023).

[48] Paolo Padovani. «Gamma-ray emitting AGN and unified schemes». In: (1997).

[49] Uria Peretz and Ehud Behar. «Classifying AGN by X-ray hardness variability». In: *Monthly Notices of the Royal Astronomical Society* 481.3 (2018), pp. 3563–3572.

[50] B. M. Peterson. «Masses of Black Holes in Active Galactic Nuclei: Implications for Narrow-Line Seyfert 1 Galaxies». In: *Narrow-Line Seyfert 1 Galaxies and their Place in the Universe*. Ed. by L. Foschini et al. Jan. 2011, 32, p. 32. DOI: 10.22323/1.126.0032.

[51] Bradley M Peterson. *An introduction to active galactic nuclei*. Cambridge University Press, 1997.

[52] Bradley M. Peterson and Amri Wandel. «Keplerian Motion of Broad-Line Region Gas as Evidence for Supermassive Black Holes in Active Galactic Nuclei». In: 521.2 (Aug. 1999), pp. L95–L98.

[53] E Piconcelli et al. «The XMM-Newton view of PG quasars-I. X-ray continuum and absorption». In: *Astronomy & Astrophysics* 432.1 (2005), pp. 15–30.

[54] JN Reeves and Martin JL Turner. «X-ray spectra of a large sample of quasars with ASCA». In: *Monthly Notices of the Royal Astronomical Society* 316.2 (2000), pp. 234–248.

[55] R. A. Remillard et al. «Twenty-Two Emission-Line AGNs From the HEAO-1 X-Ray Survey». In: 105 (June 1993), p. 2079. DOI: 10.1086/116585.

[56] Peter WA Roming et al. «Ultraviolet/Optical Telescope of the Swift MIDEX mission». In: *X-Ray and Gamma-Ray Instrumentation for Astronomy XI*. Vol. 4140. SPIE. 2000, pp. 76–86.

[57] R. R. Ross and A. C. Fabian. «A comprehensive range of X-ray ionized-reflection models». In: 358.1 (Mar. 2005), pp. 211–216. DOI: 10.1111/j.1365-2966.2005.08797.x.

[58] George B. Rybicki and Alan P. Lightman. *Radiative processes in astrophysics*. 1979.

[59] Mara Salvato. «ROSAT Bright Survey: Seyfert 1 host galaxies and their environment». In: *Ph. D. Thesis* (2002).

[60] Allan Sandage. «Intensity Variations of Quasi-stellar Sources in Optical Wavelengths». In: *Quasars and high-energy astronomy*. Jan. 1969, p. 93.

[61] M. Schmidt. «3C 273 : A Star-Like Object with Large Red-Shift». In: 197.4872 (Mar. 1963), p. 1040. DOI: 10.1038/1971040a0.

[62] Carl K. Seyfert. «Nuclear Emission in Spiral Nebulae.» In: 97 (Jan. 1943), p. 28. DOI: 10.1086/144488.

[63] NI Shakura and RA Sunyaev. «Black Holes in Binary Systems: Observational Appearances». In: *Symposium-International Astronomical Union*. Vol. 55. Cambridge University Press. 1973, pp. 155–164.

[64] Marek Sikora et al. «Comptonization of Diffuse Ambient Radiation by a Relativistic Jet: The Source of Gamma Rays from Blazars?» In: 421 (Jan. 1994), p. 153. DOI: 10.1086/173633.

[65] S. Vaughan et al. «X-ray spectral complexity in narrow-line Seyfert 1 galaxies». In: *Monthly Notices of the Royal Astronomical Society* 309.1 (Oct. 1999), pp. 113–124. ISSN: 0035-8711. DOI: 10.1046/j.1365-8711.1999.02811.x. URL: https://doi.org/10.1046/j.1365-8711.1999.02811.x.

[66] Amri Wandel and Vahe Petrosian. «Accretion-disk modeling of the UV spectrum of quasars». In: *Astrophysical Journal, Part 2-Letters (ISSN 0004-637X), vol. 329, June 1, 1988, p. L11-L16.* 329 (1988), pp. L11–L16.

[67] Fang Wang et al. «Reverberation mapping of the gamma-ray loud narrow-line Seyfert 1 galaxy 1H 0323+ 342». In: *The Astrophysical Journal* 824.2 (2016), p. 149.

[68] Hongyan Zhou et al. «A narrow-line Seyfert 1-blazar composite nucleus in 2MASX J0324+ 3410». In: *The Astrophysical Journal* 658.1 (2007), p. L13.

Acknowledgments

Ringrazio infinitamente il mio relatore Stefano Ciroi e il mio correlatore Luigi Foschini per avermi seguita e appassionata nella mia ricerca, guidandomi ma allo stesso tempo lasciandomi libera di testare ed esplorare gli strumenti e le risorse a disposizione. Da questi nove mesi di analisi credo di emergere più matura e consapevole e, spero, anche più pronta a proseguire "autonomamente" le mie ricerche nutrendo la mia curiosità.

Alla fine del mio tortuoso e sregolato percorso universitario voglio ringraziare in primis il mio spirito: determinato e ambizioso, che ha resistito e affrontato tempi difficili e situazioni di sfida. Ma questo spirito non sarebbe stato così potente senza le persone meravigliose che mi hanno accompagnata a modo loro durante tutto il viaggio.

Ringrazio i miei genitori che fin da quando ero piccola hanno visto in me una piccola scintilla e hanno creduto in me anche quando quella scintilla era un po' oscurata dalla confusione dell'adolescenza.

A mia mamma, la donna più forte che conosco, che stimo e ammiro nonostante tutti gli scontri e discussioni. Tutta la mia determinazione arriva da quel concentrato di volontà e impegno che lei incarna e le sono immensamente riconoscente per aver sempre lottato per il mio futuro.

A mio padre, alla sua dolcezza. A mio padre, che non mi ha mai fatto sentire un fallimento e mi ha lasciata sbocciare perché sarei stata per lui una creatura meravigliosa chiunque avessi deciso di essere.

A mio fratello Maxi, per farmi sperare ogni giorno che diventare adulta non significhi diventare noiosa e stanca. A Maxi, per essere sempre un'ispirazione ma anche un caro amico. Per saper sdrammatizzare, perché la leggerezza non è superficialità, è planare dall'alto senza pesi sul cuore.

A mia cognata Adriana, che da quel posto a tavola che si era presa nel lontano 2003, ora si è presa un posto enorme nel mio cuore. Per Feli ed Ele, per la loro curiosità e genuinità, per rendermi partecipe delle loro vite nonostante io sia una visitatrice occasionale. Sono grata ad avere una famiglia così unita e variopinta.

Acknowledgments

A Michelle, a tutta la sua grinta ma allo stesso tempo alla sensibilità che riesce a trasmettere. Al nostro reciproco supporto nelle nostre vite diverse ma sempre impostate sullo scoprirsi, e costruirsi. A Eleonora, alla sua dolcezza e trasparenza. Al nostro "vem", perché anche se sono lontana e non so tenere i contatti, il nostro legame è rimasto forte ed è maturato insieme a noi in questi anni di distanza.

A Elettra, alle mille disavventure che insieme hanno sempre il sapore di avventure, ai libri che ci potremmo scrivere. Al sostegno e agli sfoghi, alle notti passate in Pollaio e alle cene sedute per terra con i triangoli della pam.

A Francesco, la mia anima gemella, che, anche se sempre in altre città è sempre rimasto così vicino da poter comprendere ogni mio pensiero. Al nostro trio "poveri" che resta sempre ricco di ricordi, sogni e stima l'uno per l'altro.

A Giorgia, la mia compagna di studio costante, colei che ha sopportato tutti i miei ritardi, che ha subito tutti i miei sfoghi. Ogni giorno una certezza, con la pioggia o con il sole, l'appuntamento per studiare insieme e motivarci a vicenda.

Ai tipici, Princi, Hussy, Rachi, Matte e a quel benedetto AIESEC Brazil che ci ha fatti incontrare. A tutte le sfaccettature di questi giramondo che perfettamente si incastrano l'una con l'altra nel formare il nostro unico e tipico quadro colorato, ovviamente con la "Valemess face". A Ortona, Caldonazzo, Festivalletteratura e tutte le altre nostre sedi che dobbiamo tornare a ripopolare presto.

A Camilla, Sabrina e Marco che mi hanno accolta nel loro gruppo ancora quando ero una maschietta insicura. Ricordo che dopo un anno difficile alle superiori ho passato un'estate dove mi sentivo me stessa senza dover fingere nulla.

A Mavi, ai coinquilini vecchi e nuovi che hanno purtroppo dovuto sopportare i miei disordini, ma che ognuno a loro modo (tranne la Margherita) ha portato la sua musica nella convivenza creando un'armonia, che anche se stonata era sempre avvolgente.

To Donna, and Tim, my American parents, that have always incited me and inspired me to follow my dreams and passions without worrying about judgements or social rules. They left an indelible mark in my soul and they will always have a special spot in my heart.

Infine ringrazio Padova e Bologna per essere state teatro delle mie attività e per essere città così vive e variopinte da nutrire il mio spirito vivace.